Politecnico di Torino

Politecnico di Torino

Corso di Laurea Magistrale in Ingegneria Chimica e dei Processi Sostenibili

Anno accademico 2025/2026

Multiphysics Modeling of Ammonia Decomposition Reactors

From Packed Beds to Monolithic Catalyst Geometries

Relatori:
Daniele Marchisio
Marcus Rose
Tobias Wittmann

Candidato:
Gianluca Deferre

Marzo 2026

Index

List of Figures

List of Tables

Italian Summary

L’impiego di combustibili fossili per la produzione di energia comporta criticità ambientali significative per gli attuali sistemi energetici, rendendo necessaria la transizione verso vettori energetici alternativi. L’idrogeno è ampiamente riconosciuto come vettore energetico carbon-free, mentre l’ammoniaca è emersa recentemente come alternativa pratica per il suo stoccaggio, il trasporto e la produzione on-site di idrogeno tramite decomposizione catalitica.

Il presente lavoro si concentra sullo sviluppo di un modello computazionale di un reattore a letto fisso, in scala di laboratorio, operato presso la Technische Universität Darmstadt per il test di catalizzatori per la decomposizione dell’ammoniaca. Sebbene il reattore sperimentale sia principalmente destinato a indagini cinetiche, lo studio di modellazione mira a fornire una comprensione dei fenomeni accoppiati di trasporto e reazione che governano il comportamento del reattore e a stabilire un framework estendibile a configurazioni di reattori scalabili.

Il modello numerico è stato generato con il software COMSOL Multiphysics®, che discretizza la formulazione continua mediante il metodo degli elementi finiti (FEM). In contrasto con gli approcci semplificati di equilibrio termico locale frequentemente adottati per sistemi analoghi, la formulazione sviluppata tiene esplicitamente conto del local thermal non-equilibrium (LTNE) tra la fase solida catalitica e la fase fluida. Il bilancio della quantità di moto è descritto tramite la formulazione di Brinkman, che estende la legge di Darcy includendo gli effetti di shear viscoso. Le equazioni di governo sono accoppiate a un modello di reazione eterogenea che descrive la decomposizione dell’ammoniaca sulla base di una legge cinetica di tipo Temkin–Pyzhev.

Il sistema di equazioni non lineari risultante dall’accoppiamento tra le diverse fisiche è stato risolto mediante il metodo iterativo di Newton. Per il trattamento del problema multiphysics è stata adottata una strategia di soluzione segregata, in cui i diversi campi di variabili vengono risolti in modo sequenziale all’interno di ciascuna iterazione, fino al raggiungimento della convergenza globale del sistema. I sistemi lineari sono stati risolti mediante il solver diretto PARDISO (Parallel Direct Sparse Solver), ampiamente utilizzato per problemi multiphysics di tipo stazionario. Il criterio di convergenza del solver è stato impostato imponendo una tolleranza relativa pari a 10^{-4} sui residui del sistema.

Una verifica sistematica del framework numerico è stata inizialmente condotta per valutarne la coerenza interna. Il modello riproduce correttamente il comportamento qualitativo atteso dei reattori per la decomposizione dell’ammoniaca: l’evoluzione assiale delle specie chimiche lungo il letto catalitico, l’espansione molare associata alla stechiometria della reazione e il marcato abbassamento della temperatura dovuto alla reazione endotermica. L’analisi ha evidenziato i limiti di applicabilità del modello numerico, indicando che soluzioni fisicamente consistenti si ottengono soltanto al di sopra di una portata in ingresso minima di circa 80 mL/min. Al di sotto di tale valore, la significativa diffusione dell’idrogeno verso la sezione di ingresso del reattore si traduce in soluzioni numeriche non fisicamente plausibili e in un progressivo deterioramento delle proprietà di convergenza del solutore.

Il framework numerico è stato quindi utilizzato per condurre un’analisi parametrica e di sensitività finalizzata all’identificazione dei parametri chiave che influenzano le prestazioni del reattore. I risultati evidenziano il ruolo dominante dei fenomeni di trasporto termico nel determinare il comportamento del sistema. In particolare, la conducibilità termica efficace del letto catalitico influenza in modo significativo la distribuzione della temperatura all’interno del reattore, che a sua volta determina direttamente la velocità di reazione locale. Valori più elevati di conducibilità termica riducono il gradiente termico all’interno del letto e promuovono condizioni termiche più uniformi, migliorando di conseguenza le prestazioni complessive del reattore.

Come atteso, l’influenza della lunghezza del letto catalitico è banale: un aumento dell’altezza del letto comporta un incremento della conversione dell’ammoniaca grazie a tempi di residenza più elevati. A temperature operative elevate si osservano rendimenti marginali decrescenti, poiché la reazione tende ad avvicinarsi all’equilibrio termodinamico.

L’analisi dei parametri cinetici indica che le prestazioni del reattore sono principalmente controllate dai parametri di Arrhenius (energia di attivazione e fattore pre-esponenziale), che influenzano in modo significativo la conversione prevista dell'ammoniaca, mentre il parametro di Temkin (alpha) incide soprattutto sulla dipendenza

della velocità di reazione dalla composizione del gas, con un effetto relativamente minore sul comportamento globale del reattore.

Il framework modellistico è stato successivamente esteso all'analisi di configurazioni catalitiche alternative, basate su strutture monolitiche in nichel prodotte tramite additive manufacturing. Per consentire la simulazione di tali geometrie, il modello computazionale è stato riformulato adottando una rappresentazione tridimensionale esplicita delle strutture canalari dei catalizzatori monolitici. L'approssimazione di mezzo poroso e l'ipotesi di simmetria assiale, utilizzate per il letto impaccato, sono state pertanto abbandonate e sostituite da domini solido–fluido che rappresentano direttamente i volumi del monolite e dei canali.

Le simulazioni mostrano che i catalizzatori monolitici metallici presentano campi di temperatura significativamente più uniformi rispetto ai tradizionali letti impaccati, principalmente grazie alla maggiore conducibilità termica e alle migliori proprietà di trasporto del calore.

È stato infine effettuato un confronto tra diverse geometrie monolitiche. I risultati indicano che tali variazioni geometriche, nelle condizioni operative investigate, producono differenze relativamente moderate nelle prestazioni del reattore, con conversioni previste di ammoniaca comprese tra il 38% e il 42%. Ad ogni modo, le configurazioni monolitiche offrono vantaggi evidenti in termini di gestione termica e di perdita di carico rispetto ai letti impaccati convenzionali.

Nel complesso, il framework computazionale sviluppato rappresenta uno strumento utile per l'interpretazione di test catalitici su scala di laboratorio e per l'analisi delle complesse interazioni tra la cinetica di reazione e i fenomeni di trasporto nei reattori di cracking dell'ammoniaca. I risultati di questo lavoro indicano che il trasferimento di calore svolge un ruolo fondamentale nel determinare le prestazioni dei reattori e che le strutture catalitiche ad elevata conducibilità termica efficace possono migliorare significativamente il comportamento termico dei reattori di decomposizione dell'ammoniaca.

Nonostante i risultati promettenti, nel framework modellistico attuale persistono alcune semplificazioni. In particolare, la decomposizione dell'ammoniaca è stata implementata come termine di reazione volumetrico nella regione catalitica e i parametri cinetici sono stati tratti da correlazioni di letteratura, senza validazione sperimentale specifica per le geometrie considerate.

Futuri sviluppi dovrebbero pertanto concentrarsi sull'implementazione di modelli di reazione basati su cinetiche superficiali per i catalizzatori monolitici e sulla validazione sperimentale del modello numerico, al fine di migliorarne ulteriormente la capacità predittiva e di supportare la progettazione di catalizzatori ottimizzati per il cracking dell'ammoniaca.

Abstract

The production of energy from fossil fuels poses significant environmental concerns for today's energy systems, driving the need for carbon-free energy carriers. Hydrogen is widely regarded as a carbon-free energy carrier, and ammonia has emerged as a practical alternative for storing, transporting, and producing it on-site via catalytic decomposition.

This work focuses on developing a computational model of a laboratory-scale fixed-bed reactor operated at Technische Universität Darmstadt for testing ammonia-decomposition catalysts. While the experimental reactor is primarily intended for kinetic investigations, the modeling study aims to provide insight into the coupled transport and reaction phenomena governing reactor behavior and to establish a framework that can be extended toward scalable reactor configurations.

A heterogeneous two-phase reactor model is formulated to describe momentum, heat, and multicomponent mass transport within the catalytic bed. In contrast to simplified local thermal equilibrium approaches commonly adopted for similar systems, the present formulation explicitly accounts for local thermal non-equilibrium between the solid and fluid phases to assess its relevance. Particular attention is devoted to the role of effective bed thermal conductivity, internal temperature gradients, and their interaction with intrinsic reaction kinetics.

Parametric and sensitivity analyses are performed to evaluate the influence of catalyst kinetic parameters, catalytic bed height, and effective bed thermal conductivity on reactor conversion and temperature distribution. The modeling framework is extended further to analyze additively manufactured (3D-printed) monolithic catalysts, enabling a comparative investigation of multiple catalyst geometries under identical operating conditions. This allows the computational model to be used both to interpret laboratory-scale catalytic tests and to systematically evaluate alternative catalyst structures and reactor configurations.

1. Hydrogen Production

The negative environmental impact of energy production using fossil fuels is the fundamental problem of the current energy system. Over time, existing technologies have been improved, and alternative technologies to fossil fuels have been added. However, despite these developments, a truly radical transformation of the energy system, commonly referred to as the "energy transition", has not yet occurred (Lucentini Ilaria, 2021). In this scenario, Hydrogen is a promising alternative to fossil fuels in many applications: complementing electricity as a zero-carbon energy carrier that can be efficiently stored and transported, while contributing to a more secure energy system by reducing dependence on fossil fuels and offering versatility across the transport, industrial, heating, and power sectors (Iain Staffell, 2019).

The idea of using hydrogen as a central element of the energy system dates back to the early concepts of the "hydrogen economy" developed in the 1970s. Over time, hydrogen has evolved from a largely theoretical concept into a concrete technological option, with applications currently under investigation in both stationary and transport energy systems (Bockris, 2013). Hydrogen is taking one of the leading positions in the energy sector for stationary and transport applications. Its uses include vehicles and other means of transport, auxiliary power units, stationary power generation in domestic and industrial applications, and as an energy vector to store the excess of electrical energy generated off-peak (Lucentini Ilaria, 2021).

In 2018, around 120 million tonnes of hydrogen were produced each year, of which two-thirds is pure hydrogen, and one-third is in a mixture with other gases (Figure 1). This equals 14.4 exajoules (EJ), about 4% of global final energy and non-energy use, according to International Energy Agency (IEA) statistics. Around 95% of all hydrogen is generated from natural gas and coal. Around 5% is generated as a by-product of the chlor-alkali electrolysis process (IRENA, Hydrogen: a renewable energy perspective, 2019). In the iron and steel industry, coke oven gas also contains a high hydrogen share, some of which is recovered. In addition, there are small water-electrolysis-based hydrogen production facilities, although their contribution is currently limited. However, their early operational status shows a potential path toward achieving a green hydrogen transition.

Currently, there is no significant hydrogen production from renewable sources. Most of the hydrogen today is produced and used on-site in industry. The production of ammonia via Haber-Bosch Synthesis and oil refining are the prime purposes, accounting for two-thirds of hydrogen use. Hydrogen is primarily used in ammonia production for fertilizers, in petroleum refineries for hydrocracking and hydrogenation processes, and in methanol production from coal, with additional applications in chemical hydrogenations (IEA, The Future of Hydrogen, Seizing today's opportunities).

While today's hydrogen use has limited direct relevance for the energy transition, it has resulted in ample experience with hydrogen handling. Industrial maturity has established significant handling expertise; for instance, 3,000 km of high-pressure hydrogen pipelines are operational across Europe and North America (Iain Staffell, 2019). However, excessive costs prevent further pipeline development until sizeable and consistent demand for hydrogen can be assured. Similarly, there is a long record of transporting hydrogen in dedicated trucks. Beyond these conventional applications, which have been around for decades, hydrogen use is very modest. The importance of hydrogen for energy transition must come from new applications, and its supply needs to be decarbonized (IRENA, Hydrogen: a renewable energy perspective, 2019).

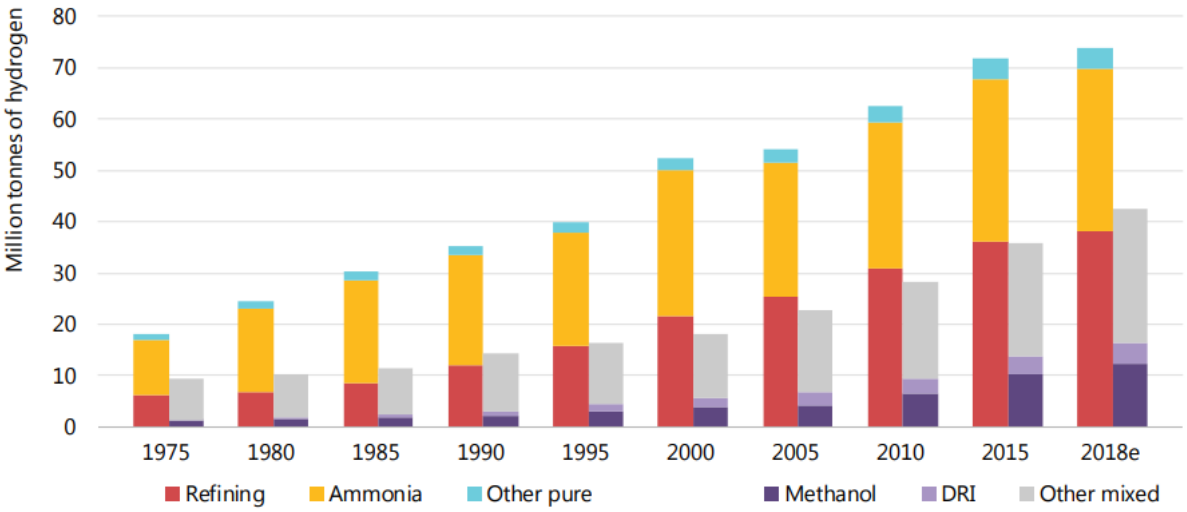

Figure 1, Hydrogen use trends, 1975 to 2018 (IEA, The Future of Hydrogen, Seizing today's opportunities)

Hydrogen will be part of emissions mitigation efforts in the coming decades. IRENA's Renewable Energy Roadmap (REmap) analysis indicates a 5% of total final energy consumption and 16% of all electricity generation being dedicated to hydrogen production in 2050 (IRENA, Global energy transformation: A roadmap to 2050 , (Full report, 2019)), while the Hydrogen Council in its roadmap suggests a much higher 18% share of the total final energy demand (Hydrogen Council, 2017).

1.1 Ammonia for Hydrogen Production

Among the various chemical media, ammonia stands out as one of the most promising hydrogen carriers. It has a high hydrogen content and can liquefy at low pressure, 8.6 bar at 20 °C (Lucentini Ilaria, 2021), which makes its transport and storage relatively easy and low-energy-demanding. The decomposition reaction of ammonia is the following.

$$2NH_3 \leftrightarrows N_2 + 3H_2, \qquad \Delta H^\circ = 92\ \mathrm{kJ\ mol^{-1}}$$

It's strongly endothermic and reaches up to 99.99% ammonia conversion at 400 °C and 1 atm according to thermodynamics (Elvira Spatolisano, 2023). This means that a moderately high operating temperature is required to drive the ammonia decomposition reaction to completion. Working above 99.99% conversion is compulsory if the hydrogen produced is used in fuel cells such as PEMFCs, which are irreparably degraded at very low concentrations of ammonia (ca. 0.1 ppm) (Lucentini Ilaria, 2021). Alternatively, hydrogen-selective membrane systems can be used, such as catalytic membrane reactors.

Ammonia is the second most produced chemical after sulfuric acid worldwide. The fertilizer industry is the biggest user of that chemical, which in turn accounts for nearly 70% of total demand (IEA, Ammonia Technology Roadmap: Towards more sustainable nitrogen fertiliser production, 2021). More than 90% of the world's ammonia is made through the Haber-Bosch process, which is basically the reverse reaction of catalytic decomposition. The process is thermochemical and usually applies iron-based catalysts with promoters. The process is conducted at very high temperatures, higher than 400 °C, and high pressures, typically in the range of 10 to 30 MPa (Speybroeck, 2024). Since the hydrogen feedstock is still mainly obtained from fossil fuels, the operation is very energy-demanding, around 2% of total final energy consumption and 1.3% of CO_2 emissions from the energy system (IEA, Ammonia Technology Roadmap: Towards more sustainable nitrogen fertiliser production, 2021). The industry, therefore, is shifting to less polluting ways of making ammonia: "blue ammonia", which combines carbon capture, utilization, and storage (CCUS) technologies, and "green ammonia," which relies on renewable hydrogen produced via water electrolysis.

The ammonia decomposition is favored at high temperatures and low pressures, considering that it is endothermic and occurs with an increase in the number of moles. The thermodynamic behavior of the reacting system is illustrated in Figure 2.

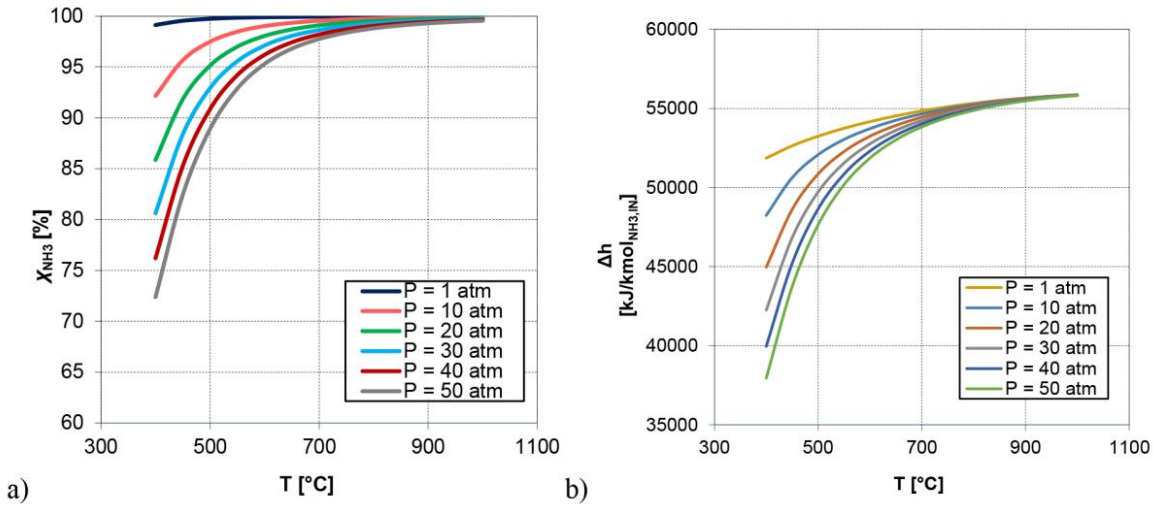

Figure 2, Thermodynamic analysis of NH3 cracking. (a) NH3 conversion as a function of temperature and at variable pressure; (b) enthalpy of reaction as a function of temperature and at variable pressure (Elvira Spatolisano, 2023)

As shown in Fig 2a, the equilibrium conversion increases with temperature and decreases with pressure. Figure 2b reports the reaction enthalpy under the same conditions. At these operating conditions, the cracking is typically kinetically limited. Moreover, the large amount of reaction heat required to sustain the process represents one of the main concerns from the standpoint of process economics.

At present, the industrial use of ammonia cracking is mainly associated with metallurgical applications, such as metal annealing and galvanizing processes. In these systems, ammonia crackers rely on an external heat supply and employ nickel-based catalysts supported on alumina, operating at temperatures typically in the range of 700–900 °C (L. Gavrilović, 2024).

To apply ammonia decomposition in power generation (ammonia-to-power) and to minimize the presence of ammonia in the outlet gas, several solutions have been proposed. First, the ammonia can be separated from the stream by cooling. To avoid lowering the gas temperature, ammonia capture materials have been used on porous supports, which can remove ammonia at high temperatures. Second, alternative fuel cells that are not affected by high levels of ammonia in the hydrogen stream could be used. In SOFCs, ammonia can be used directly as fuel at high temperatures, at which the decomposition occurs directly at the anode. Third, ammonia can be used directly as a fuel in gas turbines or engines, exploiting its high octane number (110–130). The main obstacle of these technologies is the emission of NO_x associated with the combustion of ammonia.

A major consideration when applying ammonia cracking on a large scale is the identification of appropriate methods to provide the heat necessary for the reaction. One approach consists of combusting a fuel gas to supply the required thermal energy. However, the problem with using conventional fossil fuels to sustain ammonia cracking is that it goes against the decarbonization goals associated with ammonia as a hydrogen carrier, as combustion of fossil fuels leads to significant CO_2 emissions. Therefore, in the literature, it has been suggested that a portion of the ammonia feed be combusted within the process battery limits. Although this solution can contribute to decarbonization targets, it requires a substantial fraction of ammonia to be consumed as fuel, resulting in a reduction of the net hydrogen yield. Based on the lower heating value of ammonia, approximately 20% of the inlet NH_3, together with about 2% of the produced hydrogen, must be burned to sustain the reaction (Elvira Spatolisano, 2023).

Consequently, research on this topic has proceeded in two main directions. On one side, the development of novel catalysts is being pursued, aiming to achieve high activities while operating at lower temperatures. On the other side, alternative routes for low-temperature NH_3 cracking are being explored, including plasma-assisted processes, solar-driven systems, and electrochemical approaches for H_2 production.

Since, from a thermodynamic standpoint, the ammonia cracking reaction is favored at low pressures, most experimental studies on new catalytic systems are conducted under atmospheric conditions. However, more recent investigations have also addressed the effect of operating at elevated pressures, motivated by practical

considerations related to hydrogen delivery, since the produced hydrogen must ultimately be compressed. In addition, increasing the operating pressure leads to higher space–time yields, a key parameter for reactor performance and process intensification.

1.2 Ammonia Decomposition Catalysts

Building on the considerations presented in the previous section, the focus is here placed on the catalytic systems employed for ammonia cracking. Despite extensive research efforts, both industry and academia are still actively seeking a catalytic system that combines high activity, long-term stability, and economic viability.

Historically, the ammonia dissociation has been extensively investigated in the context of ammonia synthesis, as it represents the reverse reaction within the same equilibrium system. Early investigations on transition metals, carried out empirically by Haber (Haber & Rossignol, 1913), identified iron and osmium as the most active catalysts (see Figure 2b). Subsequent improvements, together with the scarcity of osmium, led to iron becoming the transition metal of choice for industrial ammonia synthesis. (Mittasch & Frankenburg, 1950) Ruthenium, on the other hand, exhibited lower apparent activity for ammonia synthesis under the operating conditions employed, as its high catalytic activity promotes rapid attainment of thermodynamic equilibrium. Under such conditions, net ammonia formation is limited by thermodynamic equilibrium rather than by the occurrence of a concurrent decomposition reaction (see Figure 3a). Highly active Ru catalysts were subsequently developed through the incorporation of alkali promoters. The pronounced chemical and structural tunability of ruthenium, enabling optimization in both the forward and reverse reaction pathways, has motivated extensive investigation into Ru-catalyzed ammonia synthesis and decomposition over recent decades. (Stefan Peters, 2023) Afterwards, numerous other metals have been studied, including Cu, Ni, Co, Mo, Ir, Pt, Pd, and Rh (T. E. Bell, 2016), as well as bimetallic or multimetallic combinations, such as Co–Mo, Ni–Mo, Fe–Mo, Ni–Co, Co–Mo–Fe–Ni–Cu, Fe–Co, Ni–Fe, Ni–Pt, Ni–Pd, Ir–Ni, Cu–Zn, and bimetallic compositions with Ru (Shreya Mukherjee, 2018).

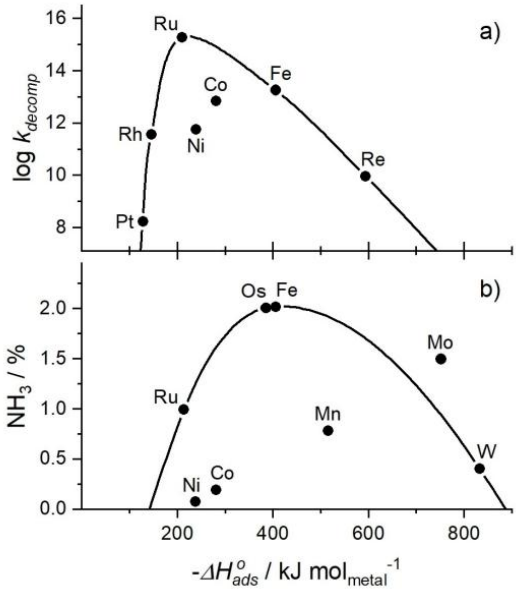

Figure 3, Logarithmic rate constants for ammonia decomposition at 673 K and 0.2–0.8 kPa (a) and ammonia yields at 773 K and 5 MPa (b) over different transition metals as a function of the dissociative adsorption enthalpy for molecular nitrogen (Stefan Peters, 2023)

In 2021, Lucentini et al. published an extensive work about the state-of-the-art of catalytic systems and their kinetic aspects. Among monometallic catalysts, ruthenium-based systems exhibit the highest intrinsic activity. It can reach a high conversion rate even at a comparatively low temperature of about 400 °C, outperforming other transition metals. These catalysts are typically supported on oxide materials or structured/unstructured carbon, but their practical use is limited by deactivation over time (Lucentini Ilaria, 2021). Furthermore, the high cost and scarcity of Ru (in 2024 the global demand stood around 35 tons (Ruthenium Market – Global Industry Analysis, Size, Share and Forecast, 2024)) make large-scale application economically challenging. Consequently, extensive research has focused on developing low-cost alternatives that can approach the performance of ruthenium while maintaining stability (T. E. Bell, 2016).

Noble metals, such as rhodium, iridium, platinum, and palladium, have been tested, but their catalytic activity hardly exceeds that of ruthenium. Nickel is the main non-noble metal alternative and currently leads the industrial standard for commercial ammonia crackers. Laboratory results show that Ni catalysts at the temperature range of 500-600 °C can give performances close to those of Ru (Lucentini Ilaria, 2021). Apart from these, other transition metals like iron, cobalt, and molybdenum have been considered to be active catalysts, with molybdenum frequently forming nitride phases, which during the reaction contribute to the catalytic activity.

The search for alternative catalytic materials has increasingly taken sustainability into account. Beyond the raw material cost, environmental considerations such as energy demand for extraction and refining, as well as the overall environmental impact of the catalyst, are gaining attention in the design of new systems. In general, economic cost and Global Warming Potential (GWP) exhibit an approximately linear correlation, as both are influenced by the natural abundance of elements in the Earth's crust. The low availability of the elements is typically accompanied by higher market prices and greater energy demands for extraction and processing. Consequently, materials with low geological availability, such as noble metals, are typically associated with higher costs and greater environmental impacts. This is well shown in Figure 4.

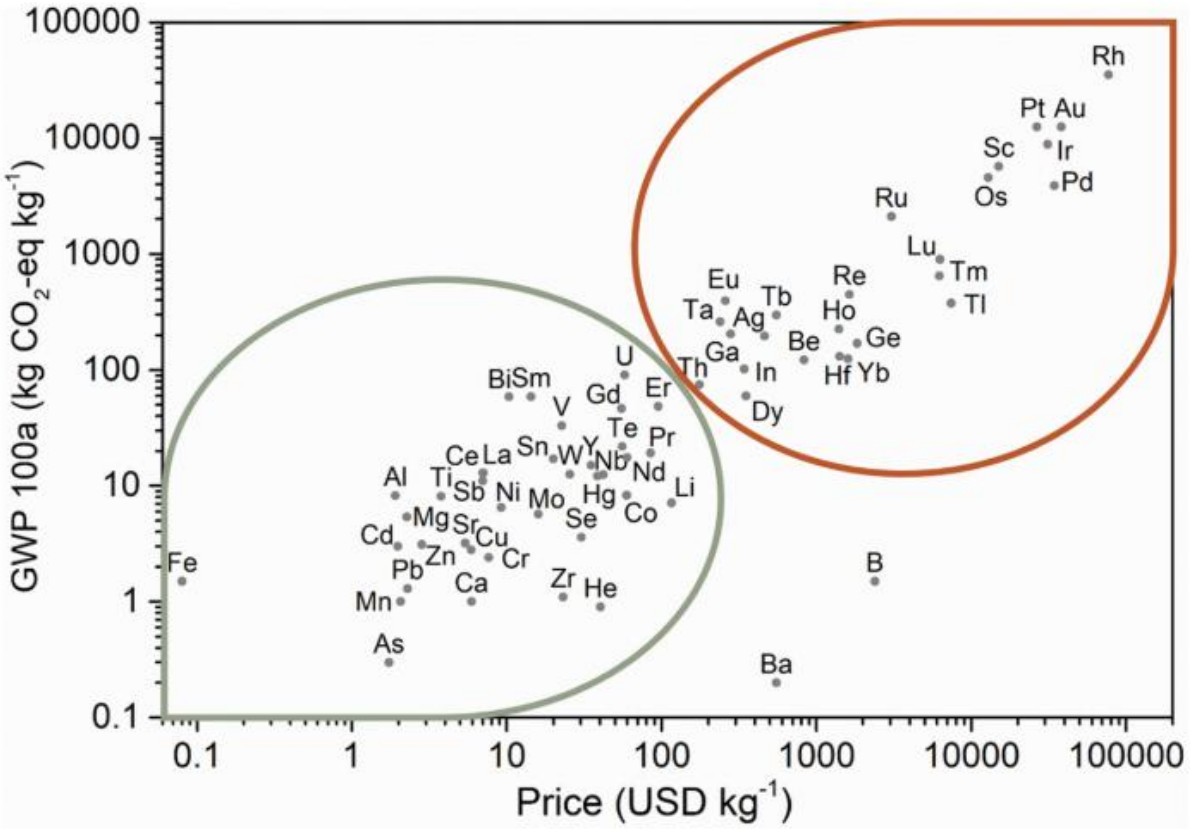

Figure 4, Comparison of the price and the global warming power on a 100-year basis of the elements (Lucentini Ilaria, 2021)

The efficiency of catalysts is governed not only by the nature of the active metal phase, but also by the characteristics of the support material and the presence of promoters. Catalytic performance is generally enhanced when high surface area supports are employed, as they enable improved metal dispersion and smaller particle sizes, particularly in combination with electron-donating promoters such as potassium, cesium, or barium (Enrique García-Bordejé, 2014). The support plays a key role in stabilizing the size and morphology of metal particles, thereby increasing the availability of exposed active sites, while simultaneously influencing the electronic properties of the supported metal species (T. E. Bell, 2016). Moreover, an increase in catalyst basicity has been shown to positively affect ammonia decomposition activity and to promote the formation of metal–nitrogen bonds with suitable bonding energies (Lucentini Ilaria, 2021).

A final aspect influencing catalytic performance in ammonia decomposition is the inhibitory role of hydrogen. As the reaction progresses along the catalytic bed, the increasing hydrogen partial pressure hinders the reaction by limiting the availability of active sites on the catalyst surface for ammonia adsorption and dissociation. Hydrogen inhibition represents a general and intrinsic limitation of ammonia cracking processes and becomes increasingly relevant at high conversion levels.

As a summary, at present, nickel supported on alumina represents the most widely used industrial catalyst, particularly for high-temperature operation, due to its mechanical strength, heat resistance, and scalability, even if its intrinsic activity is lower than that of Ru. Co–Fe or Fe-based catalysts are suited for intermediate

temperatures, while Ru-based systems enable operation at lower temperatures, but are economically prohibitive for industrial-scale applications. Consequently, significant effort is directed toward optimizing non-noble metal catalysts, alone or in combination with small amounts of noble metals. The choice of active phase, promoters, and support, with attention to basicity, thermal stability, conductivity, and surface area, is critical for achieving high performance.

1.3 Kinetics and Reaction Mechanism

In recent decades, the kinetics of ammonia decomposition have been the subject of extensive investigation for a wide range of catalytic systems, with the dual objective of defining reliable rate expressions and elucidating the underlying reaction mechanism. Early kinetic models commonly described ammonia decomposition using a simple first-order rate law with respect to ammonia partial pressure, an approach that is still occasionally adopted for engineering calculations and preliminary reactor design (Lucentini Ilaria, 2021). Subsequent studies refined this description by proposing rate expressions that transition between zero-order and first-order behavior depending on the operating temperature, reflecting changes in surface coverage and reaction regimes (Lucentini Ilaria, 2021).

More recent kinetic analyses, however, have clearly demonstrated that the reaction rate is significantly influenced by the presence of hydrogen in the reaction mixture. In particular, hydrogen has been shown to inhibit ammonia decomposition, an effect that becomes especially pronounced at lower temperatures (Shreya Mukherjee, 2018). This inhibition is generally attributed to the accumulation of hydrogen on the catalyst surface, which interferes with the adsorption and activation of ammonia and thus limits the overall reaction rate. As the reaction proceeds along the catalytic bed, hydrogen accumulates in the gas phase, progressively increasing product inhibition and reducing the availability of active sites for ammonia adsorption.

Three main approaches have been proposed to derive mechanistic rate expressions for ammonia decomposition. The first is the Langmuir–Hinshelwood–Hougen–Watson (LHHW) formulation, which is extensively applied and relies on the assumption of coverage-independent kinetic parameters (S. Armenise, 2013). A second framework is the Tamaru model, which postulates the existence of distinct kinetic regimes as a function of pressure and temperature. This approach was initially validated for W catalysts and later confirmed for Pt, VN, Mo_2N, and TiN_xO_γ systems (Lucentini Ilaria, 2021). Finally, the Temkin–Pyzhev model assumes associative nitrogen desorption as the rate-limiting step. When the influence of the reverse reaction can be neglected, the rate reduces to a power-law form, reflecting a non-uniform catalyst surface and a nitrogen coverage dependent on gas-phase composition (TEMKIN, 1979).

Within the framework of this thesis, particular attention is devoted to the Temkin–Pyzhev model. As proposed by Temkin, the mechanism considered for the decomposition of ammonia occurs following the opposite steps of ammonia synthesis and starts with the adsorption of ammonia on the catalyst surface, followed by subsequent dehydrogenation steps, and finally nitrogen and hydrogen atoms desorb as N_2 and H_2.

$$NH_{3(g)} + s \leftrightarrows NH_{3(a)}$$

$$NH_{3(a)} + s \leftrightarrows NH_{2(a)} + H_{(a)}$$

$$NH_{2(a)} + s \leftrightarrows NH_{(a)} + H_{(a)}$$

$$NH_{(a)} + s \leftrightarrows N_{(a)} + H_{(a)}$$

$$2N_{(a)} \leftrightarrows N_{2(g)} + 2s$$

$$2H_{(a)} \leftrightarrows H_{2(g)} + 2s$$

Here, s represents an empty site on the catalyst surface, and the subscript (a) refers to a species adsorbed on the surface.

Drawing analogies with ammonia synthesis, where nitrogen dissociation is generally considered the rate-limiting step, early investigations suggested that recombinative desorption of N_2 constitutes the rate-determining step (RDS) for ammonia decomposition over many metallic catalysts. Subsequent experimental and theoretical

studies, however, have demonstrated that no universal rate-determining step can be identified. As a general remark, ammonia decomposition over noble metals is typically limited by the cleavage of N–H bonds, whereas over non-noble metals the desorption of N_2 generally governs the overall rate (Elvira Spatolisano, 2023).

The nature of the catalyst support has also been shown to exert a strong influence on the reaction. As an illustrative example, Nakamura et al. found that in Ni-based catalysts, the turnover frequency depends on the nature of the metal oxide support, indicating support-induced modifications of the active sites. Accordingly, the N_2 desorption temperature varies with the support, reflecting changes in Ni–N binding energy. A volcano-type relationship between turnover frequency and N_2 desorption temperature was observed, indicating that ammonia decomposition activity and the rate-determining step are governed by the Ni–N interaction strength as a function of the support (Isao Nakamura, 2016).

The overall reaction rate equation for ammonia decomposition can be expressed as follows (El-Shafie, 2023).

$$r = k_1 p_{N2} \left(\frac{p_{H_2}^3}{p_{NH_3}^2} \right)^{\alpha} - k_2 \left(\frac{p_{NH_3}^2}{p_{H_2}^3} \right)^{1-\alpha}$$

In this equation

- r (SI unit: mol/(m^3·s)) is the reaction rate.
- k_1 (SI unit: mol/(m^3·s·$Pa^{1+\alpha}$)) is the forward reaction rate constant.
- k_2 (SI unit: (mol·$Pa^{1-\alpha}$)/(m^3·s)) is the reverse reaction rate constant.
- p_i (SI unit: Pa) is the partial pressure of the element i.
- α (dimensionless) is the Temkin–Pyzhev empirical parameter associated with the forward reaction term.

The parameter α typically ranges from 0.5 to 0.8, depending on the extent of nitrogen adsorption.

1.4 Reactor Concepts for Ammonia Cracking

A wide range of reactor technologies has been proposed for ammonia cracking, including catalytic fixed-bed reactors, fluidized beds, membrane reactors, plasma-assisted systems, microwave reactors, as well as multistage and hybrid configurations (Elvira Spatolisano, 2023; Korawich Trangwachirachai, 2024; Hossein Ali Yousefi Rizi, 2022).

Reactor selection is primarily governed by thermal requirements, operating temperatures, hydrogen purity, and production scale. These factors determine the suitability of different configurations for continuous industrial operation. This section reviews the main ammonia cracking reactor concepts to contextualize the fixed-bed thermocatalytic reactor investigated in this work. The focus is on technologies compatible with steady-state operation and industrial scalability, while alternative concepts are discussed for comparison.

Independent of the specific reactor technology, the performance of ammonia cracking systems is governed by a set of strongly coupled parameters, including reactor geometry and size, ammonia partial pressure, pressure drop, axial and radial temperature gradients, gas residence time, and, where applicable, sweep gas flow rates. These parameters directly affect reaction kinetics, heat and mass transfer limitations, and ultimately determine ammonia conversion and hydrogen productivity (Hossein Ali Yousefi Rizi, 2022).

In thermally driven ammonia cracking processes, reactor design must therefore address not only catalytic activity but also the effective integration of a high-temperature heat supply system. Consequently, advances in reactor technology play a role comparable to catalyst development in overcoming transport limitations and enabling efficient operation under industrially relevant conditions.

1.4.1 Thermocatalytic Cracking Reactors

A schematic representation of a typical thermocatalytic ammonia cracking process is shown in Figure 5.

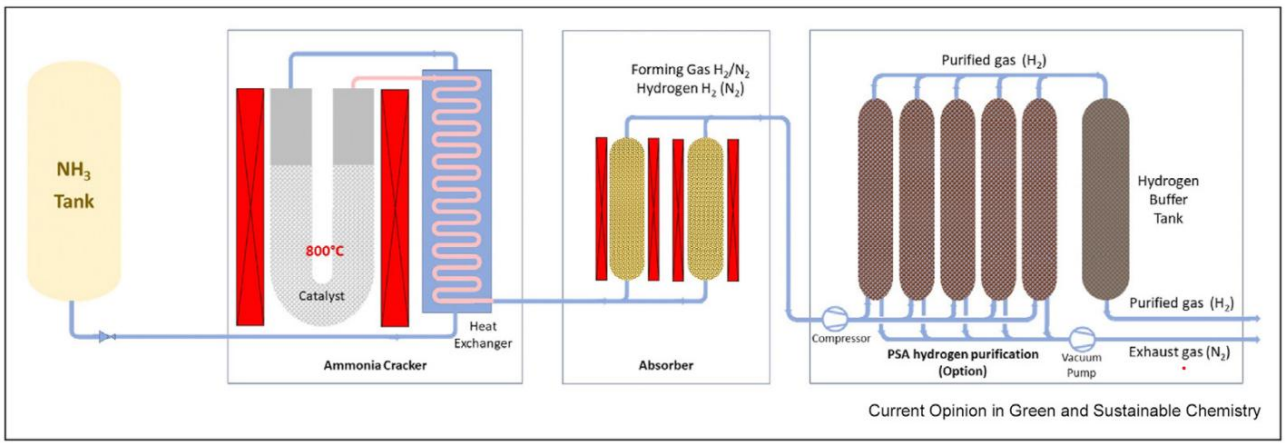

Figure 5, Schematic diagram of ammonia cracking process (Korawich Trangwachirachai, 2024).

Liquid or gaseous ammonia is fed to a high-temperature catalytic reactor, where it is decomposed into a hydrogen–nitrogen mixture over a solid catalyst. Given the strong thermal demand of the reaction, the reactor is coupled with a dedicated heat supply system, which may consist of external burners, electrical heaters, or integrated heat exchangers. Downstream of the reactor, heat recovery is commonly implemented to improve overall process efficiency, followed by optional hydrogen purification units such as pressure swing adsorption (PSA) systems, depending on the required hydrogen purity.

Fixed Bed Reactors

Fixed-bed reactors represent the most established reactor concept for thermocatalytic ammonia cracking and are widely regarded as a reference configuration for industrial implementation. Their design and operation are closely related to those of steam methane reforming units, with ammonia replacing the hydrocarbon feedstock and decomposition occurring over a packed catalytic bed at high temperature (Camel Makhloufi, 2021).

In fixed-bed ammonia crackers, high operating temperatures are required to overcome the endothermic nature of the ammonia decomposition reaction and to achieve significant conversion levels. Typical operating temperatures reported in the literature range between 600 and 900 °C (Hossein Ali Yousefi Rizi, 2022), depending on catalyst formulation and space velocity. The catalyst is generally packed in tubular or multitubular reactor geometries, enabling continuous operation and high hydrogen throughput (Korawich Trangwachirachai, 2024).

Heat supply to the reactor is a critical design aspect. In furnace-heated fixed-bed reactors, the required heat is usually supplied by external burners, where ammonia and a portion of the produced hydrogen are burnt as fuels (Camel Makhloufi, 2021). Electrically heated fixed-bed reactors, on the other hand, rely on direct electrical energy input to keep the reaction temperature and allow fast start-up and operation, flexible to load changes (Korawich Trangwachirachai, 2024). These heating modes directly affect temperature profiles along the packed bed and, thus, reactor performance.

Despite their technological maturity, fixed-bed reactors are inherently affected by heat and mass transfer limitations. Poor radial and axial heat transfer within the packed bed often leads to significant temperature gradients along the reactor length, particularly at high operating temperatures (Hossein Ali Yousefi Rizi, 2022). Since ammonia decomposition kinetics are strongly temperature-dependent, these gradients have a direct impact on local reaction rates and overall ammonia conversion. In addition, mass transfer limitations and non-ideal residence time distributions may arise at elevated space velocities, deviating from ideal plug-flow behavior (Hossein Ali Yousefi Rizi, 2022).

Fluidized Bed Reactors

Fluidized-bed reactors offer significant advantages in terms of heat and mass transfer, ensuring high temperature uniformity within the catalytic bed. This configuration is particularly beneficial for managing the high endothermicity of ammonia cracking and allows for continuous catalyst regeneration in case of deactivation. In fluidized-bed membrane reactors (FBMRs), reactor performance is influenced by phenomena such as the sweep gas effect, bubble-to-emulsion mass transfer, densified zone formation, and concentration polarization (Lucentini Ilaria, 2021). Moreover, the membrane-assisted fluidized bed reactor has good gas–solid contact and heat and

mass transfer characteristics, which can increase catalytic reforming and improve hydrogen production. However, conventional Pd-based fluidized bed membrane reactors (FBMR) are not suitable for ammonia decomposition due to their low performance under the same operating conditions. Also, due to weight, volume, and start-up time, they are not applicable for PEM fuel cells in on-board hydrogen production (Hossein Ali Yousefi Rizi, 2022).

Membrane Reactors

Membrane reactors represent an advanced reactor configuration for the thermocatalytic cracking of ammonia. In these systems, ammonia decomposition takes place over a solid catalyst while hydrogen is simultaneously separated through a hydrogen-permeable membrane integrated into the reactor. The combination of reaction and separation within a single unit enables a more efficient utilization of both catalytic activity and thermodynamic driving forces.

The continuous removal of hydrogen from the reaction zone shifts the equilibrium of the ammonia decomposition reaction toward the products, in accordance with Le Chatelier's principle. In addition to this thermodynamic effect, the reduction of hydrogen partial pressure mitigates product inhibition effects, leading to an increase in the net reaction rate. As a result, membrane reactors can achieve ammonia conversions comparable to those of conventional fixed-bed reactors at lower temperatures, or higher conversions at the same operating temperature.

Typical membrane reactor designs employ tubular hydrogen-selective membranes coupled with either a packed catalytic bed or a catalytic layer deposited on porous supports. Both ceramic-supported and metallic membrane configurations have been investigated, depending on the operating temperature and process requirements. Among the available options, palladium-based and Pd-alloy membranes are the most widely studied (Hossein Ali Yousefi Rizi, 2022; El-Shafie, 2022; Valentina Cechetto, 2021).

The integration of a hydrogen-selective membrane into a thermocatalytic ammonia cracking reactor enables conversions beyond thermodynamic equilibrium limitations. In a study conducted by Valentina Cechetto et al., at temperatures above 425 °C, ammonia conversion values higher than 86% have been reported, while simultaneously achieving hydrogen purities up to 99.998%. The use of a vacuum on the permeate side of the membrane strengthens the driving force for hydrogen separation, thereby increasing hydrogen recovery and further increasing ammonia conversion.

From a reactor engineering perspective, membrane reactors introduce additional design complexity compared to conventional fixed-bed reactors. As a result, despite their clear conceptual advantages, membrane reactors remain less mature for large-scale ammonia cracking than conventional thermocatalytic fixed-bed configurations.

Small-scale Reactor Designs

In addition to conventional fixed-bed and membrane-assisted reactors, several alternative thermocatalytic configurations for ammonia cracking have been explored, mainly in the context of small-scale and portable hydrogen production. These include microfabricated and monolithic reactors, which have been investigated for ammonia decomposition under atmospheric pressure and low flow-rate conditions.

Different microreactor concepts, such as micropost and microchannel reactors, have been compared in the literature. Reported ammonia conversions range from about 85% for micropost reactors operated at 650 °C and low flow rates, up to approximately 97% for microreactors operating between 400 and 700 °C (Hossein Ali Yousefi Rizi, 2022). At these scales, parameters such as packed-bed porosity and permeability are not considered of major engineering importance and do not significantly affect reactor performance.

Microwave-assisted reactors represent another alternative approach for thermocatalytic ammonia cracking. Due to selective heating effects, these systems can achieve high ammonia conversion at lower apparent reaction temperatures by directly transferring energy from the microwave field to the catalytically active surface. Nevertheless, limitations related to energy efficiency and scalability currently restrict their application to laboratory-scale studies.

1.4.2 Other Ammonia Cracking Technologies

In addition to thermocatalytic ammonia cracking, several alternative technologies have been investigated for hydrogen production from ammonia, based on different physical and chemical principles. These technologies are briefly described, focusing on their operating principles.

Electrolysis

In order to address concerns related to the energy efficiency of hydrogen production, ammonia electrolysis has been proposed as a viable alternative. Electrolytic ammonia decomposition has the advantage of allowing hydrogen generation at room temperature. Ammonia electrochemical decomposition can be performed using different electrolyte systems, including aqueous media operating under acidic or alkaline conditions, as well as non-aqueous electrolytes. A comprehensive review addressing the ammonia electro-oxidation reaction, with a specific focus on reaction mechanisms and electrocatalyst design, was reported by Siddharth et al. in 2018. The reaction kinetics of ammonia electro-oxidation are governed by surface-sensitive mechanisms involving sequential dehydrogenation steps and the formation of adsorbed intermediates.

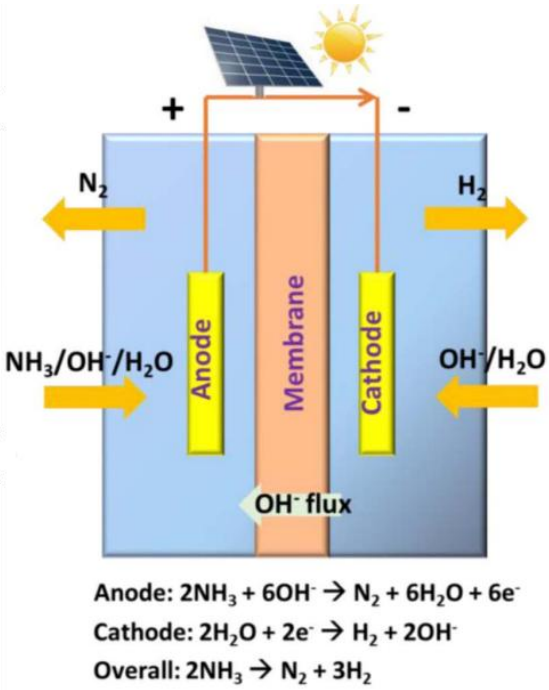

Figure 6, Schematic of a typical ammonia electrolysis cell for hydrogen generation (Nadia Mohd Adli, 2018)

In aqueous systems, ammonia electrolysis is a pH-dependent process, involving NH_3 oxidation by OH^- ions under alkaline conditions. Platinum remains the benchmark electrocatalyst (Elvira Spatolisano, 2023), owing to its near-optimal nitrogen binding strength in accordance with the Sabatier principle. However, its practical application is limited by surface poisoning phenomena and by competition with the oxygen evolution reaction at high potentials (Elvira Spatolisano, 2023).

Photocatalysis

Photocatalysis has gained attention because of its potential to promote the NH3 dissociation reaction at room temperature, which is particularly relevant, considering the high endothermicity of conventional catalytic ammonia cracking. The process exploits the photoenergy for the production of photoexcited electrons (e−) and holes (h+), involving the use of a photocatalyst, typically a semiconductor material. Very few works are available in the literature regarding the photocatalytic decomposition of NH3 to H2. NH3 photocatalytic decomposition suffers from undesired nitrogen oxide production, which is detrimental to the process H2 yield. Much work has to be done to identify a suitable photocatalyst with good activity and stability, high surface area, and simple synthesis approach. Also, the photocatalytic efficiency is still too low for practical industrial applications (Elvira Spatolisano, 2023).

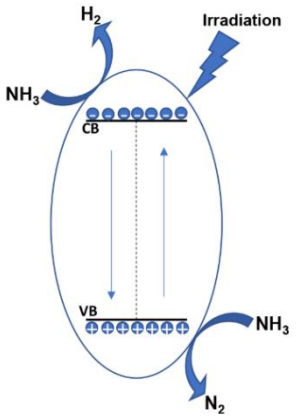

Figure 7, Schematic of photocatalytic ammonia decomposition (Elvira Spatolisano, 2023)

Ammonia Reforming

To provide the NH_3 dissociation reaction heat, one possible solution is ammonia reforming. In this case, part of the NH_3 is oxidized to provide the energy needed by the NH_3 decomposition, such that the endothermic NH_3 cracking can be self-sustained through the heat generated in the oxidation phase. The process proceeds as reported,

$$NH_3 + x\,O_2 \rightarrow 2x\,H_2O + (1.5 - 2x)H_2 + 0.5\,N_2$$

where x is the stoichiometric coefficient of oxygen, which must be lower than 0.75 to ensure H_2 production. While catalyst synthesis and formulation are not commonly perceived as a critical issue, the main concerns regarding the process scalability are related to the process heat management. Heat generated in the combustion section must be effectively transferred to the reforming section to enable NH_3 conversion to H_2 and N_2.

None of the considered alternatives were demonstrated at a scale different from the laboratory one, thus opening issues related to the process scalability, mostly regarding effective heat transfer on a larger scale. In this respect, microchannel reactor technology is supposed to be easily scaled up and convenient for modularized plants (Elvira Spatolisano, 2023). The table below summarizes the analyzed technologies, indicating their Technology Readiness Level (TRL) and highlighting the associated advantages and disadvantages.

technology	TRL	pros	cons
Thermocatalytic (Ru-based catalysts)	3–4	• Most studied active species • Highly active even at low temperatures (lowest activation energy)	• Very expensive → research efforts devoted to reducing the noble metal loading • High GWP, directly proportional to the noble metal scarcity
Thermocatalytic (Non-Ru-based catalysts)	8–9 (for Ni-based)	• Cheaper than Ru-based catalysts • Ni-based catalysts very mature technology on small scale • Good heat resistance and stability	• Higher reaction temperature needed than Ru-based catalysts
Amide-imide catalysts	3–4	• Can favor the low temperature NH_3 decomposition (T < 450 °C) • Conversion comparable to Ru-based catalysts	• Difficulty to keep the catalyst in solid phase at the reaction condition → loss of catalytic material. This problem can be solved considering a combination of 2 transition metals • The catalyst reacts with the support • Not clear reaction mechanism → effect of the reactor wall
Reforming	3–4	• Can sustain the endothermicity of the NH_3 dissociation reaction	• $DeNO_x$ system needed for NO_x abatement • Proper reactor design necessary to maximize heat transfer
Electrolysis	3	• Low reaction temperature • High faradaic efficiency with less energy needed than that for water electrolysis	• Applied current density must be further increased to sustain the low cell voltage and the durability of the electrolytic cell • High over potential in the case of non-noble metal catalysts which leads to unwanted side reactions
Photocatalysis	3	• Green process → can be driven by solar energy • Low temperature (T ambient) • No direct CO_2 emissions associated	• Most of the available photocatalyst suffer from poor activity, low stability, low surface area, complicated synthesis approach • NO_x generated that lower the yield in hydrogen • Low NH_3 concentration

Figure 8, Summary of the Analyzed Technologies with Related Pros/Cons (Elvira Spatolisano, 2023)

2. COMSOL Multiphysics® Reactor Modeling

COMSOL Multiphysics® (COMSOL) is a numerical simulation environment designed to solve engineering problems governed by partial differential equations (PDEs). The software is based on the finite element method and allows the simultaneous solution of coupled transport, thermal, and reaction phenomena within complex geometries (COMSOL AB, 2015). Its multiphysics formulation enables the consistent coupling of fluid flow, mass transport, heat transfer, and chemical reactions, which is particularly suitable for the modeling of catalytic reactor systems. The simulations presented in this work were performed using COMSOL version 5.2.

In the present work, the reactor is modeled at a macroscopic scale, resolving mass, momentum, and energy balances in the packed bed and surrounding free-flow regions. The software accommodates temperature and concentration-dependent reaction kinetics and provides the flexibility to implement complex reaction mechanisms such as the Temkin–Pyzhev ammonia decomposition rate law. While the model does not resolve intra-pellet concentration gradients, it accounts for macroscopic transport limitations due to porosity, tortuosity, and flow resistance in the packed bed.

This chapter is structured as follows. Section 2.1 introduces the theoretical background of the finite element method. The development of the CFD model is then presented, starting from the reactor geometry definition (Section 2.2) and mesh generation (Section 2.3). Finally, the governing equations describing mass transport with chemical reactions and heat transfer are introduced in Sections 2.4 and 2.5, respectively.

2.1 Finite Elements Basics

This section introduces the finite element method (FEM) as a general numerical framework for the solution of partial differential equations (PDEs). The core idea of the FEM is to approximate the solution of a continuous problem by reformulating it over a discretized representation of the spatial domain. The computational domain is divided into a finite number of subregions, referred to as elements, which together constitute the computational mesh, over which the solution is locally approximated using a limited set of degrees of freedom (DOFs).

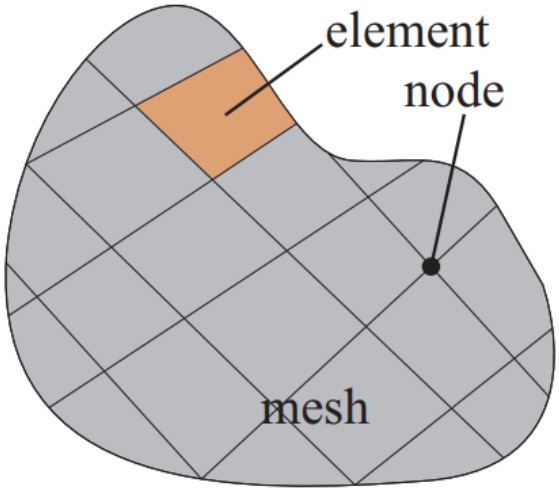

Figure 9, Mesh discretization of a 2D domain using FEM

Within this framework, the governing physical laws are not solved pointwise over the entire domain, but rather enforced in an integral sense over each element. The local approximations are then systematically assembled to obtain a global system of algebraic equations describing the behavior of the system across the whole domain.

This approach allows complex geometries, heterogeneous materials, and coupled physical phenomena to be treated within a unified numerical formulation (COMSOL AB, 2015). The finite element method was originally developed for structural mechanics (N. Bartal, 2009) and later extended to a wide range of engineering applications, including transport and reaction problems.

The fundamental steps of the FEM can be summarized as follows. Since the strong form of a PDE does not admit an analytical solution for complex engineering problems, the governing equations of the system are rewritten in the so-called weak form. In general, the weak form is derived by multiplying the strong form by a test function, integrating over the domain, and applying integration by parts to the terms involving derivatives. This process reduces the order of the derivatives and typically yields a more symmetric formulation, which is advantageous for numerical solution (O Colomés, 2023–2024). The weak form is then discretized by restricting the solution space to a finite number of DOFs and therefore reducing the infinite set of equations to a finite algebraic system. The approximate solution is calculated using a finite set of shape functions, each of which is linked to a nodal DOF. The specific definition of the shape functions depends on the element type and problem dimensionality. However, the underlying approximation principle remains the same. An example of interpolation using piecewise linear polynomials is shown in Fig. 10.

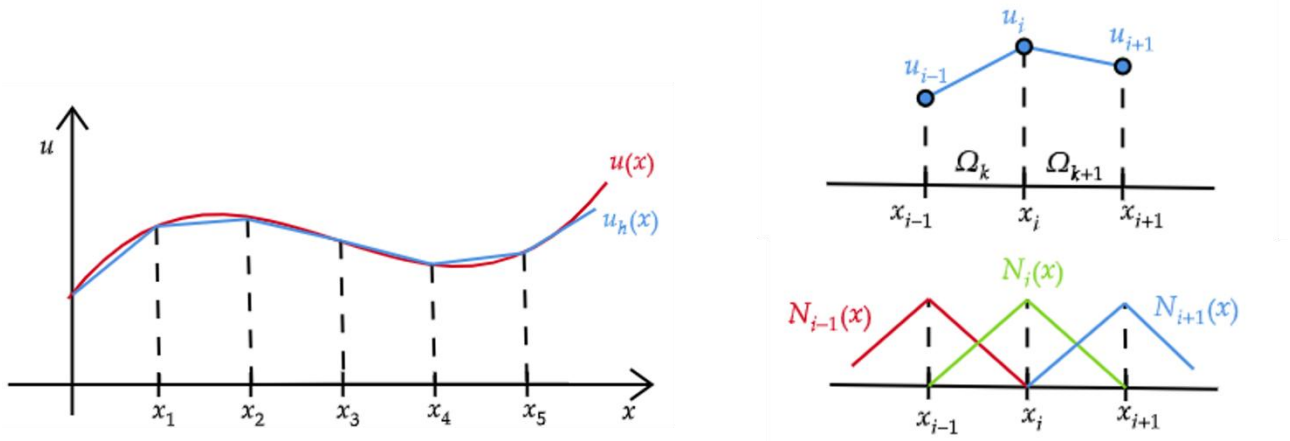

Figure 10, Interpolation of a function using piece-wise linear polynomials (left), approximated solution around node i (top-right) and shape functions for nodes $i-1$, i and $i+1$ (bottom-right). (O Colomés, 2023–2024)

2.2 Geometry

The modeled system represents a fixed-bed catalytic reactor related to a real lab scale reactor used by the research group. The reactor consists of a vertical glass tube, which has an inner diameter of 7 mm and a wall thickness of 1 mm. The catalytic bed is positioned at the tube mid-height and has an axial extension of 10 mm. Surrounding this bed region, the reactor is equipped with an external heating system that covers approximately 150 mm of tube height, centered around the catalyst zone.

Given the cylindrical symmetry of the reactor and the absence of azimuthal variations, the simulation was performed using a 2D axisymmetric formulation. This choice significantly reduces the computational cost while preserving the accuracy of the physical description.

To reproduce the actual laboratory reactor, the cross-section was assembled by combining a set of rectangular primitives. Each rectangle corresponded to one structural or functional portion of the reactor. Once the primitives were defined, a Boolean Union operation was applied to merge them into a single computational domain. The final geometry thus consists of four main subdomains: the fluid region, the porous catalytic bed, the heated glass wall, and the unheated glass wall.

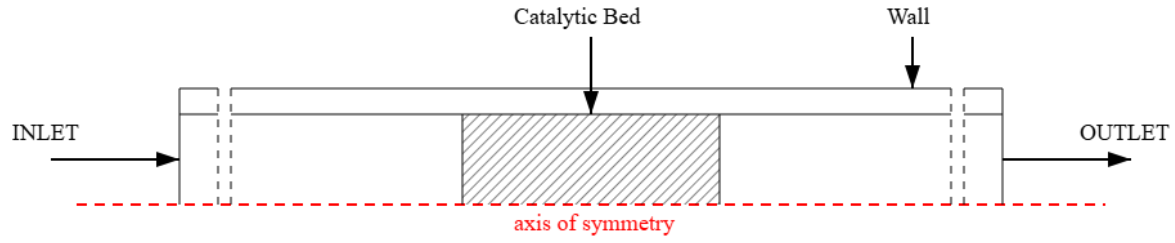

Figure 11, Geometry of the reactor

2.3 Mesh Generation

The mesh provides the discrete support for the numerical solution of the governing equations. The mesh generator discretizes the domains into triangular or quadrilateral mesh elements. In this work, the domain was discretized using a free triangular mesh, consistent with the default option for arbitrary 2D geometries.

To set the local element size, COMSOL provides predefined fluid dynamics calibrations, which adjust the characteristic element lengths following typical requirements of flow simulations. As described in the previous section, the reactor geometry consists of distinct regions with different physical behavior, making uniform meshing inefficient.

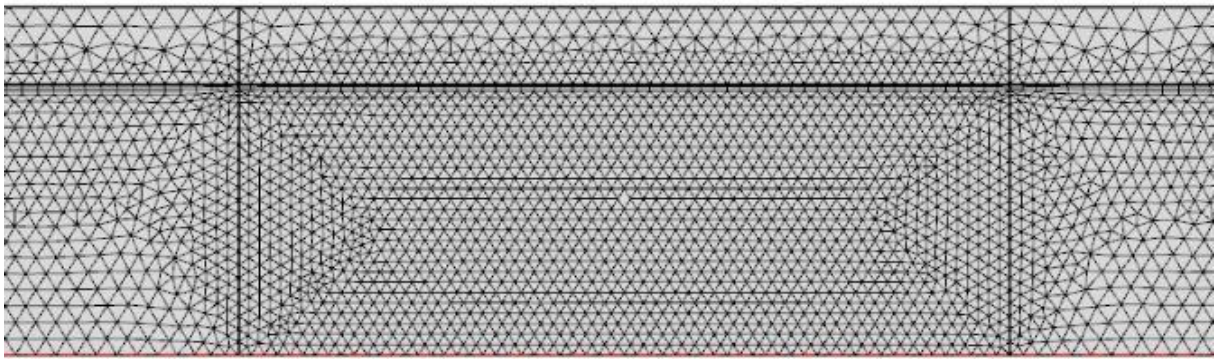

Figure 12, Example of mesh refinement

The catalytic bed was assigned a finer discretization due to the presence of strong temperature and concentration gradients induced by the reaction. Additional refinement was applied near the reactor wall. The no-slip boundary condition generates steep velocity gradients in the radial direction, while conjugate heat transfer between the wall and the fluid produces sharp temperature gradients. A locally refined mesh was therefore introduced in the near-wall region to accurately resolve these boundary-layer effects.

A mesh independence study was subsequently performed to verify that the numerical solution is not affected by the chosen discretization. The results of this analysis are presented in section “3.1.1 Mesh Independence Analysis”.

2.4 Reacting Flow Modeling

In the present work, the transport of chemical species and the ammonia decomposition reaction within the reactor are modeled by coupling fluid flow in free and porous media with multicomponent mass transport. The adopted formulation accounts for the simultaneous effects of convection, diffusion, and chemical reaction.

The catalytic bed is modeled as a porous medium, while the upstream and downstream regions are treated as free-flow domains. Since the inlet stream consists of pure ammonia and the system does not include a solvent component, all species present in the system contribute significantly to the mixture properties and must be treated on an equal footing. Species transport is therefore described using a concentrated-mixture formulation, in which the mass fractions of all chemical species are solved, and mixture properties depend on the local composition.

Based on these considerations, the model employs the RFCS (Reacting Flow Concentrated Species) framework, which couples the Brinkman equations for fluid flow in porous media with a transport model for concentrated species (COMSOL AB, 2015). This approach enables a consistent description of momentum and mass transport in both the catalytic bed and the adjacent free-flow regions, while accounting for the local production and consumption of species due to chemical reactions.

2.4.1 Governing Equations

The governing equations describing multicomponent species conservation in reacting mixtures, as well as momentum transport in free and porous media, are summarized below. The basic equation for the conservation of mass of a species i is:

$$\frac{\partial}{\partial t}(\rho\omega_i) + \nabla \cdot (\rho\omega_i \boldsymbol{u}) = -\nabla \cdot \boldsymbol{j}_i + R_i$$

Using the continuity equation, the equation can be re-cast in its non-conservative form, which is the formulation adopted in the RFCS framework.

$$\rho\frac{\partial}{\partial t}(\omega_i) + \rho(\boldsymbol{u} \cdot \nabla)\omega_i = -\nabla \cdot \boldsymbol{j}_i + R_i$$

In these equations,

- t (SI unit: s) is the time.
- ρ (SI unit: kg/m^3) is the density of the mixture.
- ω_i (dimensionless) is the mass fraction of species i.
- **u** (SI unit: m/s) is the velocity vector of the mixture.
- $\boldsymbol{j}_i$ (SI unit: kg/(m^2·s)) is the diffusive mass flux of species i.
- R_i (SI unit: kg/(m^3·s)) is the net rate of production or consumption of species *i* due to chemical reactions.

The Brinkman formulation, adopted to describe the momentum balance, extends Darcy's law by including viscous shear effects, allowing a smooth transition between porous and non-porous domains (COMSOL AB, 2015). This is particularly important in the present geometry, where the catalytic bed is embedded within a continuous flow channel. The continuity and momentum equations, which are written in a unified form that is valid both inside the porous bed and in the free-flow regions, are the following.

$$\frac{\partial}{\partial t}(\varepsilon_p\rho) + \nabla \cdot (\rho\,\boldsymbol{u}) = Q_m$$

$$\frac{\rho}{\varepsilon_p}\left(\frac{\partial \boldsymbol{u}}{\partial t} + \frac{(\boldsymbol{u} \cdot \nabla)\boldsymbol{u}}{\varepsilon_p}\right) = -\nabla \mathrm{p} + \nabla \cdot \left[\frac{1}{\varepsilon_p}\left\{\mu(\nabla\boldsymbol{u} + (\nabla\boldsymbol{u})^T) - \frac{2}{3}\mu(\nabla \cdot \boldsymbol{u})\boldsymbol{I}\right\}\right] - \left(\kappa^{-1}\mu + \frac{Q_m}{\varepsilon_p^2}\right)\boldsymbol{u} + \boldsymbol{F}$$

In these equations:

- μ (SI unit: kg/(m·s)) is the dynamic viscosity of the fluid.
- **u** (SI unit: m/s) is the velocity vector.
- ρ (SI unit: kg/m^3) is the density of the fluid.
- p (SI unit: Pa) is the pressure.
- ε_p (dimensionless) is the porosity.
- κ (SI unit: m^2) is the permeability of the porous medium.
- Q_m (SI unit: kg/(m^3·s)) is a mass source or sink. The mass source accounts for mass deposit and mass creation within the domains. The mass exchange is assumed to occur at zero velocity.
- **F** (SI unit: N) represents the external body forces.

2.4.2 Diffusion Model

The Transport of Concentrated Species interface always accounts for transport due to diffusion. The available diffusion models are Maxwell–Stefan, Mixture-averaged, and Fick's law (COMSOL AB, 2015).

In this work, multicomponent diffusion was described using the Maxwell–Stefan formulation, which represents the most rigorous physical model available in COMSOL for gas-phase mixtures. The choice is motivated by the following reasons. Ammonia decomposition generates a mixture rich in hydrogen, and the diffusivities of H_2, N_2, and NH_3 differ up to one order of magnitude. These strong disparities and the steep concentration gradients along the reactor cause pronounced counter-diffusion phenomena and significant coupling between fluxes of different species. Simplified models such as Fick's law or the mixture-averaged approach would fail to capture these

interactions because they neglect the interspecies friction forces, which are central to multicomponent systems with high conversion.

To evaluate the binary diffusivities, needed to compute the Maxwell–Stefan matrix, the Fuller–Schettler–Giddings correlation was used (Edward N. Fuller, 1966). For gases, the binary diffusivity, expressed in m^2/s, is given by the following relation.

$$D_{A,B} = \frac{10^{-7} T^{1.75} \left(\frac{1}{M_A} + \frac{1}{M_B}\right)^{1/2}}{p\left[\left(\sum_A v_i\right)^{1/3} + \left(\sum_B v_i\right)^{1/3}\right]^2}$$

Where

- T (SI unit: K) is the absolute temperature.
- M_A (SI unit: kg/mol) is the molar mass of species A.
- M_B (SI unit: kg/mol) is the molar mass of species B.
- p (SI unit: Pa) is the total pressure of the system.
- v_i (dimensionless) are the diffusion volumes of the atomic or molecular groups composing the species.
- $\sum_A v_i$ (dimensionless) is the sum of the diffusion volumes of species A.
- $\sum_B v_i$ (dimensionless) is the sum of the diffusion volumes of species B.

This correlation is widely accepted for non-polar gases at moderate pressures and elevated temperatures, conditions that match the operating window of the reactor. Temperature-pressure-dependent binary diffusivities were defined as COMSOL analytic functions and subsequently arranged into the symmetric Maxwell–Stefan matrix, with unit values on the diagonal as required by the formulation.

2.4.3 Transport Properties and Reaction Term

The following section describes the methodology adopted for the computation of the physical and chemical properties required for the implementation of the model.

The density is computed from the ideal gas law in the manner of:

$$\rho = \frac{\mathrm{p}\, M}{R_g T}$$

Where

- p (SI unit: Pa) is the pressure of the system.
- M (SI unit: kg/mol) is the molar mass of the gas mixture.
- R_g (SI unit: J/(mol·K)) is the universal gas constant.
- T (SI unit: K) is the absolute temperature.

The mixture's dynamic viscosity follows Wilke's mixing rule

$$\mu = \sum_i \frac{x_i \mu_i}{\sum_j x_i \Phi_{ij}}$$

with interaction terms (Φ_{ij}) computed as

$$\Phi_{ij} = \frac{1}{\sqrt{8}} \left(1 + \frac{\mu_i}{\mu_j}\right)^{-\frac{1}{2}} \left(1 + \sqrt{\frac{M_i}{M_j}}\right)^2$$

Where

- μ_i (SI unit: kg/(m·s)) is the dynamic viscosity of species i.
- μ_j (SI unit: kg/(m·s)) is the dynamic viscosity of species j.
- x_i (dimensionless) is the mole fraction of species i.

- M_i (SI unit: kg/mol) is the molar mass of species i.
- M_j (SI unit: kg/mol) is the molar mass of species j.

Since mass transport within the catalytic bed is hindered by the presence of a solid porous structure, the transport properties must be corrected to account for porosity effects. The porosity used in the model corresponds to the macroscopic interparticle porosity of the packed bed:

$$\varepsilon_p = 1 - \frac{\rho_b}{\rho_{pe}}$$

where ρ_b is the bulk bed density and ρ_{pe} is the pellet density. In the present work, the porosity is assumed to be uniform throughout the catalytic bed and is set to a constant value of 0.794.

The reduction of diffusive transport in the packed bed due to the porous structure is accounted for through an effective transport factor, defined as a function of porosity and fluid tortuosity as follows:

$$f_e = \frac{\varepsilon_p}{\tau_F}$$

The fluid tortuosity factor is assumed to be constant and equal to 4, in accordance with typical values reported in the literature for heterogeneous catalytic structures.

Flow resistance in the packed bed is described through the permeability κ, calculated using the Kozeny–Carman equation (Kozeny, 1927), which is appropriate for low-Reynolds-number flow in beds of approximately spherical particles:

$$\kappa = \varphi_s^2 \frac{\left(\varepsilon_p^3 \, d_p^2\right)}{\left(150\left(1-\varepsilon_p\right)^2\right)}$$

Where

- φ_s (dimensionless) represents the sphericity of the particles
- d_p (SI unit: m) is the diameter of the volume equivalent spherical particle
- ε_p (dimensionless) is the macroscale porosity of the bed

Ammonia decomposition kinetics are described using a Temkin–Pyzhev rate expression. As the reaction rate is defined on a mass-of-catalyst basis, expressed in mol(NH_3)/($kg_{catalyst}$·s), whereas the numerical model requires a volumetric source term in units of kg/(m^3·s), an appropriate unit conversion is performed. The rate is therefore computed as:

$$R_i = \nu_i \, M_i \, \rho_{bulk} \, r$$

Where

- ν_i (dimensionless) is the stoichiometric coefficient
- M_i (SI unit: kg/mol) is the molar mass
- ρ_{bulk} (SI unit: $kg_{catalyst}/m^3$) is the bulk density of the catalyst

2.5 Heat Transfer Modeling

To model heat transport in a porous medium at the macroscopic scale, different approaches are available, depending on the validity of the local thermal equilibrium (LTE) hypothesis and the required level of accuracy for thermal effects in the solid phase. The classical LTE hypothesis assumes pointwise equality of solid and fluid temperatures within the porous medium.

When the LTE assumption is not valid or cannot be confidently assessed, it is necessary to define two separate heat-transfer interfaces: one describing heat transport in the solid matrix and the other in the fluid phase. These interfaces must then be coupled through a local thermal non-equilibrium (LTNE) multiphysics formulation. The

LTNE approach solves the two energy equations separately, allowing for distinct solid and fluid temperature fields, at the expense of doubling the computational cost.

In general, assessing the validity of the LTE assumption is not straightforward in specific situations. However, the *COMSOL Heat Transfer Module User's Guide* (COMSOL AB, 2015) provides criteria based on the dimensionless Sparrow number (Sp) and the Darcy number (Da) to assess the validity of this assumption. The Sparrow and Darcy numbers are defined by:

$$Sp = \frac{h_{sf} L^2}{k_{eff} r_h}, \qquad Da = \frac{\kappa}{d_p^2}$$

Where:

- h_{sf} (SI unit: W/(m²·K)) is the interstitial heat transfer coefficient between solid and fluid phases
- L (SI unit: m) is the plate layer thickness
- k_{eff} (SI unit: W/(m·K)) is the equivalent thermal conductivity of the porous medium
- r_h (SI unit: m) is the hydraulic radius
- κ (SI unit: m²) is the permeability
- d_p (SI unit: m) is the average particle diameter

For most practical applications, the LTE is satisfied when Sp > 100. However, for very fast transients, Sp should be as much as 500 or more (A. Amiri, 1998). Moreover, the LTE hypothesis becomes more justifiable for small values of Da. Numerical literature analyses show that values considered small are typically in the order of 10^{-7} (R. G. Carbonell, 1984).

The Darcy number can be readily computed using the particle diameter and permeability parameters of the model. Since the particles considered in this study have a characteristic length on the order of millimeters and are therefore relatively coarse, the resulting Darcy number is Da = 0.079, which is comparatively high. In addition, preliminary simulations showed that the Sparrow number is only slightly above the threshold value of 100. Based on these considerations, the LTNE formulation was therefore adopted for the present work.

The thermal contact between the reactor wall and the porous catalytic bed was modeled using a thin resistive layer, accounting for interfacial thermal resistance between the solid wall and the packed porous medium.

2.5.1 Governing Equations

Non-equilibrium heat transfer in porous media for binary systems consisting of a rigid porous matrix and fluid phase is governed by a set of two equations. These are the usual heat equations for solids and fluids, multiplied by the volume fractions θ_s and the porosity $(1 - \theta_s)$, respectively, and with an additional source term quantifying exchanged heat between both phases.

$$\theta_s \rho_s C_{p,s} \frac{\partial T_s}{\partial t} + \nabla \cdot \boldsymbol{q_s} = q_{sf}(T_f - T_s) + \theta_s \boldsymbol{Q_s}$$

$$\boldsymbol{q_s} = -\theta_s k_s \nabla T_s$$

$$(1 - \theta_s)\rho_f C_{p,f} \frac{\partial T_f}{\partial t} + \rho_f C_{p,f} \boldsymbol{u} \cdot \nabla T_f + \nabla \cdot \boldsymbol{q}_f = q_{sf}(T_s - T_f) + (1 - \theta_s)\boldsymbol{Q_f}$$

$$\boldsymbol{q_f} = -(1 - \theta_s) k_f \nabla T_f$$

In these expressions:

- θ_s (dimensionless) is the solid volume fraction.
- ρ_s (SI unit: kg/m³) and ρf are the solid and fluid densities.
- $C_{p,s}$ and $C_{p,f}$ (SI unit: J/ (kg·K)) are the solid and fluid heat capacities at constant pressure.
- $\mathbf{q_s}$ and $\mathbf{q_f}$ (SI unit: W/m2) are the solid and fluid conductive heat fluxes.

• k_s and k_f (SI unit: W/(m·K)) are the solid and fluid thermal conductivities.

• q_{sf} (SI unit: W/(m^3·K)) is the interstitial convective heat transfer coefficient.

• $\mathbf{Q_s}$ and $\mathbf{Q_f}$ (SI unit: W/m^3) are the solid and fluid heat sources.

• **u** (SI unit: m/s) is the fluid velocity vector. In the present work, the velocity field is computed from the *RFCs* interface and then coupled to be used accordingly.

In addition to the solid and fluid temperature fields, the LTNE formulation defines an energy-weighted average temperature T, obtained from the solid and fluid temperatures.

$$T = \frac{\theta_s \rho_s C_{p,s} T_s + (1-\theta_s)\rho_f \, C_{p,f} T_f}{\theta_s \rho_s C_{p,s} + \, (1-\theta_s)\rho_f \, C_{p,f}}$$

This variable does not represent an additional physical temperature, but rather an equivalent volumetric temperature whose definition preserves the total internal energy of the porous medium. It is mainly introduced for post-processing purposes and for compatibility with models based on the local thermal equilibrium assumption.

2.5.2 Heat Transfer Properties

Most of the properties required by the model are the same as those reported in Section 2.5.4. Only the additional properties are discussed below.

The heat capacities at constant pressure of the gas-phase species are obtained from the Shomate correlation, with coefficients taken from the NIST Chemistry WebBook (National Institute of Standards and Technology, Gaithersburg, MD, USA). The mixture heat capacity of the fluid phase is computed using a mass-weighted average according to:

$$c_{p,f} = \sum_{i=1}^{3} w_i c_{p,i}$$

Where:

- w_i (dimensionless) is the mass fraction
- $c_{p,i}$ (SI unit: J/(kg · K)) is the specific heat capacity at constant pressure of species i.

An analogous averaging procedure is adopted for the solid phase in order to estimate the effective heat capacity $c_{p,s}$ of the catalyst.

Particular attention must be paid to the evaluation of the effective thermal conductivity of the solid–fluid system, k_{eff}, which is related to the thermal conductivity of the solid phase, k_s, and of the fluid phase, k_f, and depends on the microstructural geometry of the porous medium.

Several simplified models for estimating the effective thermal conductivity of an isotropic porous medium are reported in the literature. In the limiting case where heat conduction in the solid and fluid phases occurs in parallel, the effective thermal conductivity can be approximated by the volume-weighted arithmetic mean of the phase conductivities:

$$\mathrm{k_{eff}} = \theta_\mathrm{s}\mathrm{k_s} + (1-\theta_\mathrm{s})\mathrm{k_f}$$

This expression represents an upper bound for the effective thermal conductivity. Conversely, if heat conduction occurs in series, with the heat flux sequentially crossing both phases, the effective thermal conductivity can be estimated using the harmonic mean:

$$\frac{1}{\mathrm{k_{eff}}} = \frac{\theta_\mathrm{s}}{\mathrm{k_s}} + \frac{1-\theta_\mathrm{s}}{\mathrm{k_f}}$$

This reciprocal average model provides a lower bound for the effective thermal conductivity of the porous medium.

2.5.3 Effective Thermal Conductivity of Ni/Al_2O_3 Pellets

The theoretical models presented above provide limiting or approximate estimates for the effective thermal conductivity of a porous catalytic pellet. However, their predictive accuracy strongly depends on the contrast between the solid and gas-phase conductivities, as well as on the actual morphology of the solid matrix. In order to apply these models to the Ni/Al_2O_3 catalytic material used in this work (60% w/w Ni), the effective conductivity of the solid matrix must first be estimated. Since heat conduction is governed by the spatial continuity of the phases rather than mass composition, the weighted average must be performed on volume fractions. Using the densities of Ni and Al_2O_3, the corresponding volume fractions v_{Ni} and $v_{Al_2O_3}$ are computed, and the solid-phase conductivity was evaluated using a linear rule of mixtures, which represents a first-order approximation for a composite solid phase:

$$k_s = v_{Ni}k_{Ni} + v_{Al_2O_3}k_{Al_2O_3} \approx 36.18\ \mathrm{W/mK}$$

This value, combined with the fluid conductivity $k_f \approx 0.08\ \mathrm{W/mK}$ and the solid volume fraction θ_p = 0.206, was then used to compute the effective conductivity using the models implemented in *COMSOL Multiphysics®*.

As described in the previous section, the harmonic and arithmetic models provide strict theoretical bounds corresponding respectively to fully sequential and fully parallel heat-transfer pathways

$$k_{eff}^{ser} = 0.101\ \mathrm{W/mK}, \qquad k_{eff}^{par} = 7.517\ \mathrm{W/mK}$$

These represent, respectively, the minimum and maximum admissible values for the effective thermal conductivity of the pellet under idealized microstructural assumptions.

Experimental measurements indicate instead an effective conductivity of $k_{\mathrm{eff}}^{\mathrm{exp}} = 0.358$ (Hughes, 1979), which lies within the theoretical bounds but is not satisfactorily predicted by any of the simple closed-form models.

Woodside and Messmer proposed that the thermal conductivity could be represented by the expression (W. Woodside, 1961):

$$k_{eff} = K_f \left(\frac{K_p}{K_f}\right)^{1-\theta_p} = 10.27\ \mathrm{W/mK}$$

Such a value significantly exceeds even the parallel limit, indicating an evident breakdown of the model assumptions. This is expected, as the formulation accounts for heat conduction through macropores only and neglects the micro- and mesoporous structure typical of catalyst pellets. As a result, when applied to bidisperse pore networks, the Woodside–Messmer equation systematically overpredicts k_{eff}.

When the porous medium is composed of solid spherical inclusions in a fluid phase (COMSOL AB, 2015), the effective thermal conductivity can be expressed as:

$$k_{eff} = kf\,\frac{2\,k_f + k_p - 2(k_f - k_s)q_p}{2k_f + k_p + (k_f - k_s)q_p} = 0.142\ \mathrm{W/mK}$$

Bruggeman symmetric equation for an isotropic two-phase medium (Bruggeman, 1935) is:

$$\theta_p \frac{k_p - k_{\mathrm{eff}}}{k_p + 2k_{\mathrm{eff}}} + (1 - \theta_p)\frac{k - k_{\mathrm{eff}}}{k + 2k_{\mathrm{eff}}} = 0.$$

Solving the equation numerically using a MATLAB script, with the k_p estimate above the result is:

$$k_{\mathrm{eff}}^{\mathrm{Bruggeman}} = 0.205\ \mathrm{W/mK}$$

Bruggeman produces an intermediate value between the harmonic and arithmetic bounds and moves the predicted k_{eff} closer to the experimental value. However, it still underpredicts the experimentally observed

effective conductivity. The discrepancy suggests that the pellet thermal transport is controlled by microstructural effects not captured by idealized two-phase EMA models.

Several physically plausible mechanisms may explain the higher experimental value. Pellet–pellet contact conduction within the packed bed may introduce high-conductivity parallel heat paths that increase apparent k_{eff}. Partial percolation or clustering of Ni at particle surfaces can create conductive networks significantly above the idealized "dispersed inclusion" assumption, effectively increasing the solid connectivity. Hierarchical porosity (micro-/mesopores) can modify gas-phase conduction and tortuosity in ways not reflected in simple binary mixing rules. Non-negligible radiative or interstitial contributions under experimental conditions may increase measured conductivity beyond purely conductive predictions.

More advanced formulations should therefore be considered. As discussed in Ref. 39, models that reproduce experimental values require knowledge of both micro- and macropore diameters, as well as the void fractions at each scale. The effective conductivity of the microporous particles must first be determined using the micropore void fraction, and then integrated with the macropore structure to estimate the pellet-scale conductivity. Harriott further distinguished three microstructural regimes: packed-bed, consolidated-particle, and porous-solid models, each of which requires detailed information on the interparticle contact area and pore-size distribution (Harriott, 1975).

Given these limitations, the experimentally measured value of $k_{\mathrm{eff}}^{\mathrm{exp}}$ is the most reliable estimate for quantitative reactor-scale thermal modelling. In the absence of experimental measurements and when the detailed microstructural information required by more advanced models is not available, this analysis confirms that the Bruggeman effective medium formulation represents a robust and physically consistent choice for estimating the effective thermal conductivity of porous catalyst pellets.

2.5.4 Reaction Heat Source Term

The volumetric heat-generation term required by COMSOL must be expressed in units of $\mathrm{W{\cdot}m^{-3}}$. To obtain this, the reaction enthalpy is coupled with the local reaction rate and the bulk density of the pellet. In this work the source term is implemented as

$$Q = -\,\Delta H_{\mathrm{rxn}}(T)\;\rho_{\mathrm{bulk}}\,r$$

where r is the intrinsic reaction rate per unit mass of catalyst (SI unit: $\mathrm{mol\ kg^{-1}s^{-1}}$). The negative sign is consistent with the convention that endothermic reactions correspond to negative volumetric heat sources.

Because ammonia decomposition exhibits a strongly temperature-dependent reaction enthalpy, the expression for $\Delta H_{\mathrm{rxn}}(T)$ must account for the standard enthalpy change and for the sensible enthalpy contributions of reactants and products. The formulation used is

$$\Delta H_{\mathrm{rxn}}(T) = \Delta H_{\mathrm{rxn}}(T_{\mathrm{ref}}) + \int_{T_{\mathrm{ref}}}^{T} \left[\sum_{\mathrm{Prod}} \nu_i c_{p,i}(T') - \sum_{\mathrm{React}} \nu_j c_{p,j}(T') \right] dT'$$

Here $\Delta H_{\mathrm{rxn}}(T_{\mathrm{ref}} = 298\ K) = 46'110\ \mathrm{J/mol_{NH3}}$ is the standard enthalpy change at the reference state, while the temperature-dependent heat capacity contributions correct this value to the local temperature.

While this formulation allows the heat-generation term to respond locally to temperature variations within the porous catalytic domain, its implementation introduces a strong nonlinear coupling between reaction kinetics and heat transfer. Numerical tests showed that evaluating $\Delta H_{rxn}(T)$ locally at each iteration significantly deteriorates the convergence behavior of the steady-state solver under the operating conditions considered.

For this reason, a simplified formulation was adopted in which the reaction enthalpy is evaluated at the wall temperature and treated as constant:

$$\Delta H_{rxn}(T) \approx \Delta H_{rxn}(T_{wall})$$

This approximation reduces the numerical stiffness of the coupled energy species momentum problem and allows stable convergence of the steady-state simulations under the operating conditions considered.

2.6 Extension of the Model to Monolithic Catalyst Geometries

To complement the packed-bed reactor model, the numerical framework was extended to simulate additively manufactured (3D-printed) monolithic nickel catalysts. The purpose of this extension is a qualitative, geometry-driven comparison among different channel architectures under identical operating conditions and kinetic inputs.

In contrast to the porous pellet bed (Ni/Al_2O_3), the monoliths consist of a continuous solid nickel structure and therefore exhibit a substantially higher thermal conductivity. A fixed thermal conductivity of 65 W/m·K was adopted for nickel, in agreement with the average value reported over the operational range of interest (R. W. Powell, 1965). Moreover, in the monolith, thermal energy is first conducted through the continuous solid framework and subsequently transferred to the fluid phase, which constitutes a significantly more efficient path for heat transfer compared to the porous pellets. As a consequence, the monolithic configurations are expected to mitigate reaction-induced temperature depressions.

2.6.1 Geometry and Computational Domain

The monolith is characterized as follows: it has a cylindrical shape and replaces the porous catalytic bed. Its diameter coincides with the inner diameter of the reactor tube (7 mm), while its axial length is 10 mm. The cylindrical body contains an array of straight channels with either square or hexagonal cross-sections. Channel size and wall thickness vary among the investigated designs in order to assess the sensitivity of the temperature and conversion fields to the monolith architecture.

Four different monolithic channel architectures were analyzed (Figures 13–16). The geometries differ primarily in terms of channel density and wall thickness distribution, parameters that directly affect solid-phase heat conduction and the hydrodynamic behavior of the gas flow. Geometry 1 (Agueniou) is based on the monolithic structure proposed by Agueniou et al. and is used here as a reference configuration. The structure corresponds to a relatively low channel density of approximately 230 cells per square inch (CPSI) and features significantly thicker walls compared to the other designs (Fazia Agueniou, 2022). Geometry 2 (Hexagon_CPSI400) adopts a conventional honeycomb layout with hexagonal channels and a cell density of approximately 400 CPSI; the walls have uniform thickness. Geometry 3 (Hexagon_CPSI400_Massiv) maintains the same nominal channel density (400 CPSI) but introduces a radially varying wall thickness, with struts progressively thickening toward the outer region of the monolith. This modification slightly alters the channel shape and is intended to enhance radial heat conduction within the metallic structure. Geometry 4 (Hexagon_CPSI600) is characterized by a higher channel density of 600 CPSI, resulting in a larger number of smaller hexagonal channels.

In all configurations, the monolithic structure is enclosed by an external annular wall with a thickness of 0.3 mm, ensuring mechanical integrity and contact with the reactor wall. Since the channel cross-sections are not axisymmetric, the simulations are performed in three dimensions. To reduce computational cost, only one quarter of the reactor cross-section is modeled, and symmetry boundary conditions are imposed on the two cut planes.

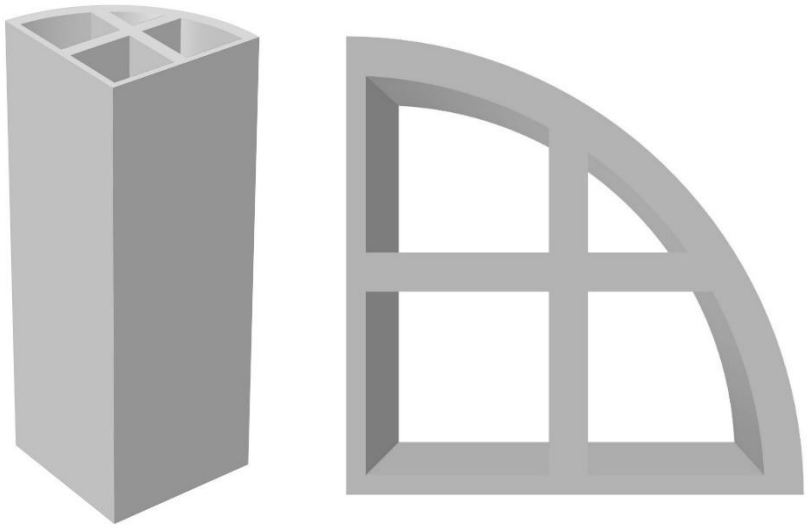

Figure 13, Monolith geometry Agueniou

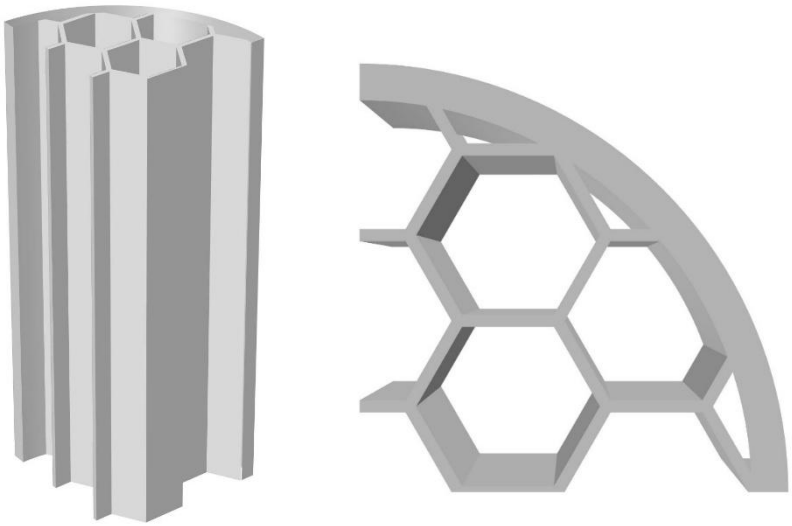

Figure 14, Monolith geometry Hexagon_CPSI400

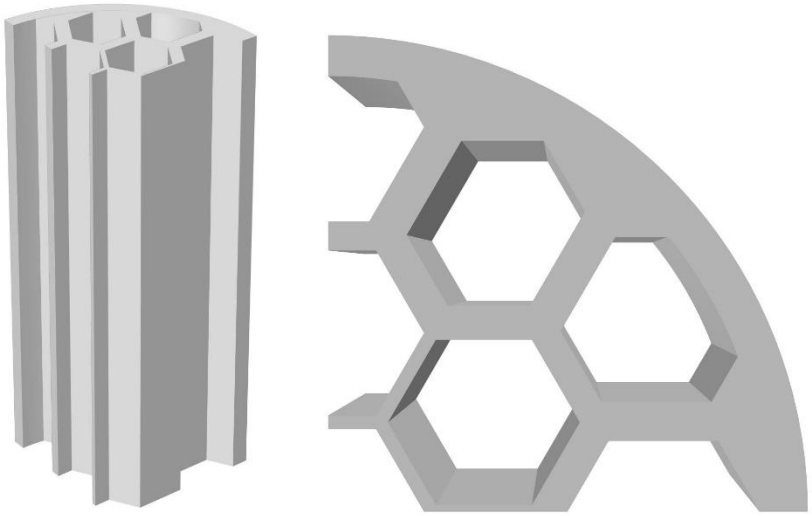

Figure 15, Monolith geometry Hexagon_CPSI400_Massiv

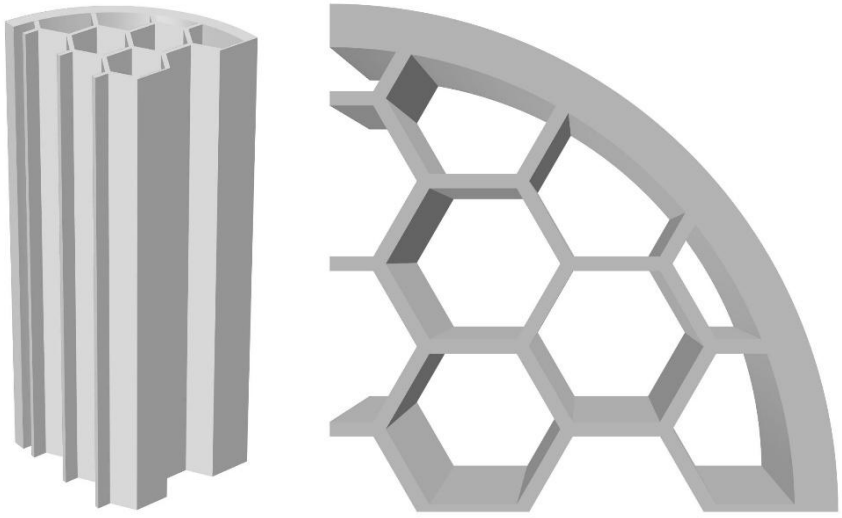

Figure 16, Monolith geometry Hexagon_CPSI600

2.6.2 Physical Model and Governing Assumptions

The gas-phase description (mixture properties, multicomponent diffusion, and heat transfer in the free flow) is retained from the packed-bed model. Species transport is still described using a concentrated-mixture formulation with Maxwell–Stefan diffusion, and gas-phase properties are computed consistently as a function of temperature and composition. The reactor wall heating configuration and the conjugate heat-transfer treatment are preserved.

All porous-medium-related parameters and flow-resistance closures were eliminated, and the computational domain was explicitly partitioned into a gas-flow region, comprising both the open monolith channels and the upstream and downstream free-flow sections, and a solid nickel region corresponding to the monolith structure.

Momentum transport is solved only in the gas channels, while heat conduction is solved in the solid domain. The two domains are thermally coupled through continuity of heat flux at the solid–fluid interface. An additional thin interfacial thermal resistance layer is included to represent unresolved thermal contact resistance at this interface.

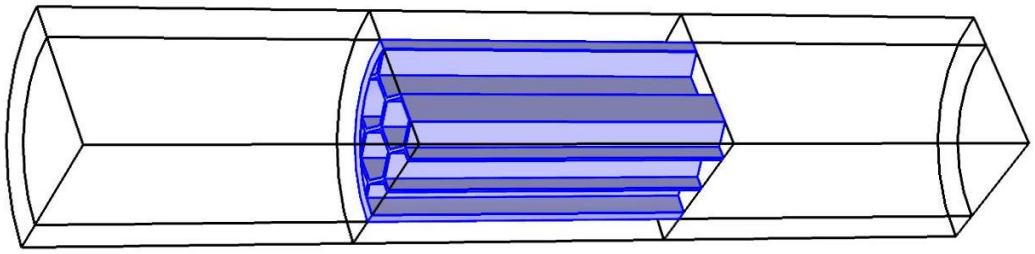

Figure 17, Domain of the 3D model. In blue the monolithic catalyst

Ammonia decomposition in the monolith simulations is described using the same Temkin–Pyzhev kinetic expression adopted for the packed-bed model (Section 2.4.3), implemented as a volumetric source term. The same formulation is retained for all monolith geometries to maintain identical kinetic conditions across configurations and to avoid introducing additional structure-dependent parameters. It is emphasized that ammonia decomposition on nickel is intrinsically a wall-mediated process. Consequently, the present formulation does not aim to predict the absolute performance of a monolithic catalytic reactor.

3. Results and Discussion

The modeling framework described in the previous sections provides a fully coupled description of momentum, species, and heat transport in a catalytic fixed-bed reactor. The parametric study covers a representative operating window defined by wall temperature (300–700 °C) and inlet volumetric flow rate (20–240 mL/min) at atmospheric pressure. This chapter first checks numerical/physical consistency of the coupled RFCS–LTNE model, then uses it to quantify the impact of k_{eff}, bed length, and kinetic parameters within the validated window. The model is subsequently applied to a comparative analysis of alternative reactor configurations by evaluating different 3D-printed nickel monolithic catalyst geometries.

3.1 Model Verification and Physical Consistency Checks

Before conducting parametric analyses, the numerical model is assessed for internal consistency and physical plausibility. This section verifies that the coupled momentum, species, and energy transport formulation generates solutions that are consistent with fundamental conservation laws and are qualitatively correct. This analysis is intended as a verification of the model implementation rather than as a quantitative validation against experimental data.

The stationary problem was solved using the default COMSOL solver configuration. A fully coupled Newton method with the PARDISO linear solver was employed, and convergence was assessed using the default relative

tolerance of 10^{-4}. The following operating conditions and kinetic parameters were adopted as reference values for model verification. All figures presented subsequently correspond to simulations carried out under these conditions.

T_{wall}	500 °C	Wall temperature
T_{in}	500 °C	Inlet temperature
p_{in}	1 atm	Inlet pressure
Q_{in}	100 mL/min	Inlet flowrate
k_{eff}	0.358 W/(m·K)	Effective thermal conductivity
K_0	$2.25 \cdot 10^5$ (mol·Pa$^{0.5}$)/(kg·s)	Pre-exponential factor
alpha	0.5	Temkin–Pyzhev empirical parameter
Ea	$1.0 \cdot 10^5$ J/mol	Activation energy

Table 1, Consistency simulation parameters

3.1.1 Mesh Independence Analysis

A mesh-independence study was performed to evaluate the sensitivity of the numerical solution to spatial discretization. The mesh was progressively refined in the catalytic bed, free-flow regions, and near-wall zones, while all physical and kinetic parameters were kept constant.

Two representative quantities were monitored: the minimum temperature within the catalytic bed and the ammonia mole fraction at the reactor outlet. These variables are particularly sensitive to coupled heat and mass transfer effects and were therefore selected as indicators of numerical convergence. The corresponding trends are shown in Figure 18.

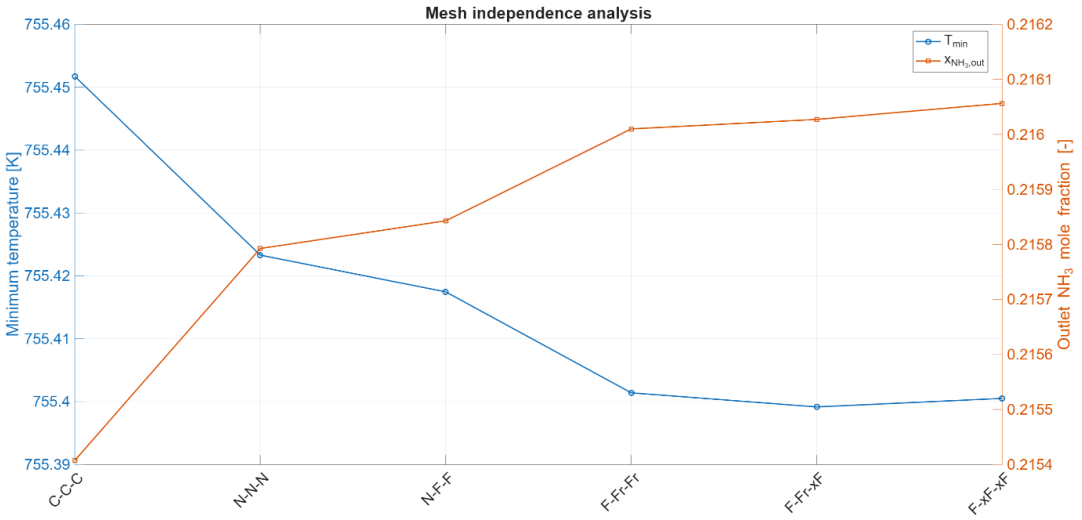

Figure 18, Minimum bed temperature and outlet ammonia mole fraction as a function of mesh refinement.

Quantitative results are reported in Table 2. The solution obtained with the finest mesh (F–xF–xF) was taken as numerical reference, and relative deviations were evaluated accordingly. A relative error threshold of 0.02% was adopted for both monitored quantities.

Mesh refinement	T min [K]	Rel. error on T [%]	xNH_3,out [-]	Rel. error on xNH_3,out [%]
C-C-C	755.45173	0.00678	0.21540744	0.300
N-N-N	755.42330	0.00301	0.21579264	0.122
N-F-F	755.41746	0.00224	0.21584297	0.099
F-Fr-Fr	755.40140	0.00011	0.21600995	0.021
F-Fr-xF	755.39916	0.00018	0.21602726	0.013
F-xF-xF	755.40051	0.0000	0.21605639	0.000

Table 2, Relative errors of T_{min} and xNH_3,out for increasing mesh refinement.

The results indicate that variations fall below the prescribed tolerance at the F–Fr–xF level. No appreciable changes are observed upon further refinement. On this basis, this mesh was selected for all subsequent simulations, as it represents the coarsest grid satisfying the prescribed accuracy threshold.

It is worth noting that the absolute variations in both monitored quantities remain small across all refinement levels, with temperature variations below 0.05 K and outlet mole fraction variations below 10^{-3}. This confirms that the numerical solution can be considered effectively mesh-independent throughout the investigated discretization range.

3.1.2 Mass, Species, and Energy Consistency

Figure 17 shows the steady-state spatial distributions of ammonia, hydrogen, and nitrogen mole fractions within the reactor domain. Ammonia is consumed within the catalytic bed, while nitrogen and hydrogen are generated and transported downstream. All species mole fractions remain bounded between zero and one throughout the computational domain, and no spurious oscillations or negative concentrations were observed. The solution fields are spatially smooth, indicating stable coupling between reaction kinetics and multicomponent transport.

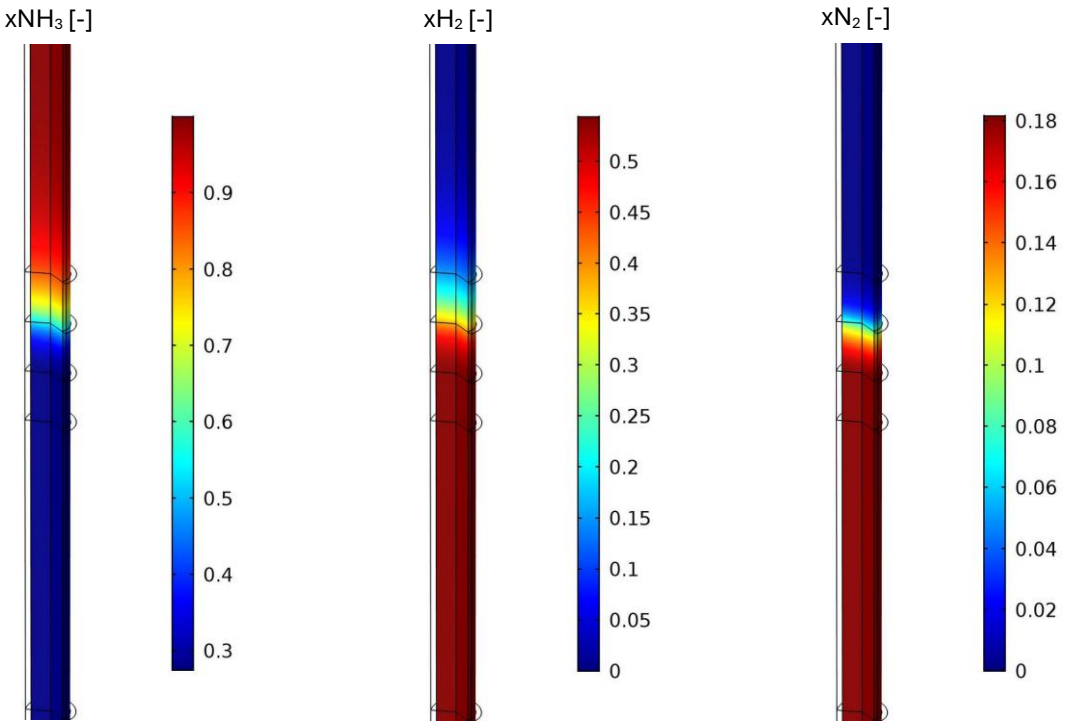

Figure 19, Spatial distributions of components mole fractions within the reactor domain

To provide a clearer quantitative interpretation, axial profiles of cross-section–averaged mole fractions are reported in Figure 20.

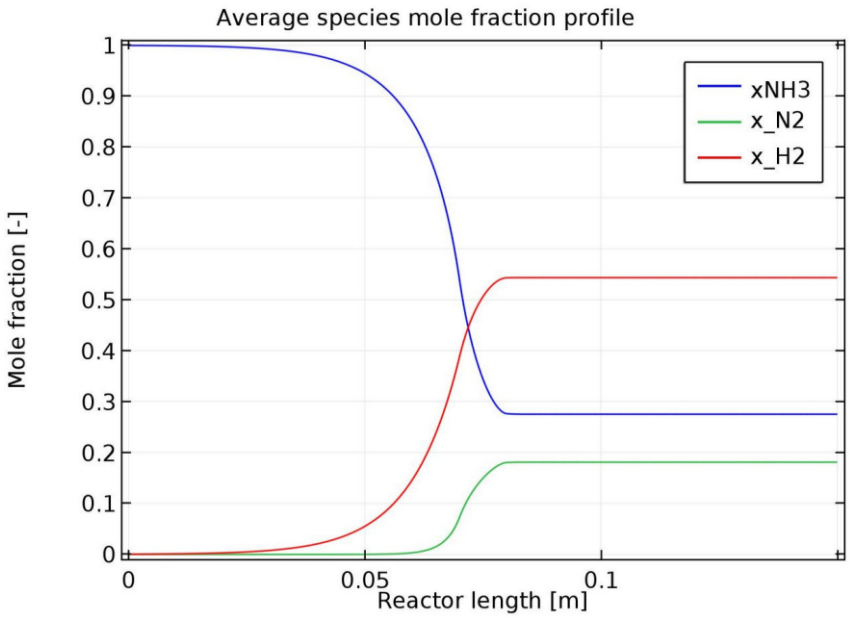

Figure 20, Axial profiles of cross-section averaged species mole fractions

The global molar balance was verified by checking the molar flow rates at the inlet and outlet. The computed outlet ratio of 3.00009324 is in agreement with the theoretical stoichiometric value, confirming conservation of mass within numerical tolerance.

Hydrogen and nitrogen are observed upstream of the catalytic bed, extending approximately 50 mm prior to the entrance. Although the reaction occurs almost exclusively within the porous region, this behavior is physically consistent and results from the diffusion of reaction products upstream against the bulk convective flow. Due to its higher diffusivity in ammonia, hydrogen penetrates further upstream than nitrogen.

The velocity field is shown in Figure 19. The no-slip condition is correctly enforced at the reactor wall. Within the catalytic bed, the velocity profile reflects the adopted Brinkman–Darcy formulation for the porous medium.

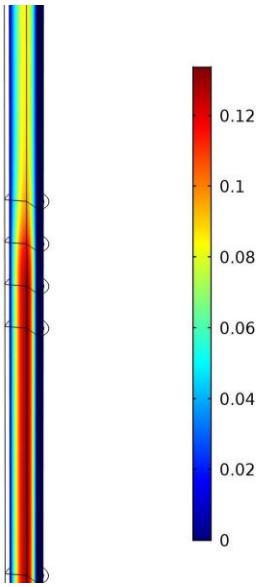

Figure 21, Velocity profile within the reactor [m/s]

A gradual increase in axial velocity is observed along the length of the reactor, consistent with the molar expansion associated with ammonia decomposition. The reaction increases the total molar flow rate, resulting in a local increase in volumetric flow.

A significant temperature decrease (around 20 °C) occurs within the catalytic bed, reflecting the strongly endothermic nature of ammonia decomposition. The temperature distribution is shown in Figure 20.

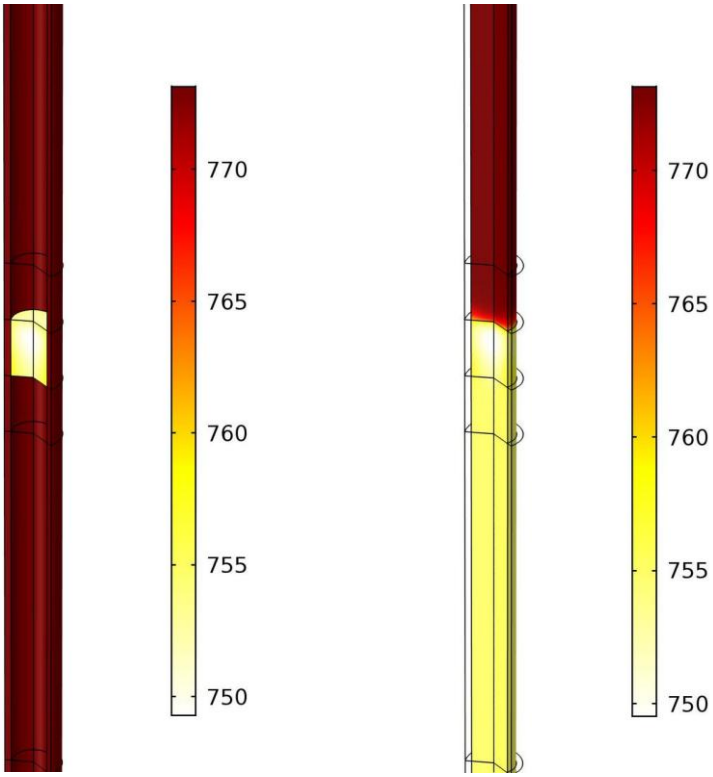

Figure 22, Axial temperature profiles of the solid phase (left) and the fluid phase (right) within the reactor [K]

The minimum bed temperature is 749.3 K, and a pronounced radial temperature drop is observed at the interface between the reactor wall and the porous bed. This temperature discontinuity reflects the finite thermal contact resistance between the metallic wall and the catalytic matrix, which is modeled through a thin resistive thermal layer at the interface.

Radial temperature profiles of the solid and fluid phases were extracted at three axial positions: the bed entrance, the mid-bed, and the outlet. At the bed entrance, a noteworthy temperature difference between the fluid and solid phases is observed. At the reactor centerline (r = 0), the fluid temperature is approximately 7 K higher than the solid temperature. This difference decreases progressively along the axial direction. At the mid-bed and outlet positions, the solid and fluid temperatures nearly coincide across most of the radius with no significant deviations except near the wall.

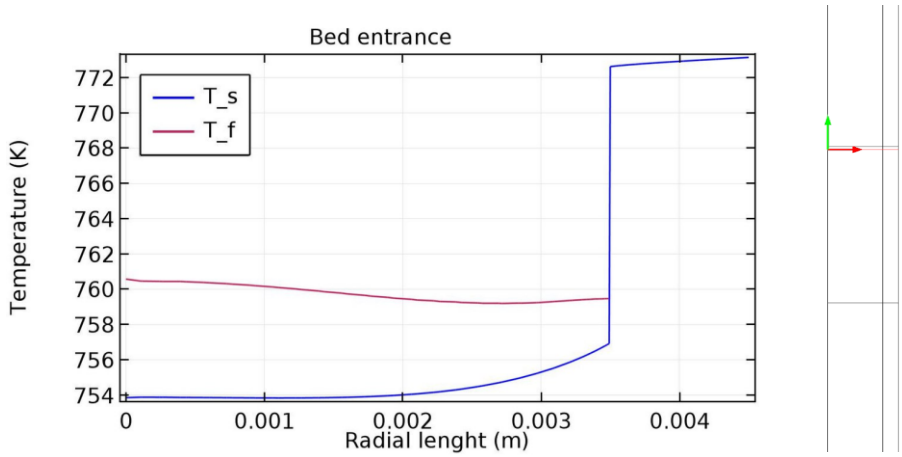

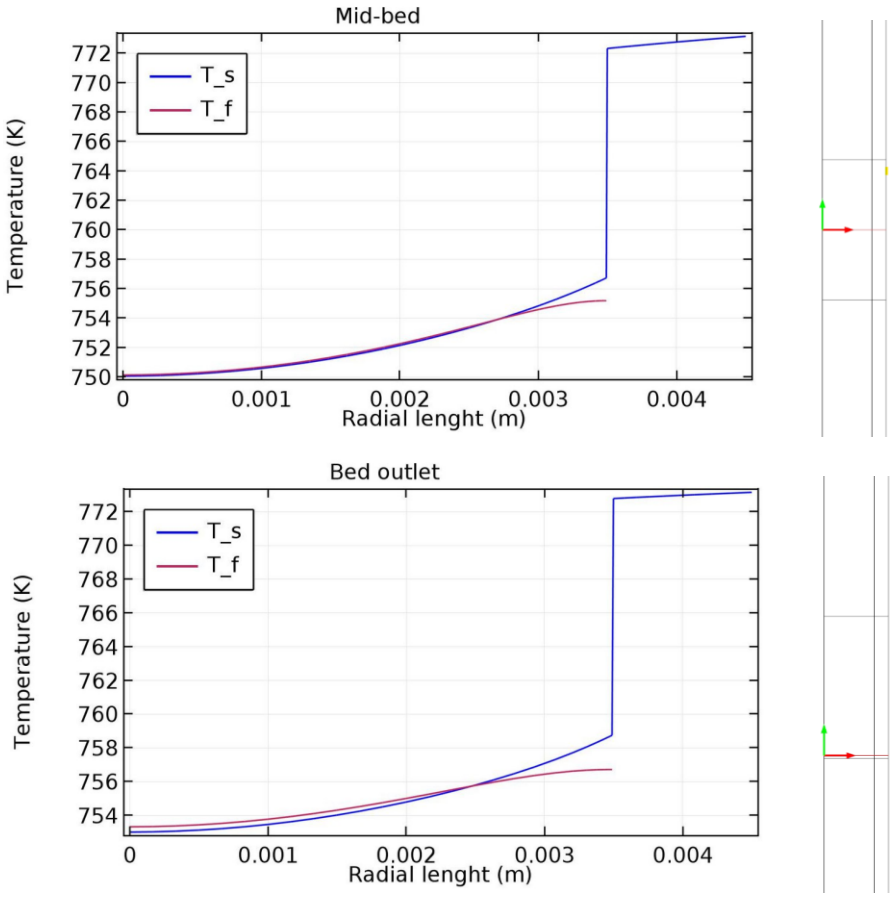

Figure 23, Radial temperature profiles along the bed

These results indicate that NLTE effects are most significant near the bed entrance, while the system approaches thermal equilibrium conditions downstream. For the present operating regime, an LTE approximation would likely provide acceptable accuracy. Nevertheless, the LTNE formulation ensures that the model remains applicable under conditions characterized by stronger thermal gradients.

3.1.3 Model Applicability Limits

The applicability limits of the numerical model were investigated to identify the operating conditions under which the coupled momentum, heat, and multicomponent mass transport formulation provides physically consistent and numerically stable solutions.

The inlet composition is imposed through a Dirichlet boundary condition, with H_2 and N_2 mole fractions fixed equal to zero. While this boundary condition correctly reproduces the experimental feeding configuration, it may become incompatible under regimes characterized by strong upstream diffusive transport. To quantify the onset of this incompatibility, a parametric sweep was performed on the inlet volumetric flow rate while maintaining the most diffusion-favouring thermal conditions investigated in this work. At fixed pressure, gas-phase molecular diffusivities increase with temperature, thereby enhancing upstream diffusive transport. For this reason, the inlet and wall temperatures were set to their maximum investigated value of 700 °C. Under these conditions, varying the inlet flow rate directly modifies the relative importance of convective transport, allowing identification of the minimum flow rate required to maintain physically consistent solutions.

The physical validity of each simulation was assessed using a stoichiometric consistency criterion based on outlet molar flow rates. The outlet molar production rates must satisfy the stoichiometric constraint. The relative deviation from the theoretical stoichiometric ratio was then defined as:

$$\varepsilon_{stoich} = \left| \frac{\dot{n}_{H_2}}{\dot{n}_{N_2}} - 3 \right|$$

A simulation was considered physically consistent when the deviation satisfied the criterion $\varepsilon_{stoich} < 2 \cdot 10^{-4}$.

The simulations reveal that the stoichiometric deviation strongly depends on the inlet volumetric flow rate. At low flow rates, the outlet molar ratio significantly deviates from the theoretical value. For instance, at a flow rate of 20 mL/min, the deviation is 0.198, corresponding to an outlet molar flow ratio of H_2/N_2 = 2.80, which is physically inconsistent. At a flow rate of 0.04 L/min, the deviation decreases to 0.0177, but it still far exceeds the admissibility threshold. A rapid improvement is observed as the flow rate increases, with the deviation falling below the prescribed criterion at approximately $\mathrm{Q_{in}} \approx 0.08\ \mathrm{L/min}$. Further increases in the flow rate produce only marginal improvements, with the deviations stabilizing around $O(10^{-5})$.

To further investigate the mechanism responsible for the observed deviations, the relative contributions of convective and diffusive species transport were examined in the inlet region by evaluating the corresponding axial flux components at representative cross-sections upstream of the catalytic bed. The analysis indicates that under low-flow conditions the upstream region is strongly affected by diffusive transport of reaction products generated within the catalytic bed. In particular, hydrogen produced in the porous domain can diffuse upstream toward the reactor inlet.

Because the inlet boundary condition imposes zero mole fractions for hydrogen and nitrogen, the numerical solution must simultaneously satisfy the diffusive flux originating from the catalytic bed and the fixed composition imposed at the boundary. Under sufficiently low inlet flow rates, these constraints become incompatible and lead to steep concentration gradients in the inlet region, ultimately resulting in inconsistencies in the outlet species balance.

Additional verification was performed to further assess the role of upstream diffusion. A set of auxiliary simulations was conducted in which the binary molecular diffusivities of hydrogen and nitrogen were uniformly reduced by one order of magnitude, with all other operating conditions held constant. Under these modified transport conditions, physically consistent solutions were recovered even at inlet flow rates that previously produced significant stoichiometric deviations.

This behavior confirms that the loss of physical consistency is directly associated with strong upstream diffusion from the catalytic bed toward the inlet boundary. Reducing the binary diffusivities suppresses axial back-diffusion and restores compatibility between the transport equations and the imposed Dirichlet inlet composition.

Based on the above results, physically consistent solutions are obtained only for inlet flow rates above approximately 80 mL/min under the most diffusion-favouring thermal conditions investigated in this work. Since molecular diffusivities increase with temperature at fixed pressure, this threshold represents a conservative lower bound for the inlet flow rate within the considered operating window. Within this validated range, the model provides stable and physically consistent predictions and can therefore be used for the parametric analyses presented in the following sections.

3.2 Parametric Analysis of Reactor Performance

To identify the key parameters governing reactor performance and thermal behaviour, a systematic parametric analysis was carried out within the validated operating window defined in the previous section. The analysis focuses on parameters expected to influence both reaction kinetics and heat-transport mechanisms, including effective bed thermal conductivity, catalytic bed length, and intrinsic kinetic constants. For each parameter, steady-state simulations were performed over the investigated ranges of wall temperature and inlet flow rate. Reactor performance was evaluated in terms of outlet ammonia conversion, temperature distribution, and local thermal non-equilibrium indicators, allowing assessment of both global reactor efficiency and internal transport limitations.

3.2.1 Effect of Effective Thermal Conductivity

The effective bed conductivity was varied from 0.101 to 7.517 W/(m K), which corresponds to the theoretical bounds of the series and parallel configurations of porous catalytic packing. This range includes intermediate values obtained from analytical correlations, such as the Bruggeman formulation, and the experimentally

determined effective conductivity of 0.358 W/(m K). Thus, it covers realistic values representative of packed metallic catalyst structures.

Conversion behaviour

Figure 22 presents the outlet ammonia conversion as a function of effective bed conductivity for all investigated temperatures and flow rates. Across the entire operating window, conversion increases monotonically with increasing k_{eff}, confirming that enhanced conductive heat transport progressively alleviates reaction-induced thermal limitations within the porous bed. At a fixed conductivity, an increase in the inlet flow rate systematically reduces conversion. This reflects the combined effects of reduced residence time and increased thermal demand associated with the strongly endothermic reaction. Similar trends were observed across all investigated flow rates.

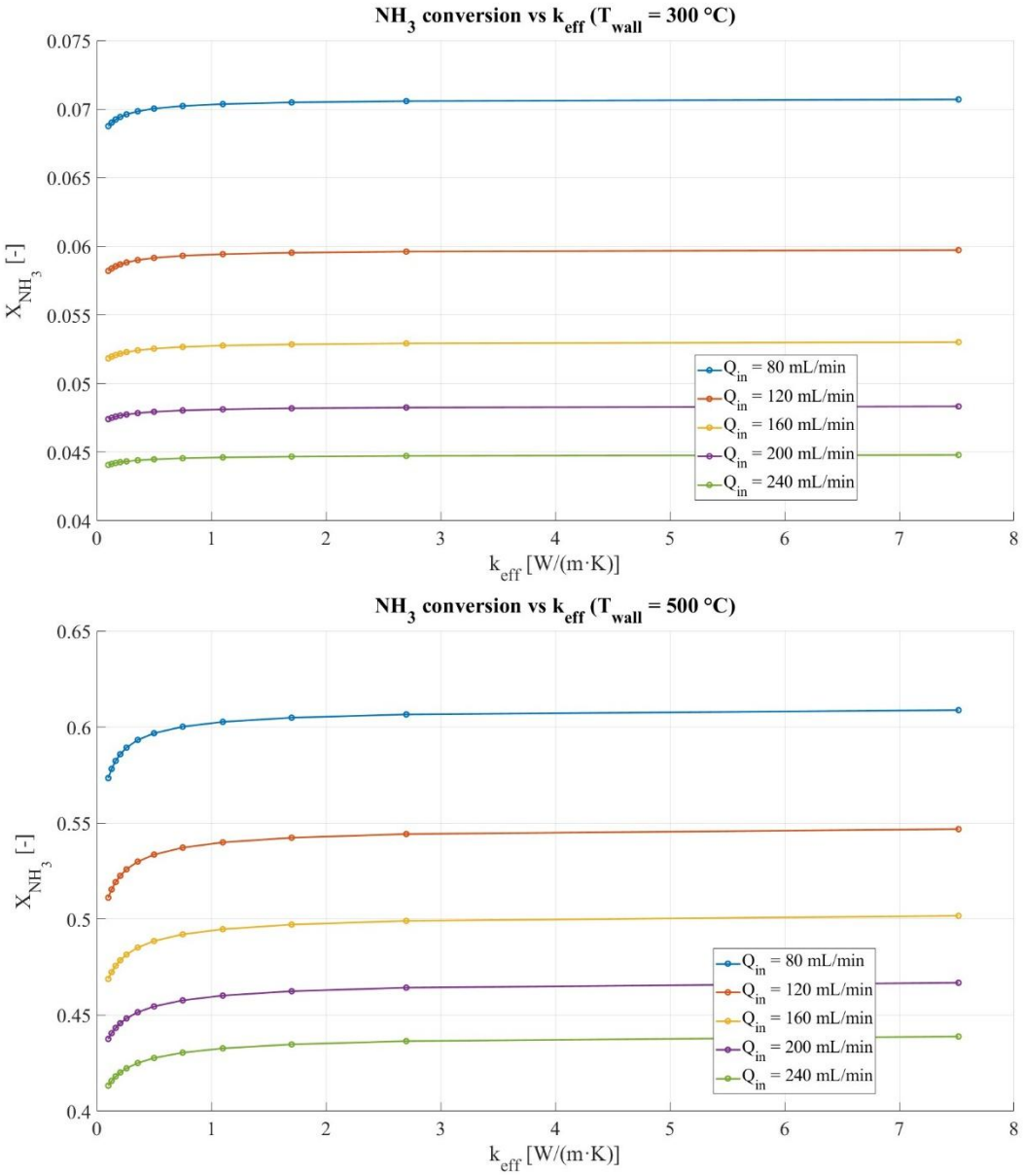

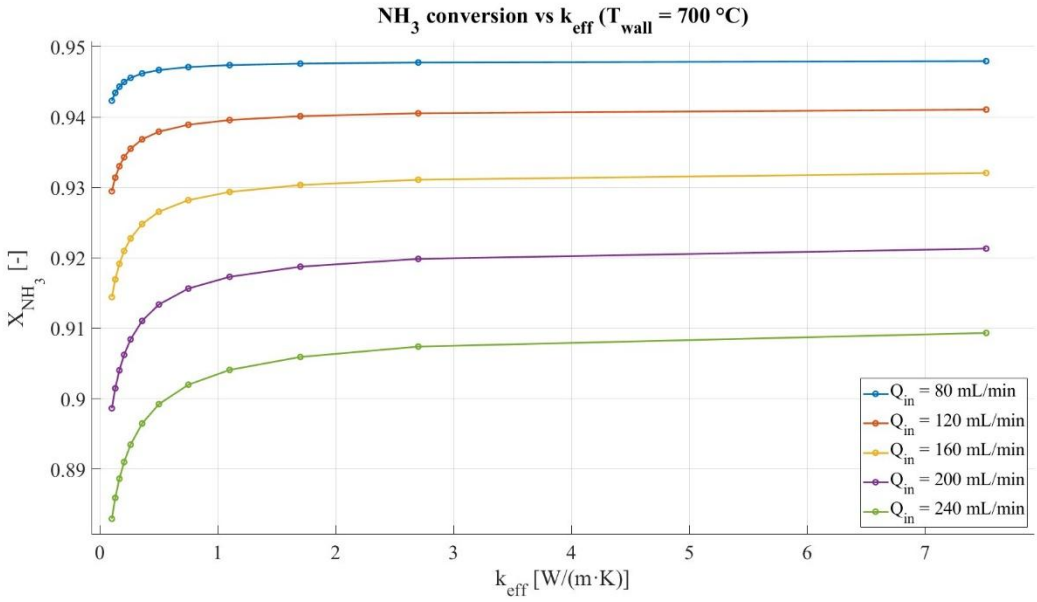

Figure 24, X_{NH_3} vs k_{eff} at different temperatures

To quantify the impact of conductivity, the absolute conversion gain was defined as follows:

$$\Delta X_{\%} = [X(k_{eff,max}) - X(k_{eff,min})] \cdot 100$$

T_{wall} (°C)	$\Delta X_{\%}$ (80 mL/min)	$\Delta X_{\%}$ (160 mL/min)	$\Delta X_{\%}$ (240 mL/min)
300	0.195	0.118	0.073
400	1.568	1.101	0.741
500	3.538	3.287	02.556
600	2.668	4.023	3.991
700	0.562	1.763	2.639

The conversion gain associated with increasing effective thermal conductivity remains small across the entire investigated range. Even under the most favourable conditions, the maximum improvement does not exceed a few percentage points. Therefore, intrabed heat transport does not appear to be the primary performance-limiting mechanism under the investigated conditions.

The sensitivity to conductivity exhibits a clear temperature dependence. At low temperature (300 °C), conversion is predominantly controlled by intrinsic kinetics, and the effect of enhanced heat transport is negligible. The relative impact increases at intermediate temperatures (400–600 °C), where stronger reaction-induced cooling generates larger internal temperature gradients and moderately amplifies the benefit of improved thermal redistribution. At 700 °C, the gain decreases again at low flow rates as conversion approaches its kinetic ceiling, while remaining observable at higher throughputs where thermal gradients persist.

To further quantify the relative importance of effective conductivity, a normalized sensitivity indicator was introduced. This indicator is defined as follows:

$$S_k = \frac{\Delta X}{X_{max}} \cdot 100 = \frac{X(k_{eff,max}) - X(k_{eff,min})}{X(k_{eff,max})} \cdot 100$$

T_{wall} (°C)	S_k (80 mL/min)	S_k (160 mL/min)	S_k (240 mL/min)
300	2.76	2.23	1.62
400	5.60	5.11	4.04
500	5.81	6.55	5.82
600	3.09	5.11	5.50
700	0.59	1.89	2.90

The normalized sensitivity indicator confirms the limited role of effective conductivity. Across all operating conditions, S_k remains below approximately 6.5%, demonstrating that variations in thermal conductivity produce only marginal changes in reactor performance.

Sensitivity is highest at intermediate temperatures (400–500 °C), where thermal transport and reaction kinetics exert comparable influence. At lower temperatures, kinetics dominate, and S_k remains below about 3%. At high temperature (700 °C), sensitivity decreases further at low flow rates due to conversion saturation, while remaining modestly observable at high throughput where stronger thermal gradients persist.

Cold-Spot Formation and Mitigation

The conversion behavior discussed in the previous section is closely associated with the temperature distribution within the porous catalytic bed. To quantify the thermal mechanisms underlying conductivity-driven performance variations, the influence of the bed's effective thermal conductivity was analyzed using the minimum solid temperature within the porous domain, $T_{s,min}$, and the corresponding temperature depression relative to the imposed wall temperature.

Figure 23 shows $T_{s,min}$ as a function of k_{eff} for the investigated operating conditions. Over the entire temperature and flow rate spectrum, $T_{s,\min}$ consistently increases as k_{eff} grows, highlighting the role of enhanced intra-particle conductive heat transfer in balancing thermal gradients inside the catalytic bed. This effect is more pronounced at high temperatures, where the reaction cooling effect is stronger.

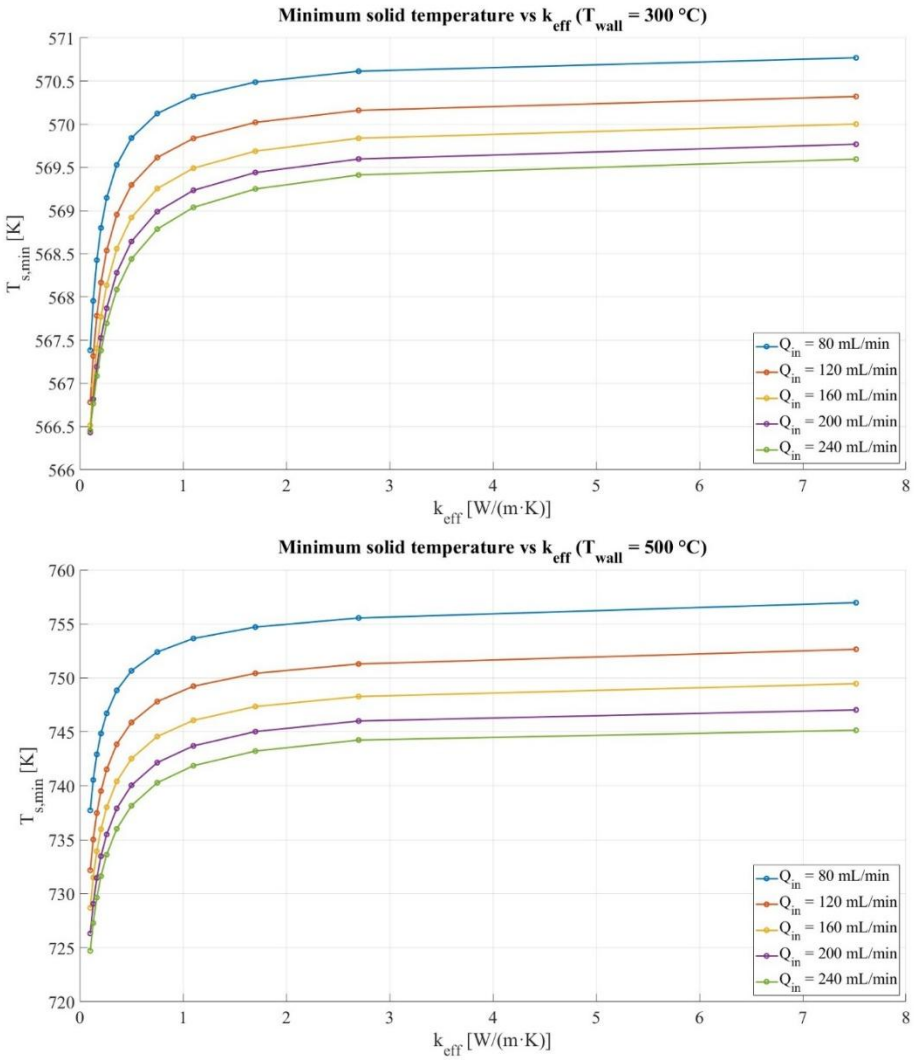

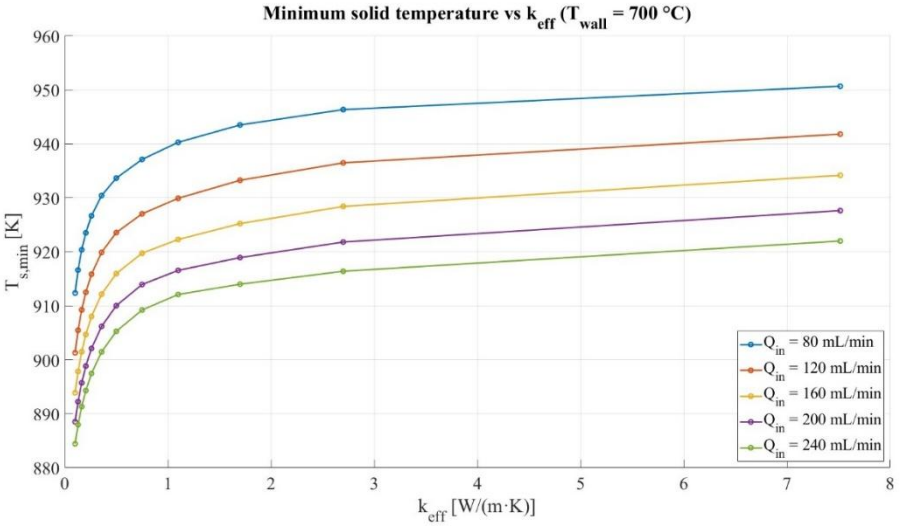

Figure 25, Ts,min vs keff at different temperatures

The qualitative behavior is consistent across the entire operating window. For a given wall temperature, increasing the inlet flow rate systematically lowers $T_{s,\min}$ due to the combined effects of shorter residence time and higher local heat consumption by reaction. Conversely, increasing effective conductivity partially compensates for this temperature depression by improving intrabed heat transport. While the absolute temperature drop increases with wall temperature as reaction heat demand becomes more pronounced, the dependence on conductivity remains similar across all cases.

To enable direct comparison across different thermal regimes, cold-spot severity was further quantified using the temperature drop, defined as

$$\Theta_{\text{cold}} = \mathrm{T}_{\text{wall}} - \mathrm{T}_{\text{s,min}}.$$

Figure 24 shows the variation of Θ_{cold} with effective thermal conductivity for representative low, intermediate, and high wall temperatures.

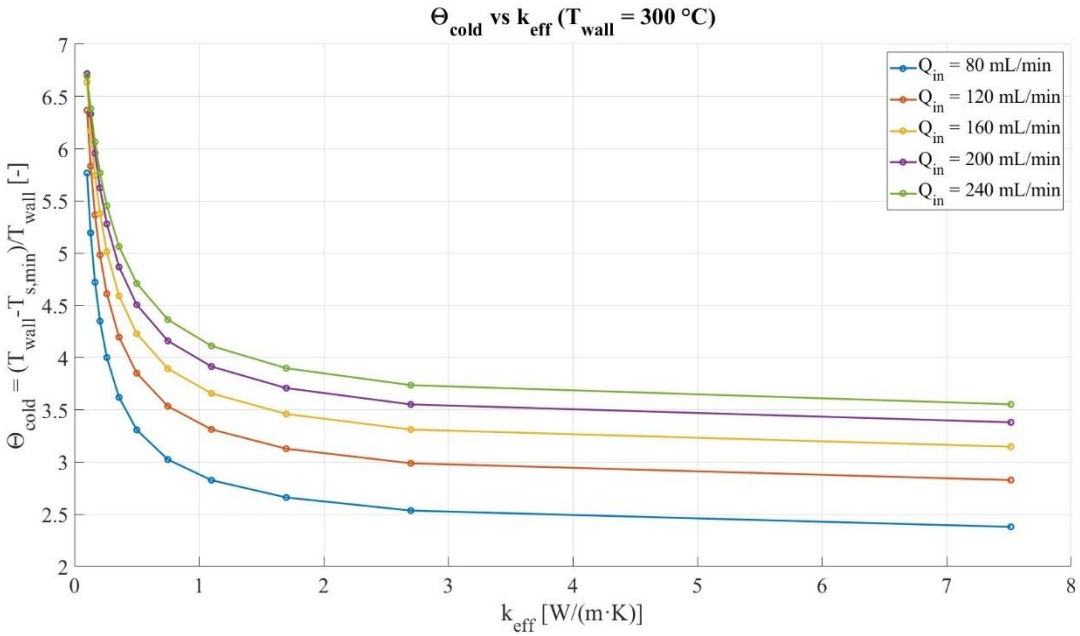

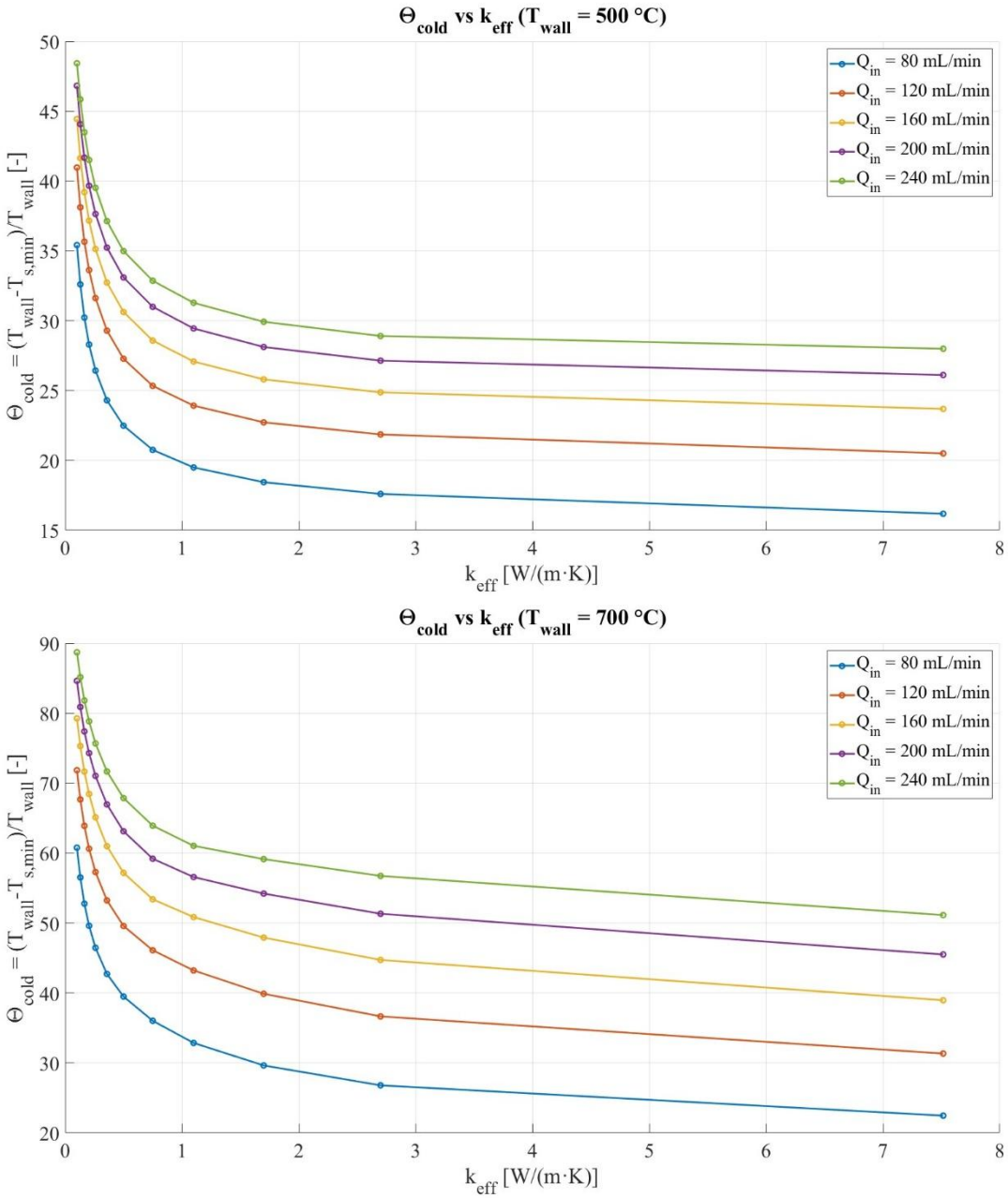

Figure 26, Theta vs k_{eff}

Across all flow rates and temperatures, Θ_{cold} decreases monotonically with increasing k_{eff}, confirming that improved conductive heat transport systematically mitigates reaction-induced cooling within the catalytic bed.

The normalized representation highlights that the mitigation benefit associated with higher conductivity becomes more significant at elevated wall temperatures. As thermal demand increases, enhanced intrabed heat redistribution more effectively limits the relative temperature depression, although the qualitative dependence on conductivity remains similar across the entire operating window.

The dependence of cold-spot severity on wall temperature is further illustrated in Figure 27 for a representative inlet flow rate.

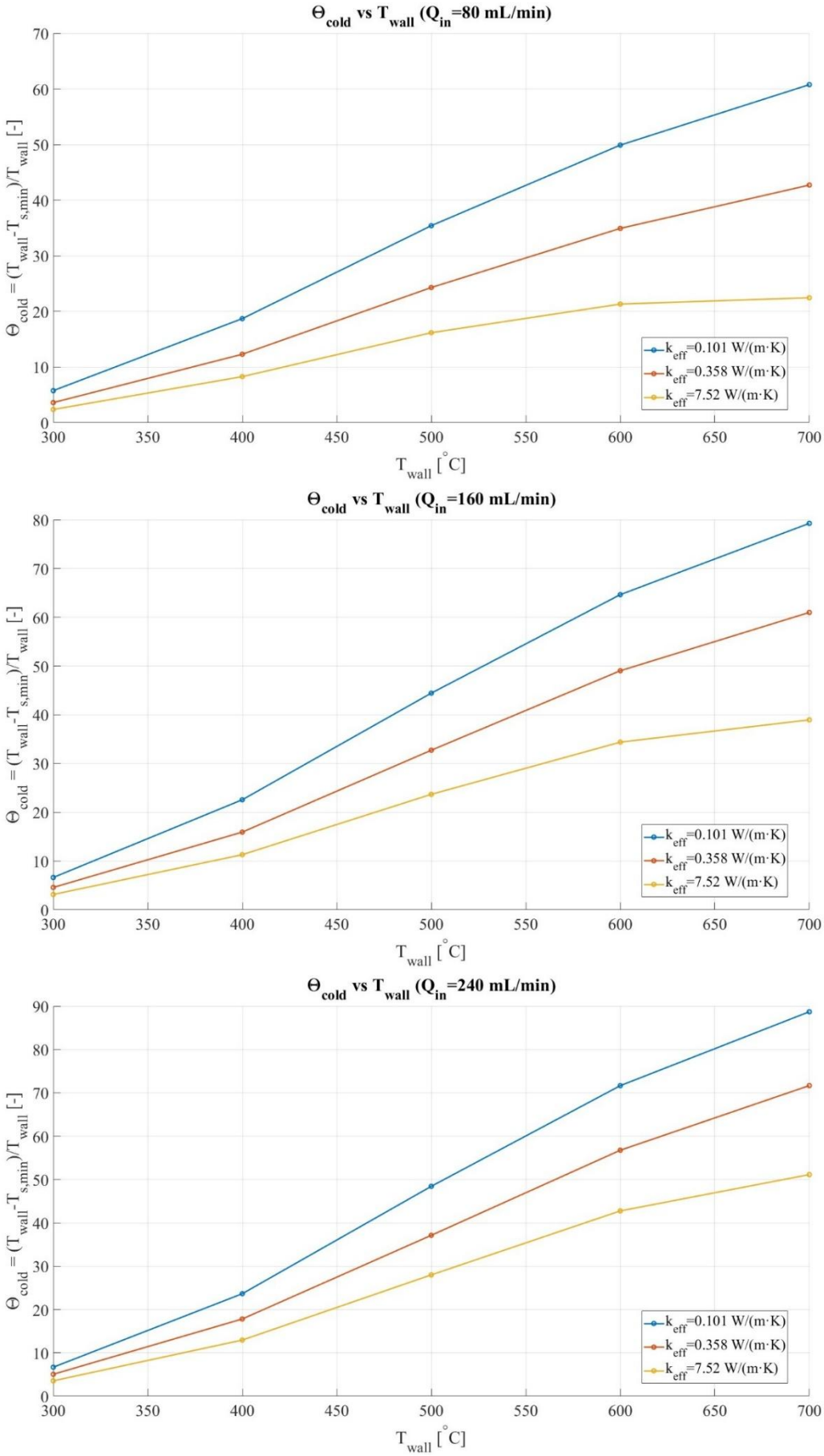

Figure 27, Theta vs Twall

For all conductivity values, the normalized temperature depression increases with wall temperature, indicating a progressive amplification of reaction-induced thermal gradients as the operating temperature rises. This amplification is substantially more pronounced under low-conductivity conditions, where limited intrabed heat redistribution allows local temperature deficits to intensify. In contrast, higher effective conductivity dampens the temperature sensitivity of the cold spot, moderating its growth as thermal demand increases.

LTNE Temperature Mismatch

To assess the thermal coupling between solid and fluid phases, the maximum local temperature difference between the two phases was evaluated as

$$\Delta T_{\mathrm{LTNE,max}} = \max \mid T_s - T_f \mid.$$

This indicator quantifies the intensity of local thermal non-equilibrium within the catalytic bed. Figure 28 shows the dependence of $\Delta T_{\mathrm{LTNE,max}}$ on effective thermal conductivity for representative wall temperatures.

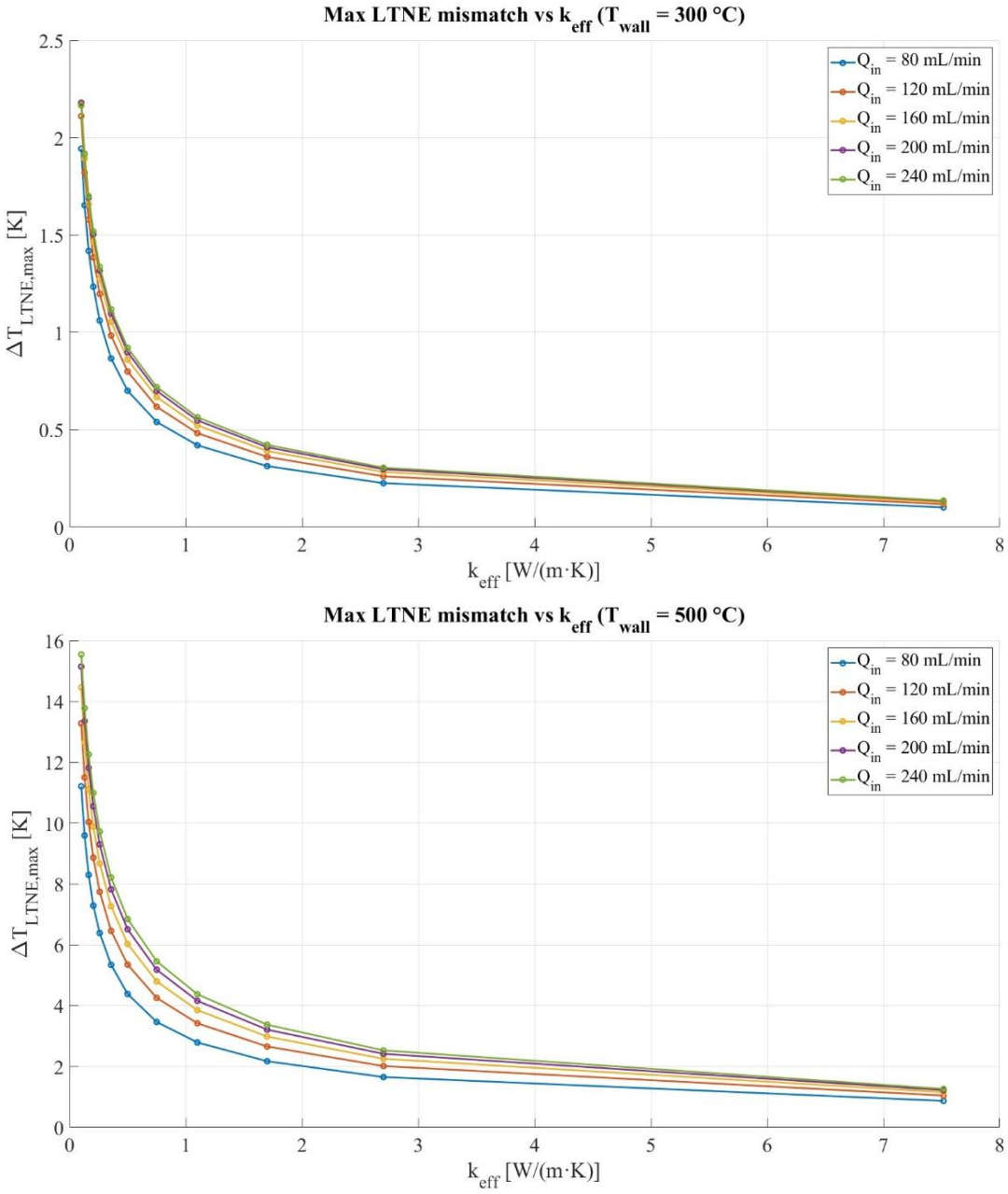

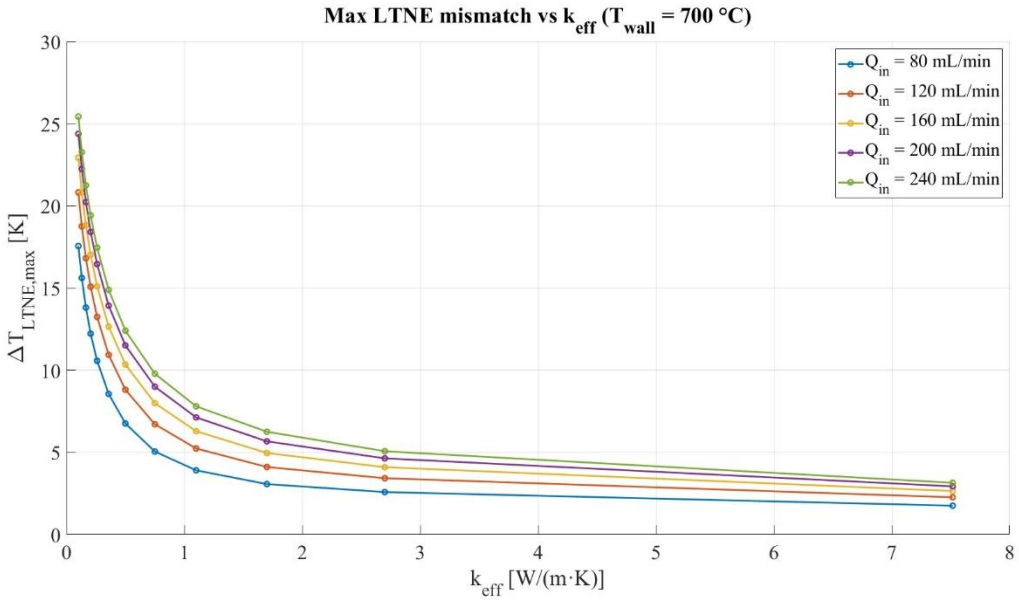

Figure 28, Max Temperature mismatch at fixed wall temperature

In all cases, increasing k_{eff} reduces the temperature mismatch by improving heat redistribution within the solid matrix and strengthening thermal coupling between phases. Nevertheless, a finite solid–fluid temperature difference persists even at high conductivity, indicating that conductive smoothing alone cannot fully suppress local non-equilibrium effects.

The magnitude of $\Delta T_{LTNE,\max}$ increases markedly with wall temperature. At low temperature, the solid–fluid temperature difference remains limited to a few kelvin, whereas at the highest investigated temperature it reaches several tens of kelvin. This behavior reflects the increasing thermal demand of the endothermic reaction, which amplifies local heat exchange between phases and intensifies thermal non-equilibrium.

A moderate dependence on inlet flow rate is also observed, with higher flow rates producing slightly larger temperature differences due to increased local heat consumption. Overall, the results indicate that solid–fluid thermal non-equilibrium remains significant under high-temperature operating conditions and is only partially mitigated by increased effective conductivity.

As effective conductivity increases, the magnitude of the solid–fluid temperature mismatch progressively decreases, eventually reaching only a few kelvin at the highest conductivity values. Under these conditions, local thermal non-equilibrium has a limited impact on global reactor performance. This provides a rationale for the widespread adoption of local thermal equilibrium (LTE) models in packed-bed reactor simulations. In many practical applications, effective bed conductivity is estimated using upper-bound formulations, such as the parallel model

$$k_{\text{eff}} = \theta_s k_s + (1 - \theta_s) k_f,$$

which yields relatively high conductivity values and therefore predicts small interphase temperature differences. When combined with the modest sensitivity of conversion to local temperature mismatch observed in the present study, simplified LTE formulations often provide sufficiently accurate predictions of overall reactor performance.

Nevertheless, the present results show that appreciable solid–fluid temperature differences can still arise under high-temperature and high-throughput conditions when realistic conductivity values are considered. The LTNE framework, therefore, remains necessary to accurately capture local thermal behavior and cold-spot formation, even when its influence on global conversion is limited.

The results show that effective bed conductivity primarily acts as a thermal smoothing parameter. Increasing conductivity mitigates cold-spot formation and reduces solid–fluid thermal mismatch, although its impact on overall conversion remains moderate within the investigated operating range.

3.2.2 Effect of Catalytic Bed Length

The influence of catalytic bed length on ammonia decomposition performance was investigated by varying the height of the porous bed (H_{bed}) between 5 and 20 mm.

Increasing bed length is expected to enhance conversion by increasing residence time and the amount of active catalyst. However, the conversion gain associated with additional catalyst volume is not necessarily proportional to bed length. As the reaction proceeds along the reactor axis, the incremental conversion achieved in the downstream region may decrease, leading to diminishing returns when extending the catalytic bed.

Outlet ammonia conversion ($X_{NH3,out}$) was used as a global performance metric. In addition, a characteristic length H_{95} was introduced to quantify the axial extent of the reactive region. This length corresponds to the bed height required to reach 95% of the outlet conversion under each operating condition.

From this quantity, the unused bed fraction was defined as

$$f_{unused} = 1 - \frac{H_{95}}{H_{bed}},$$

representing the fraction of catalyst volume providing only marginal additional conversion.

Conversion Behavior and Catalyst Utilization

For every temperature, increasing the inlet flow rate decreases $X_{NH_3,out}$ at a given H_{bed}, as shown in Fig. 29. This is consistent with reduced residence time.

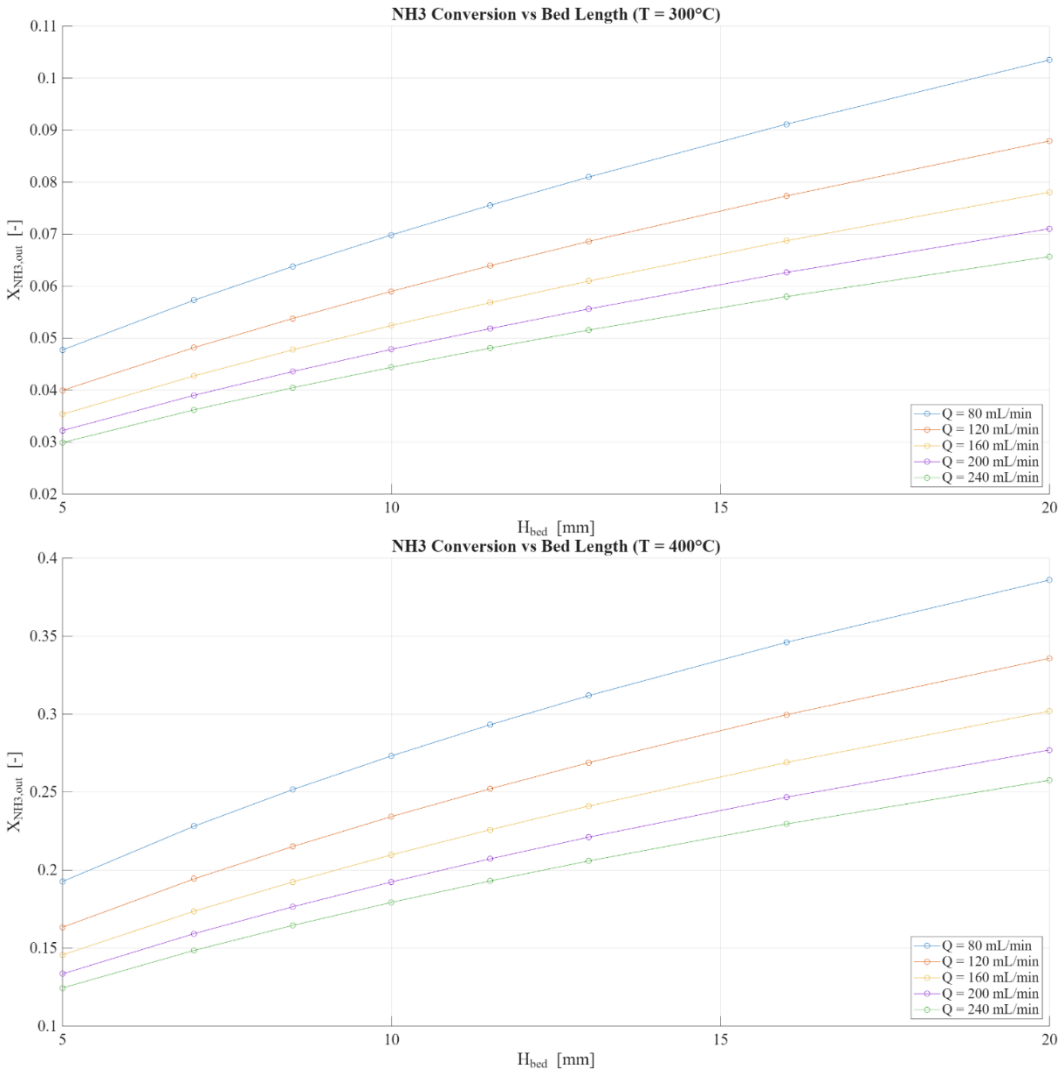

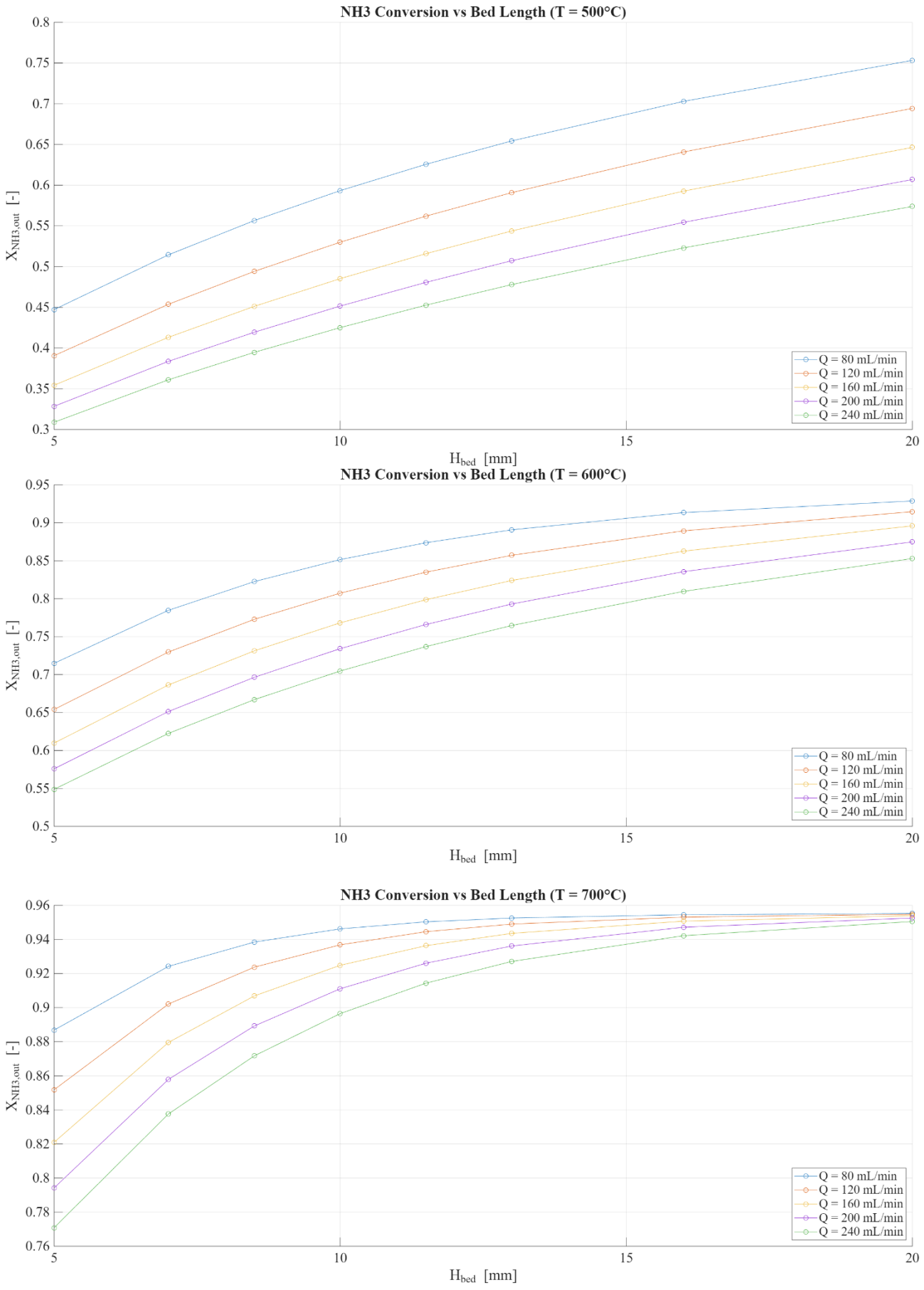

Figure 29, $X_{NH3,out}$ vs H_{bed} at different temperatures

At low and intermediate temperatures (300–500 °C), outlet conversion increases nearly linearly with bed length. This behavior indicates a residence-time-controlled regime, in which extending the catalytic bed directly increases reactant–catalyst contact time and results in proportional conversion gains. No saturation is observed within the investigated range, confirming that the catalyst volume remains effectively utilized and that the reactor does not approach a conversion limit under these conditions.

At higher temperatures (600–700 °C), the same monotonic dependence on bed length is preserved, but the incremental gain associated with additional bed height progressively decreases. At 600 °C the curves remain broadly linear, although a slight reduction in slope is visible at larger bed lengths. At 700 °C this effect becomes more evident: conversion rises rapidly at short bed lengths and then approaches a plateau, with only marginal improvements obtained beyond approximately 15–20 mm. In this regime, the higher intrinsic reaction rate allows high conversion to be achieved within shorter residence times, so that further increases in bed length produce diminishing returns in terms of outlet conversion.

Additional insight into the spatial distribution of the reaction can be obtained from the catalyst utilization analysis. Figure 30 presents the unused bed fraction as a function of bed length for the investigated operating conditions.

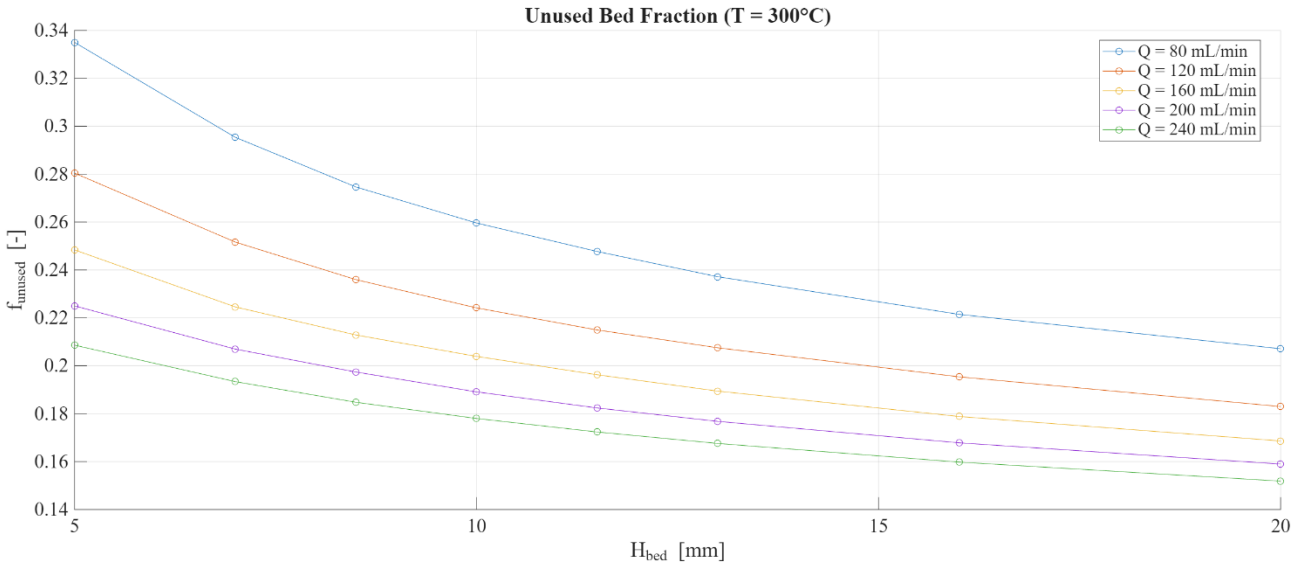

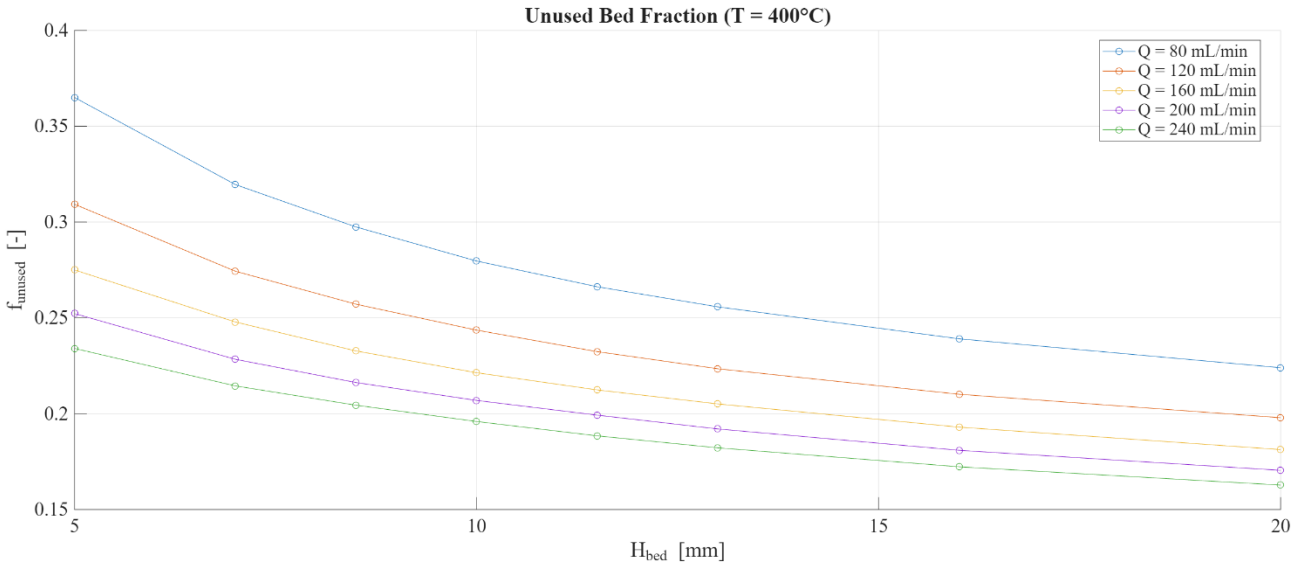

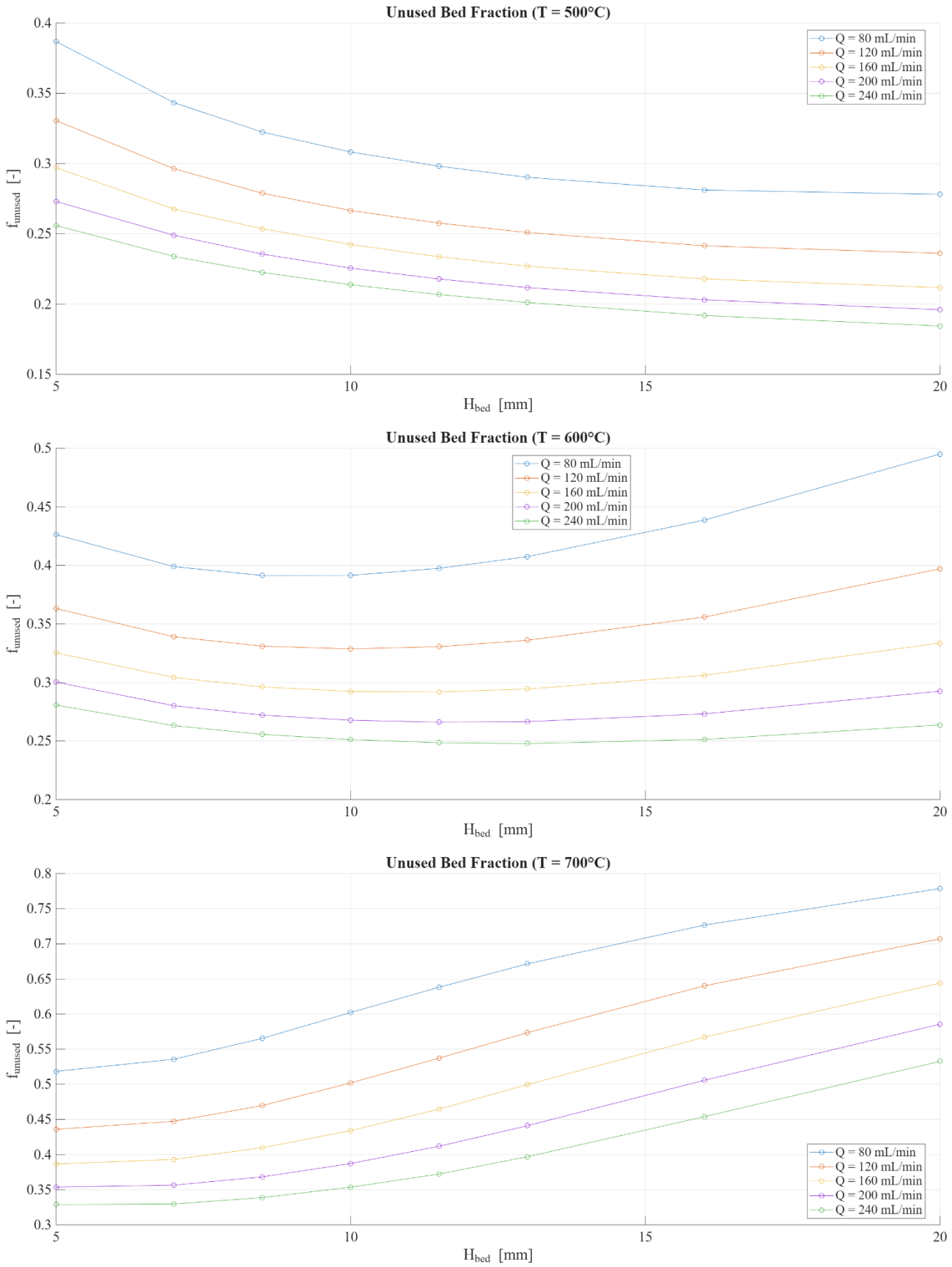

Figure 30, f_{unused} vs H_{bed} at different temperatures

At low and intermediate temperatures (300–500 °C), the unused bed fraction decreases monotonically with increasing bed length for all investigated flow rates. This indicates that, within the explored length range, the entire

catalytic volume contributes significantly to conversion and that extending the bed leads to progressively more complete catalyst utilization.

At 600 °C, a different behavior emerges. The unused bed fraction exhibits a minimum at an intermediate bed length and then increases again for longer beds. This trend is observed at all investigated flow rates and indicates that beyond a certain length the additional catalyst volume provides progressively smaller conversion gains. As the inlet flow rate increases, the minimum of the unused fraction shifts toward larger bed lengths. This is consistent with the reduction in residence time: at higher flow rates, a longer bed is required to utilize the available catalytic volume effectively .

At 700 °C, the unused bed fraction increases monotonically with bed length for all flow rates instead. This indicates that most of the conversion occurs within the upstream portion of the reactor and that further bed extension mainly adds catalytic volume that contributes only marginally to the overall conversion. Increasing the inlet flow rate reduces the unused fraction, but the increasing trend with bed length remains evident under all investigated conditions.

3.2.3 Effect of Kinetic Parameters

The sensitivity of the reactor model to the kinetic parameters appearing in the Temkin–Pyzhev rate expression was assessed by independently varying the pre-exponential factor K_0, the activation energy E_a, and the Temkin parameter α, while monitoring the outlet ammonia conversion $X_{NH_3,out}$. The results are reported in Figures 31–33 for three representative wall temperatures and three inlet flow rates.

The results highlight a clear difference in the influence of the kinetic parameters. The Temkin parameter α has a relatively limited impact on the outlet conversion, although it modifies the trend with temperature. At 300 °C, increasing α slightly increases the predicted conversion, whereas at 500–700 °C the trend reverses and higher α values lead to lower conversion.

This behavior reflects the role of α in the Temkin–Pyzhev rate expression, where the parameter modifies the relative dependence of the reaction rate on reactant and product partial pressures rather than directly scaling the overall rate constant. At low temperature, the reactor operates in a strongly reaction-limited regime, and the hydrogen concentration within the bed remains relatively low. Under these conditions, the forward decomposition term dominates and increasing α slightly enhances the effective reaction rate, resulting in higher conversion.

At higher temperatures, the overall conversion becomes much larger, and hydrogen accumulates along the reactor. The kinetic expression, therefore, becomes more sensitive to product inhibition and to the contribution of the reverse reaction. In this regime, increasing α shifts the balance of the rate expression in a way that slightly penalizes the net decomposition rate, leading to the decrease in predicted conversion observed in the simulations.

In contrast, the Arrhenius parameters E_a and K_0 strongly affect the predicted reactor performance. Variations of either parameter produce large changes in the outlet conversion across the investigated operating window. The sensitivity is particularly pronounced at the intermediate temperature of 500 °C, where the conversion spans a wide range depending on the kinetic parameters. At lower temperature the reactor remains strongly reaction-limited, whereas at the highest temperature, part of the parameter space already approaches high-conversion conditions.

Overall, the results indicate that the reactor performance is primarily controlled by the Arrhenius term of the kinetic expression, while the Temkin parameter mainly affects the detailed dependence of the reaction rate on gas composition. Overall, the results suggest a practical hierarchy of influence on the predicted conversion, with E_a and K_0 acting as the two dominant parameters and α playing a secondary role:

$$E_a \approx K_0 \gg \alpha$$

Within the investigated operating window, the largest discrimination among kinetic parameter sets is obtained at intermediate temperature, whereas low temperature emphasizes strongly nonlinear Arrhenius effects and high temperature progressively approaches conversion saturation.

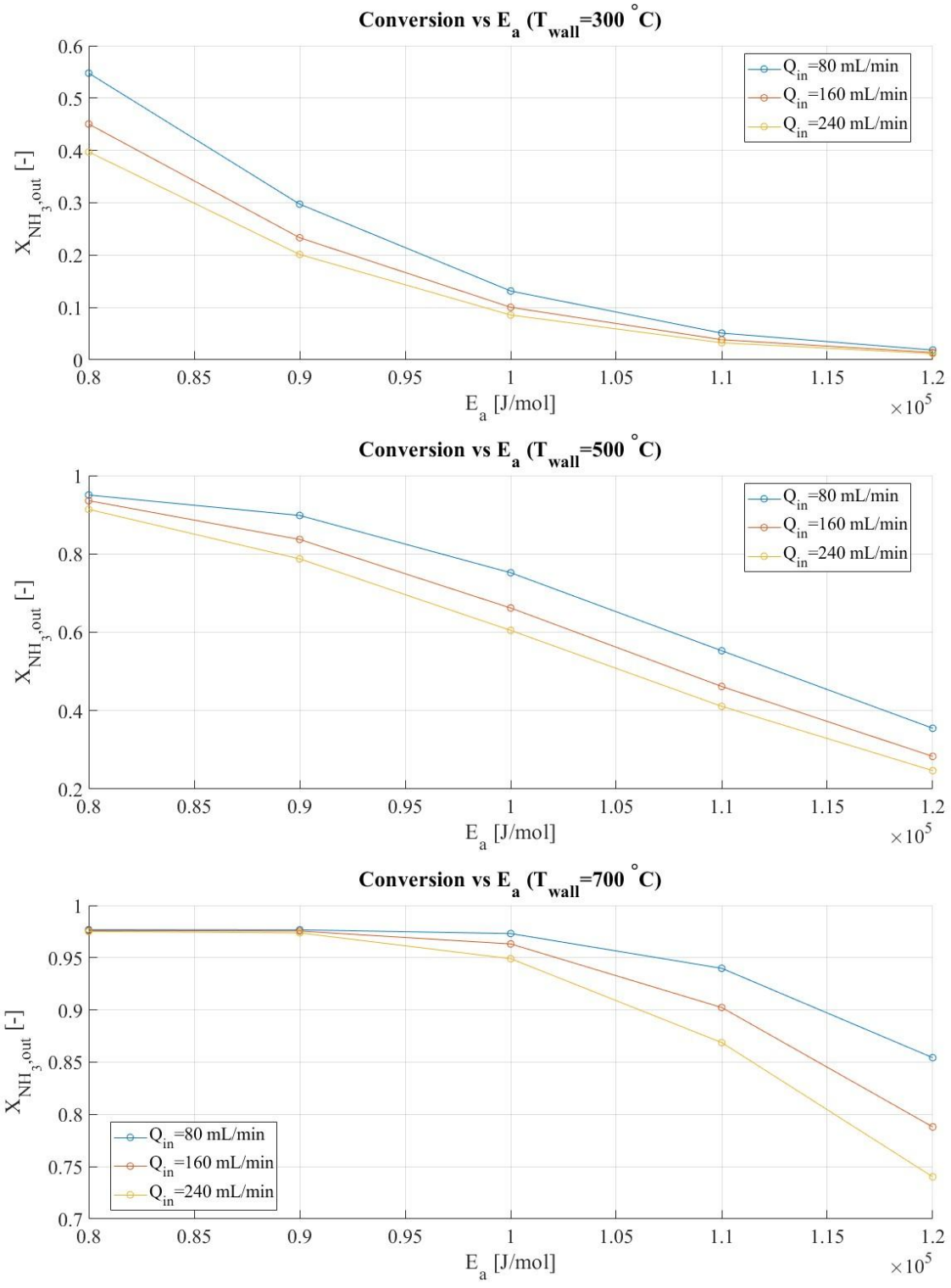

Figure 31, Conversion vs Ea at different temperatures

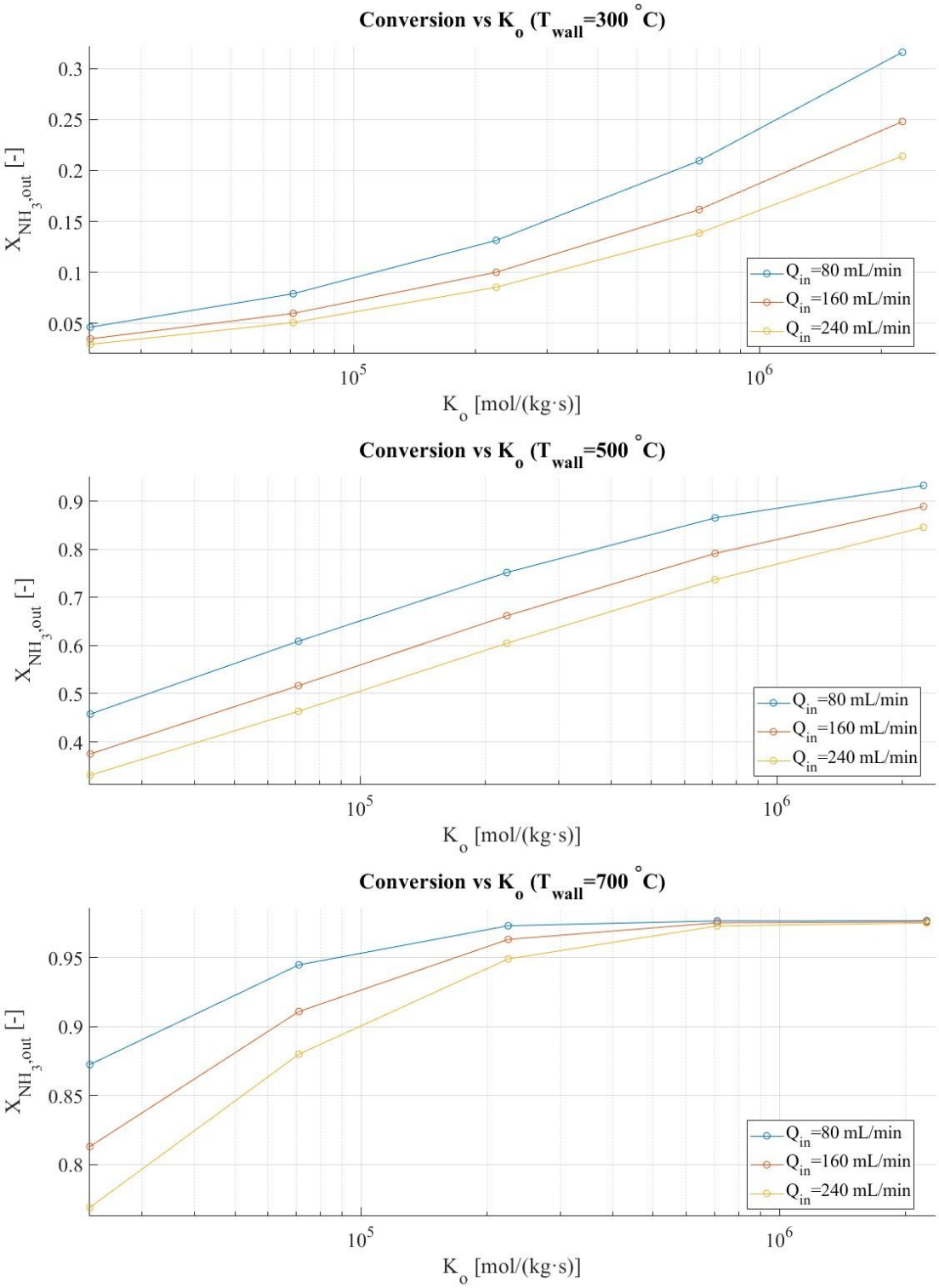

Figure 32, Conversion vs K_0 at different temperatures

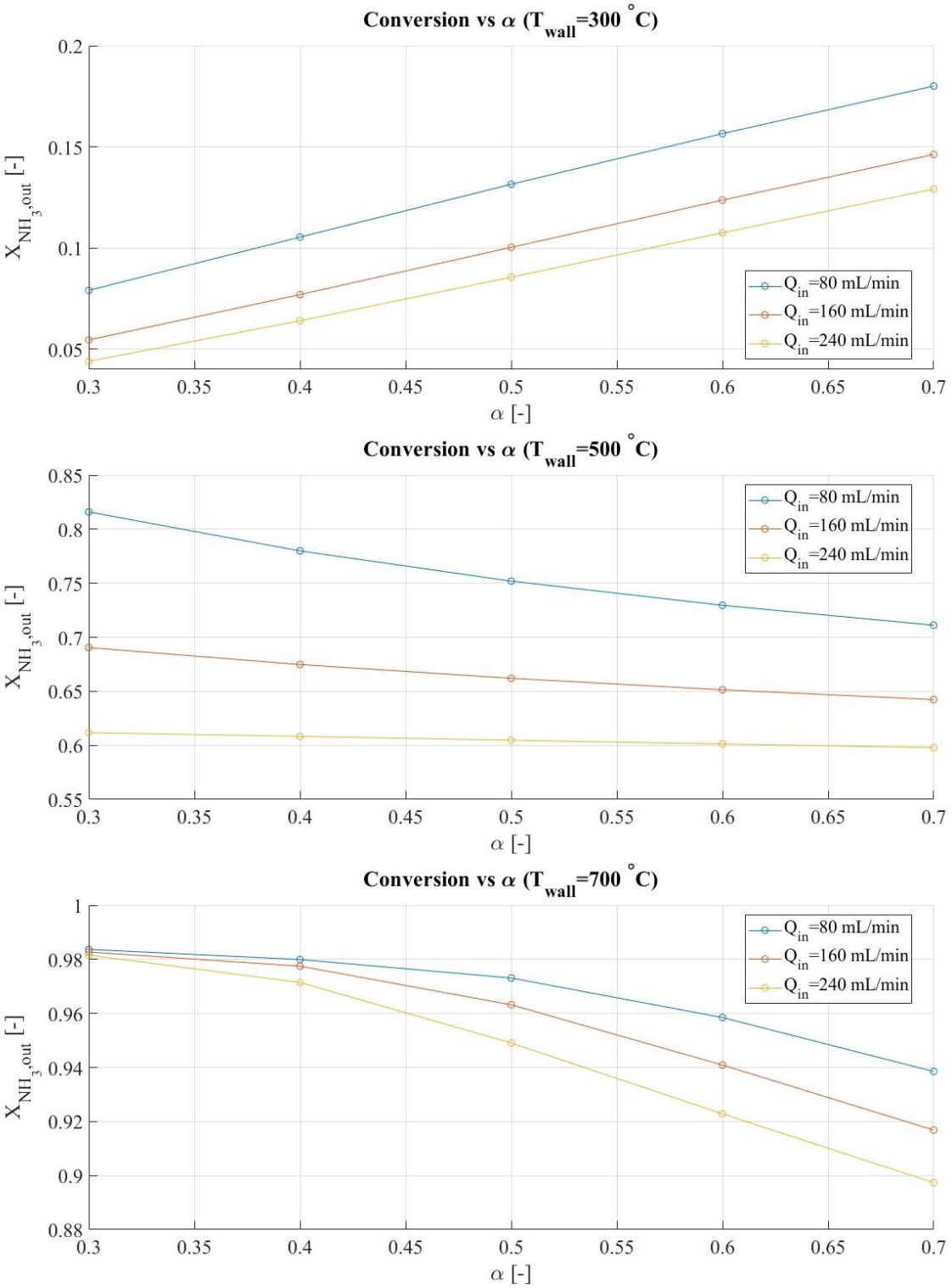

Figure 33, Conversion vs α at different temperatures

3.3 Performance Comparison of 3D-printed Monolithic Catalysts

The monolithic catalyst configurations described in Section 2.6 were analyzed using the validated CFD framework developed for the packed-bed reactor. Since the governing equations, transport models, and kinetic formulation remain unchanged, the numerical verification and consistency checks discussed in Section 3.1 apply to the monolithic simulations. The simulations were performed under the following operating conditions: the inlet temperature and the wall temperature were both set to 600°C, while the inlet pressure was set to 1 atm, and the inlet volumetric flow rate was set to 100 mL/min.

Prior to a comparison of the various monolithic geometries, it is instructive to highlight the fundamental differences between the packed-bed and monolithic configurations with respect to heat transport. To this end, an additional simulation of the porous catalytic bed was performed under the reported operating conditions, selecting the kinetic parameters such that a comparable overall conversion was obtained. In the porous bed, a pronounced temperature depression has been observed to develop within the catalytic region, with drops reaching almost 40 kelvin. This behavior represents a significant limitation for reactor operation, since the rate of ammonia decomposition is strongly dependent on the local temperature.

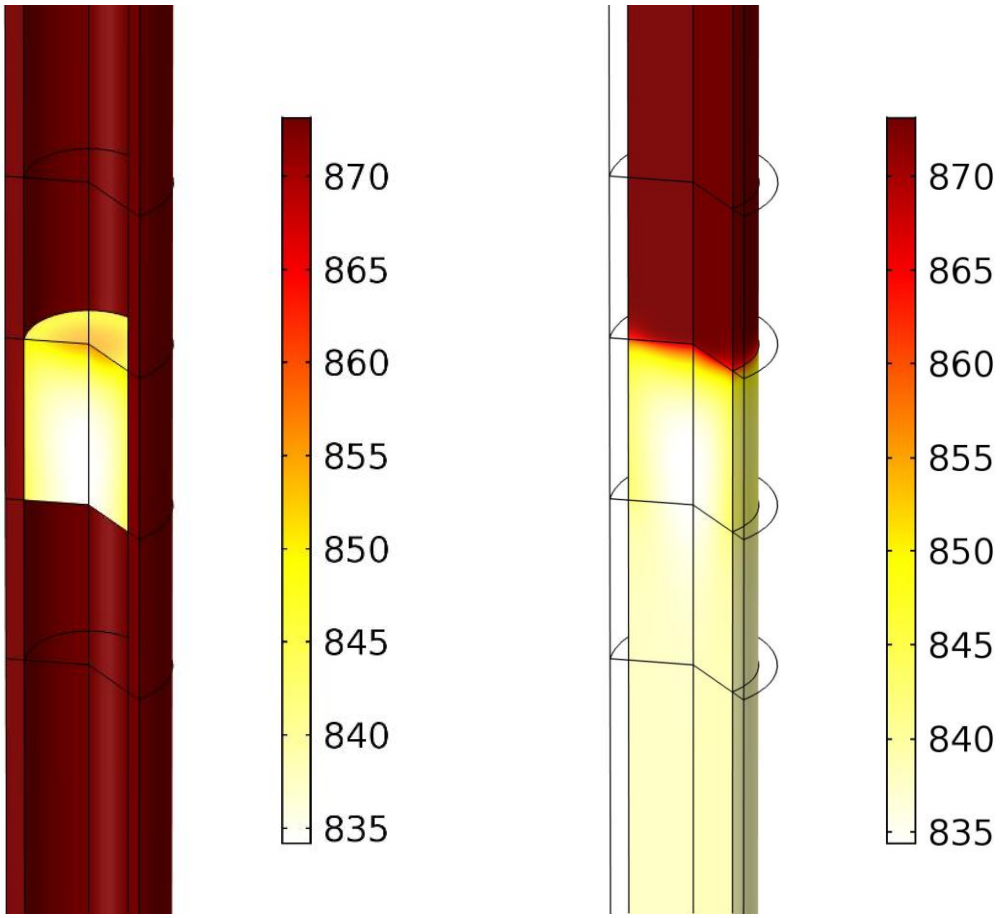

Figure 34, Temperature profiles of the solid phase (left) and the fluid phase (right) in the porous bed [K]

In contrast, monolithic metal structures demonstrate significantly more uniform temperature fields. The high thermal conductivity of nickel results in an efficient redistribution of heat throughout the solid phase, thereby mitigating the local cooling induced by the endothermic reaction. In fact, the temperature variations within the monolith are in the order of a few kelvins. The temperature distributions obtained for the four monolithic geometries are reported in Figure 35a-d.

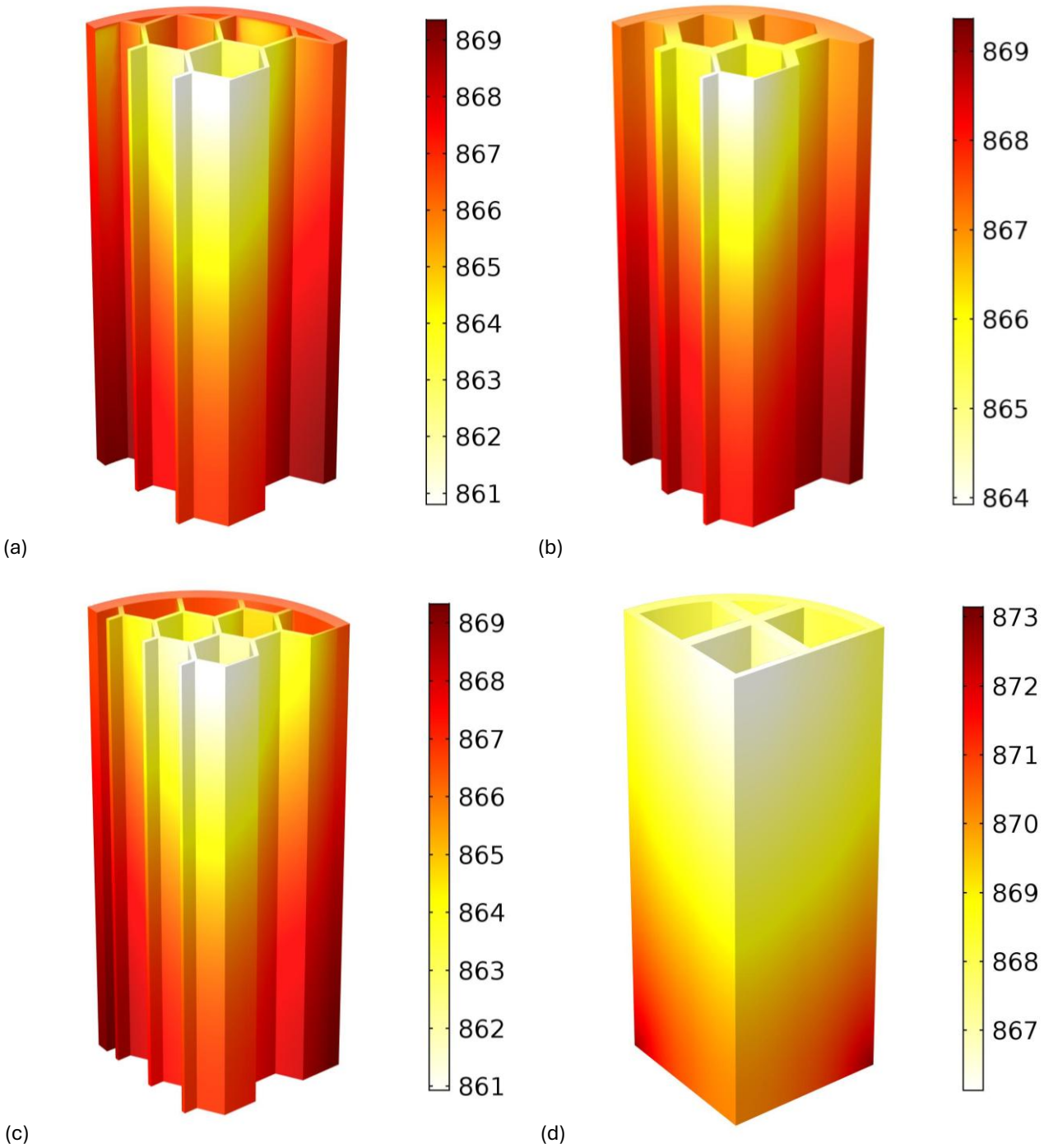

Figure 35, Monolith Temperature Field [K] of (a) Hexagon_CPSI400, (b) Hexagon_CPSI400_Massiv, (c) Hexagon_CPSI600, and (d) Agueniou

The geometries characterized by thicker walls, such as Square_CPSI400 and Hexagon_CPSI400, exhibit particularly smooth temperature profiles due to the larger conductive cross-section. On the other hand, geometries with finer channels can still provide favorable thermal conditions for the reacting gas. The smaller channel dimensions reduce the characteristic distance between the gas phase and the heated solid walls, which improves heat transfer to the fluid and limits the local temperature depression inside the channels. This effect can be observed in Figure 36, where the minimum gas temperatures remain relatively high despite the thinner walls of these structures.

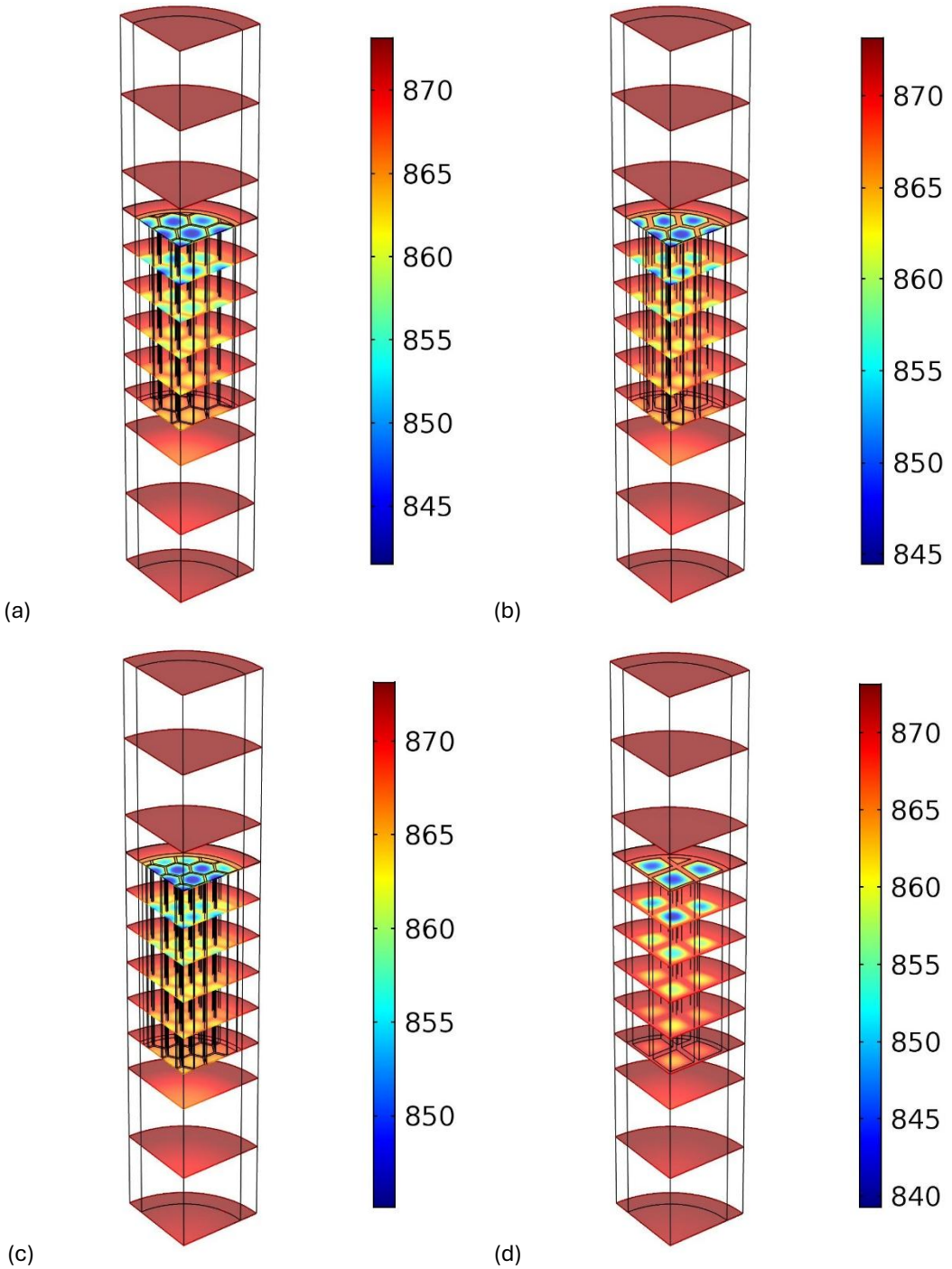

Figure 36, Temperature slices within the reactor [K] of (a) Hexagon_CPSI400, (b) Hexagon_CPSI400_Massiv, (c) Hexagon_CPSI600, and (d) Agueniou

Since the ammonia decomposition kinetics are strongly temperature dependent, the observed differences in the gas-phase temperature field are expected to influence the overall reactor performance. The resulting ammonia conversions obtained for the four monolithic geometries are summarized in Table 3.

Geometry	NH_3 conversion (%)
Hexagon_CPSI600	41.90
Hexagon_CPSI400	41.27
Hexagon_CPSI400_Massiv	39.41
Agueniou	38.28

Table 3, Overall Conversion in the different geometries

The calculated conversions indicate that, under the investigated operating conditions, the channel architecture moderately affects the overall reactor performance. Among the analyzed designs, Hexagon_CPSI600 provides the highest conversion, followed by Hexagon_CPSI400, and Hexagon_CPSI400_Massiv, while Agueniou geometry exhibits the lowest performance.

Although the minimum gas temperature provides a useful indication of the local cooling within the channels, it does not uniquely determine the overall reactor conversion. The reactor performance depends on the integrated reaction rate over the entire catalyst region, which is controlled by both the temperature field and the residence time of the reacting mixture. In this respect, the Hexagon_CPSI400_Massiv configuration exhibits a slightly higher minimum gas temperature than Hexagon_CPSI400, yet results in a lower overall conversion. This suggests that the beneficial thermal effect is partially offset by hydrodynamic factors, such as higher local velocities associated with the reduced open cross-sectional area created by the thicker struts, which may reduce the effective residence time of the reacting mixture inside the catalyst channels.

The pressure drop across the monolithic structures was found to be negligible (below 1 Pa) under the investigated operating conditions. The spatial distributions of NH_3, H_2, and N_2 within the monolithic reactor are shown in Figures 37-40.

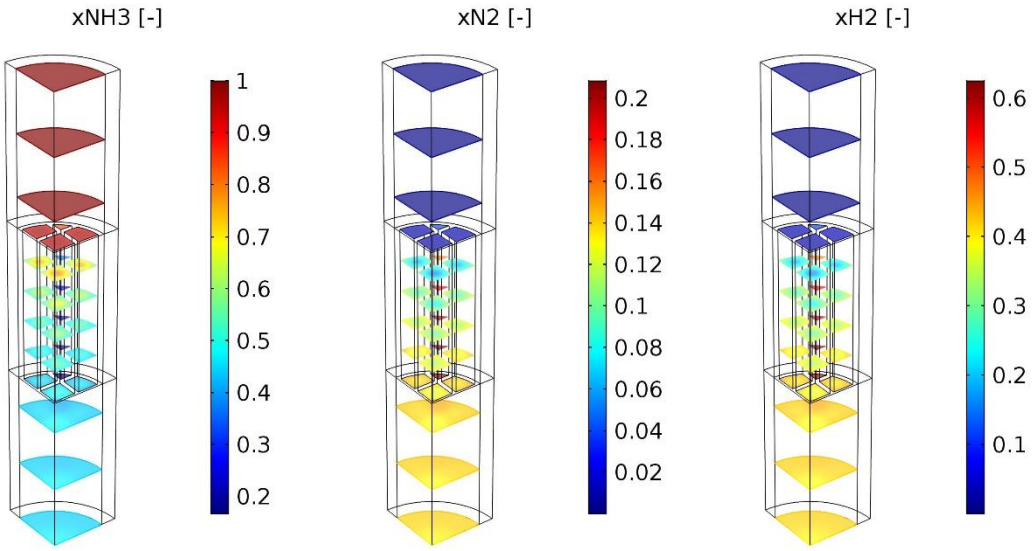

Figure 37, Agueniou Concentration Profiles

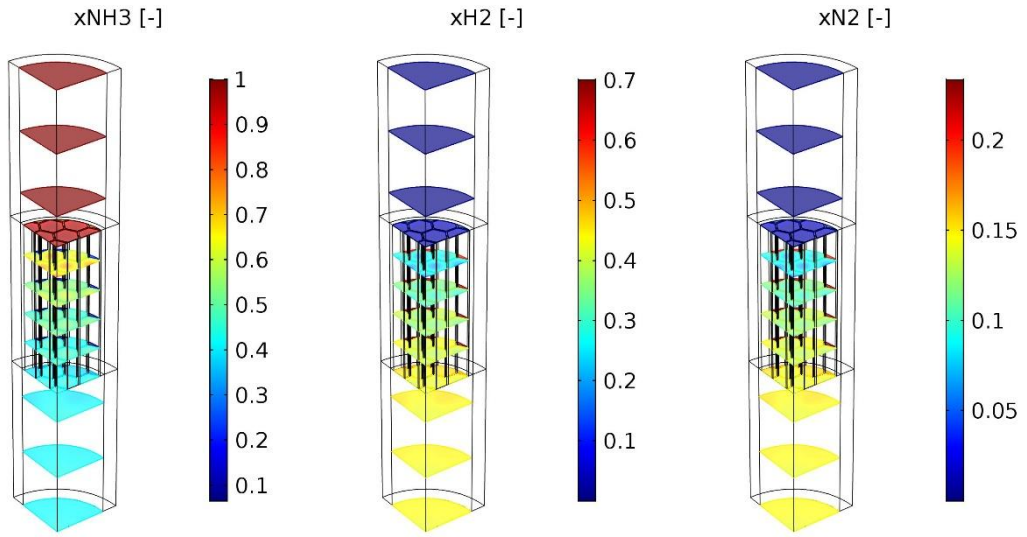

Figure 38, Hexagon_CPSI400 Concentration Profiles

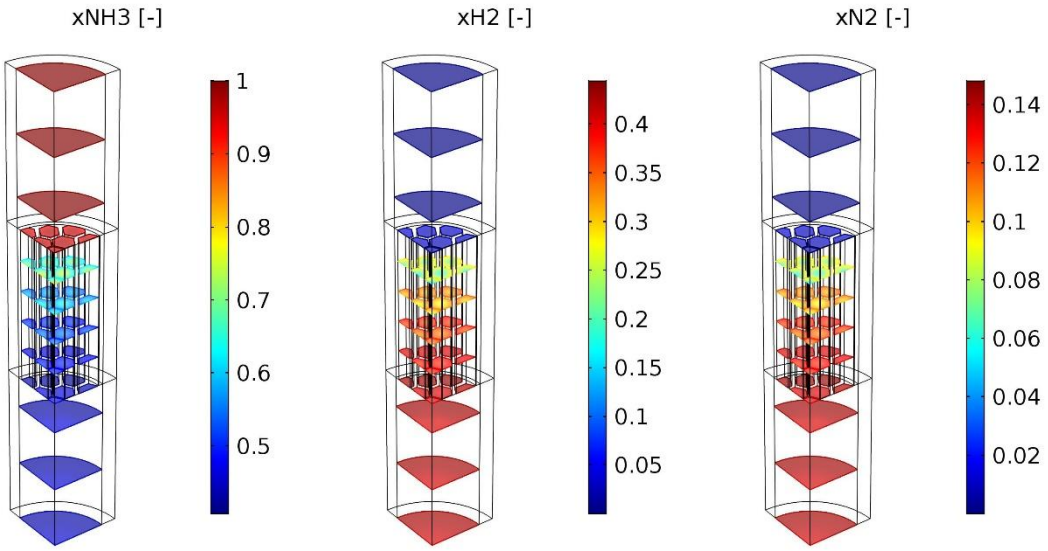

Figure 39, Hexagon_CPSI400_Massiv Concentration Profiles

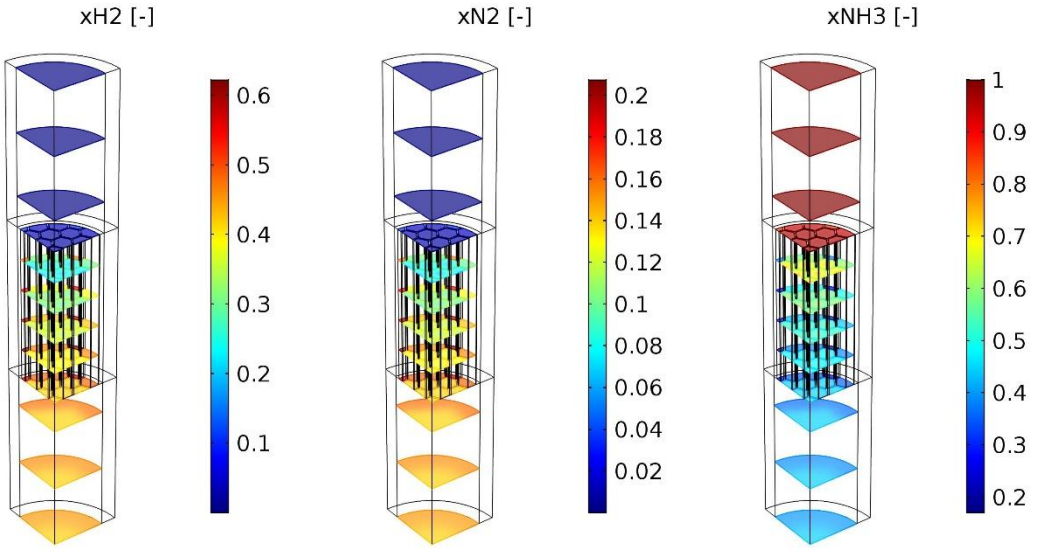

Figure 40, Hexagon_CPSI600 Concentration Profiles

Overall, the investigated monolithic catalyst geometries yield similar global conversions under the examined operating conditions, ranging from approximately 38% to 42%. The differences among the configurations can be associated with variations in channel size, wall thickness, and the resulting flow distribution within the catalyst structure. Higher channel density geometries have been observed to provide slightly higher conversions due to improved heat transfer between the heated solid walls and the reacting gas. The monolith exhibits significantly more uniformity than the packed-bed configuration, showcasing the advantage of the high thermal conductivity inherent in the metallic structure. Monolithic nickel catalysts effectively mitigate the substantial temperature depressions characteristic of packed-bed ammonia decomposition reactors, while preserving advantageous hydrodynamic characteristics and negligible pressure losses.

4. Conclusions

This thesis investigated the numerical modeling of ammonia decomposition in catalytic reactors through a CFD framework implemented in COMSOL Multiphysics. The developed model couples reacting flow in porous media with a local thermal non-equilibrium (LTNE) heat transfer formulation in order to capture the strong thermal effects associated with the highly endothermic nature of the reaction.

A systematic verification of the numerical framework was first carried out to assess the internal consistency of the coupled transport formulation. The model reproduces the expected qualitative behavior of ammonia decomposition reactors, including species evolution along the catalytic bed, molar expansion effects due to the reaction stoichiometry, and the strong temperature depression induced by the endothermic reaction. The analysis also identified the applicability limits of the numerical model, showing that physically consistent solutions are obtained only above a minimum inlet flow rate of approximately 80 mL/min under the most diffusion-favorable thermal conditions.

The parametric study highlighted the dominant role of heat transport in determining reactor performance. In particular, the effective thermal conductivity of the catalytic bed strongly affects the temperature distribution within the reactor, which in turn controls the local reaction rates. The analysis of the catalytic bed length showed that increasing the bed size enhances ammonia conversion, although diminishing returns are observed at high temperatures where the reaction approaches thermodynamic equilibrium. A sensitivity analysis of the kinetic parameters was also performed to evaluate the influence of uncertainties in the Temkin–Pyzhev rate expression. The results indicate that reactor performance is mainly controlled by the Arrhenius parameters (activation energy and pre-exponential factor), which strongly affect the predicted conversion, while the Temkin parameter primarily modifies the dependence of the rate on gas composition and has a comparatively smaller impact on the overall reactor behavior.

The modeling framework was then extended to analyze alternative catalyst configurations based on additively manufactured monolithic nickel structures. Compared with conventional packed beds, the metallic monolithic structures exhibit significantly more uniform temperature fields as a consequence of their high thermal conductivity. While the porous bed can experience temperature depressions of several tens of kelvin due to the strongly endothermic nature of ammonia decomposition, the monolithic configurations maintain much smaller temperature gradients, resulting in more favorable thermal conditions for the reaction.

The comparison among the different monolithic geometries indicates that variations in channel density and wall thickness only produce moderate differences in reactor performance, with predicted ammonia conversions ranging between approximately 38% and 42% under the investigated operating conditions. Overall, the results indicate that metallic monolithic catalysts constitute a promising alternative to conventional packed beds for ammonia decomposition reactors, primarily due to their improved thermal management and negligible pressure drop.

Despite these promising results, the present work includes several modeling simplifications. In particular, ammonia decomposition was implemented as a volumetric reaction term, and the kinetic parameters were taken from literature correlations without experimental validation for the considered geometries. Future work should therefore focus on the implementation of surface-based reaction models for monolithic catalysts, as well as on experimental validation of the proposed numerical framework.

Bibliography

A. Amiri, K. V. (1998). Transient analysis of incompressible flow through a packed bed. *International Journal of Heat and Mass Transfer, 41*, 3148-3168. doi:10.1016/S0017-9310(98)00120-3

Bockris, J. O. (2013). The hydrogen economy: Its history. *International Journal of Hydrogen Energy, 38*, 2579 - 2588.

Bruggeman, D. A. (1935). Berechnung verschiedener physikalischer Konstanten von heterogenen Substanzen. I. Dielektrizitätskonstanten und Leitfähigkeiten der Mischkörper aus isotropen Substanzen. *Annalen der Physik, 416*, 636-664.

Camel Makhloufi, N. K. (2021). Large-scale decomposition of green ammonia for pure hydrogen production. *International Journal of Hydrogen Energy, 46*, 34777-34787. doi:10.1016/j.ijhydene.2021.07.188

COMSOL AB. (2015). *COMSOL Heat Transfer Module User's Guide (Version 5.2)*.

COMSOL AB. (2015). *COMSOL Multiphysics Reference Manual (Version 5.2)*.

COMSOL AB. (2015). *The CFD Module User's Guide (Version 5.2)*.

COMSOL AB. (2015). *The Porous Media Flow Module User's Guide (Version 5.2)*.

Edward N. Fuller, P. D. (1966). A new method for prediction of binary gas-phase diffusion coefficients. *Industrial & Engineering Chemistry, 58*(5), 18–27.

El-Shafie, M. (2022). Hydrogen separation using palladium-based membranes: Assessment of H2 separation in a catalytic plasma membrane reactor. *International Journal of Energy Research, 46*, 3572-3587. doi:10.1002/er.7406

El-Shafie, M. (2023). A comprehensive assessment of ammonia synthesis reaction kinetics and rate equations. *International Journal of Hydrogen Energy, 48*, 35938-35952.

Elvira Spatolisano, L. A. (2023). Ammonia as a Carbon-Free Energy Carrier: NH3 Cracking to H2. *Industrial and Engineering Chemistry Research, 62*, 10813-10827. doi:10.1021/acs.iecr.3c01419

Enrique García-Bordejé, S. A. (2014). Toward Practical Application Of H2 Generation From Ammonia Decomposition Guided by Rational Catalyst Design. *Catalysis Reviews: Science and Engineering, 56*, 220–237.

Fazia Agueniou, H. V.-G.-I. (2022). Honeycomb monolithic design to enhance the performance of Ni-based catalysts for dry reforming of methane. *Catalysis Today, 383*, 226-235. Retrieved from https://doi.org/10.1016/j.cattod.2020.07.030

Haber, F., & Rossignol, R. L. (1913). Über die technische Darstellung von Ammoniak aus den Elementen. *Zeitschrift für Elektrochemie und Angewandte Physikalische Chemie, 19*, 53–72. doi:10.1002/bbpc.19130190201

Harriott, P. (1975). Thermal conductivity of catalyst pellets and other porous particles: Part I: Review of models and published results. *The Chemical Engineering Journal, 10*(1), 65-71. doi:10.1016/0300-9467(75)88018-X

Hossein Ali Yousefi Rizi, D. S. (2022). Green Hydrogen Production Technologies from Ammonia Cracking. *Energies, MDPI, 15*.

Hughes, M. S. (1979). The Thermal Conductivity of Porous Catalyst Pellets. *The Canadian Journal of Chemical Engineering, 57*, 24-28. doi:10.1002/cjce.5450570104

Hydrogen Council. (2017). Hydrogen scaling up - A sustainable pathway for the global energy transition.

Iain Staffell, D. S. (2019). The role of hydrogen and fuel cells in the global. *Energy and Environmental Science, Royal Society of Chemistry*. doi:10.1039/c8ee01157e

IEA. (2021). *Ammonia Technology Roadmap: Towards more sustainable nitrogen fertiliser production*. OECD Publishing, Paris.

IEA. (n.d.). The Future of Hydrogen, Seizing today's opportunities. *(Report prepared for the G20, Paris)*.

IRENA. ((Full report, 2019)). Global energy transformation: A roadmap to 2050 .

IRENA. (2019). Hydrogen: a renewable energy perspective.

Isao Nakamura, T. F. (2016). Role of metal oxide supports in NH3 decomposition over Ni catalysts. *Applied Catalysis A: General, 524*, 45-49.

Korawich Trangwachirachai, K. R. (2024). Recent progress on ammonia cracking technologies. In *Current Opinion in Green and Sustainable Chemistry* (Vol. 49). Elsevier B.V.

Kozeny, J. (1927). *Uber Kapillare Leitung der Wasser in Boden* (Vol. 136). Hölder-Pichler-Tempsky, A.-G.

L. Gavrilović, J. P. (2024). AMMONIA AS A HYDROGEN CARRIER – BENCHMARK CATALYSTS FOR AMMONIA CRACKING. *Institute for Energy Technology, 2007 Kjeller, Norway*.

Lucentini Ilaria, G. X. (2021). Review of the Decomposition of Ammonia to Generate Hydrogen. *Industrial and Engineering Chemistry Research*.

Mittasch, A., & Frankenburg, W. (1950). *Advances in Catalysis, Volume 2*. Academic Press.

N. Bartal, G. S. (2009). *Modeling of a Catalytic Packed Bed Reactor and Gas*. WORCESTER POLYTECHNIC INSTITUTE.

Nadia Mohd Adli, H. Z. (2018). Review - Ammonia Oxidation Electrocatalysis for Hydrogen Generation and Fuel Cells. *Journal of The Electrochemical Society, 165*, J3130-J3147. doi:10.1149/2.0191815jes

National Institute of Standards and Technology, Gaithersburg, MD, USA. (n.d.). *NIST Chemistry WebBook, NIST Standard Reference Database Number 69*. Retrieved November 2025, from https://webbook.nist.gov

O Colomés, I. R. (2023–2024). *Finite Elements in Civil Engineering and Geosciences. Delft University of Technology*. Retrieved 2025, from https://interactivetextbooks.citg.tudelft.nl/computational-modelling/introduction/discrete.html

R. G. Carbonell, S. W. (1984). Heat and Mass Transfer in Porous Media. In *Fundamentals of Transport Phenomena in Porous Media* (pp. 121–198). doi:10.1007/978-94-009-6175-3_3

(2024). *Ruthenium Market – Global Industry Analysis, Size, Share and Forecast*. 360 Research Reports. Retrieved 01 15, 2026, from https://www.360researchreports.com/market-reports/ruthenium-market-201250

S. Armenise, E. G.-B. (2013). A Langmuir-Hinshelwood approach to the kinetic modelling of catalytic ammonia decomposition in an integral reactor. *Physical Chemistry Chemical Physics, 15*, 12104-12117. doi:10.1039/c3cp50715g

Shreya Mukherjee, S. V. (2018). Low-Temperature Ammonia Decomposition Catalysts. *Applied Catalysis B: Environmental, 226*, 162-181. doi:10.1016/j.apcatb.2017.12.039

Speybroeck, V. V. (2024). Following the dynamics of industrial catalysts under operando conditions. *Proc. Natl. Acad. Sci. U.S.A. , Vol. 121*(2).

Stefan Peters, A. M.-M. (2023). Thermocatalytic Ammonia Decomposition – Status and Current Research Demands for a Carbon-Free Hydrogen Fuel Technology. *ChemCatChem, 15*. doi:10.1002/cctc.202201185

T. E. Bell, L. T.-M. (2016). H2 Production via Ammonia Decomposition Using Non-Noble Metal Catalysts: A Review. *Topics in Catalysis, 59*, 1438-1457. doi:10.1007/s11244-016-0653-4

TEMKIN, M. .. (1979). The Kinetics of Some Industrial Heterogeneous Catalytic Reactions, . In *ADVANCES IN CATALYSIS, Volume 28* (pp. 173-287).

Valentina Cechetto, L. D. (2021). H2 production via ammonia decomposition in a catalytic membrane reactor. *Fuel Processing Technology, 216*. doi:10.1016/j.fuproc.2021.106772

W Woodside, J. H. (1961). Thermal Conductivity of Porous Media. I. Unconsolidated Sands. *Journal of Applied Physics, 32*, 1688–1699.